EXCITING COHERENT PROCESSES IN CATHODOLUMINESCENCE

Ph.D. Thesis, University of Amsterdam, December 2025
Exciting coherent processes in cathodoluminescence
E. A. Akerboom

Cover: (back) Calculated convergent beam electron diffration pattern from graphene, with two people swing dancing in the background (made with AI), 'activating' the diffraction disk that they are standing on.
(front) Calculated interference pattern from cathodoluminescence emitted from the 'activated' diffraction spots (red circles) in the back.

ISBN 978-94-92323-87-3

The work described in this thesis was performed between October 2021 and December 2025 at NWO-institute AMOLF, Science Park 104, 1098 XG Amsterdam, The Netherlands.

This work is part of the research program of the Dutch Research Council (NWO).

A digital version of this thesis is available at https://ir.amolf.nl.

EXCITING COHERENT PROCESSES IN CATHODOLUMINESCENCE

ACADEMISCH PROEFSCHRIFT

ter verkrijging van de graad van doctor
aan de Universiteit van Amsterdam
op gezag van de Rector Magnificus
prof. dr. ir. P.P.C.C. Verbeek
ten overstaan van een door het College voor Promoties ingestelde commissie,
in het openbaar te verdedigen in de Agnietenkapel
op woensdag 11 maart 2026, te 10.00 uur

door Evelijn Anne Akerboom
geboren te Amsterdam

Promotiecommissie

Promotor:	prof. dr. A. Polman	Universiteit van Amsterdam
Copromotor:	prof. dr. F. J. García de Abajo	ICFO
Overige leden:	prof. dr. E. Alarcón Lladó	Universiteit van Amsterdam
	prof. dr. P. C. M. Planken	Universiteit van Amsterdam
	dr. J. van de Groep	Universiteit van Amsterdam
	dr. W. Albrecht	AMOLF
	prof. dr. C. Ropers	Max Planck Institute for Mathematics

Faculteit der Natuurwetenschappen, Wiskunde en Informatica

Contents

1

Introduction

The perception of our surroundings is governed by the interaction between light and matter. In the visible range of the electromagnetic spectrum, with wavelengths between approximately 380 nm and 750 nm, this interaction gives rise to the optical phenomena we observe in daily life, from the transparency of glass to the red line on a positive COVID test. To understand these phenomena, it is useful to distinguish three regimes of light–matter interaction. At the macroscopic scale, ray optics dominates, and light propagation can be described by Fermat's principle. At the opposite extreme lies the subwavelength regime, where objects are much smaller than the wavelength of light. In this limit, the optical response of a heterogeneous medium can often be captured by an effective refractive index, determined by the weighted contributions of its constituents.

Between these two extremes lies an intermediate, regime where the characteristic dimensions of the structures are comparable to the wavelength of light. Here, neither the ray picture nor the effective-medium approximations are applicable: light and matter interact in complex ways that sometimes give rise to resonant effects[1]. Optical fields can become strongly confined within or around nanoparticles leading to distinct resonant peaks in the scattering spectrum, which are highly sensitive to the particle's size, geometry, and refractive-index[2]. The ability to harness these resonant interactions has opened many technological opportunities. They are exploited to capture energy in photovoltaic devices[3–5], drive chemical reactions using plasmonic nanostructures [6–10], and are the basis of analog computations in the optical domain [11–13], to mention just a few examples. In all of these applications, precise control over light–matter interactions across length scales is essential.

1

1.1. Nanophotonics

To control of light at the nanoscale, with top-down (nanostructuring) and bottom-up (colloid synthesis of nanoparticles) approaches. Plasmonic nanoparticles have been extensively studied, as they support collective oscillations of free electrons, localized surface plasmon resonances (LSPRs), that concentrate electromagnetic energy into subwavelength volumes. In addition, plasmonic surfaces can sustain surface plasmon polaritons (SPPs), electromagnetic waves confined to the interface and capable of propagating over relatively long distances. Plasmonic structures have enabled light confinement in nanoscale geometries[14, 15], the realization of plasmonic nanolasers[16], and the development of plasmonic antennas that efficiently couple light to and from nanostructures[17, 18].

Additionally, dielectric nanostructures exhibit a strongly geometry- and size dependent optical response arising from the Mie resonances supported by the material. Compared to plasmonic systems, dielectric structures feature significantly reduced losses and can sustain both electric and magnetic resonances, enabling high field enhancement without substantial absorption. The interplay and spectral overlap of these modes can give rise to Fano resonances and pronounced directional scattering, phenomena that are exploited in applications such as anti-reflection coatings [19]. Moreover, advances in design and fabrication now allow dielectric metasurfaces to replicate the functionality of some bulk optical components [20].

1.2. Electron microscopy

The need to control light-matter interactions has also stimulated the development of instruments capable of probing the structure and optical properties with nanoscale precision. Among these, the electron microscope stands out as a powerful tool. From the first prototype that used 50 keV electrons to achieve a magnification of only 17.4× [21], to today's transmission electron microscope (TEM) capable of resolving individual atoms at 200 keV with sub-ångstrom resolution [22], the evolution of electron optics has continuously expanded the limits of what can be visualized. The small de Broglie wavelength of high-energy electrons (2.5 pm at 200 keV) enables spatial resolutions far beyond the optical diffraction limit, while their wave nature provides additional opportunities to probe matter at the atomic scale.

The first TEM was developed in 1931 by Rushka and Knoll[21, 23], with the goal of surpassing the spatial resolution limits of the optical microscope, a milestone achieved only one year after the initial proof of concept[24]. Following this, the development of electron microscopy progressed rapidly. Initially, electron microscopy was used in material science to investigate the atomic ordering and defects of thin metallic foils. Soon after, its use expanded to biological application, where it enables the visualization of viruses and bacteria[25, 26]. After five decades of technological developments, the accessible space-time resolution of TEM now spans the picometer (pm) spatial scale to the femtosecond (fs) temporal scale, using an ultrafast TEM [27]. This evolution of electron microscopy was rewarded with the Nobel

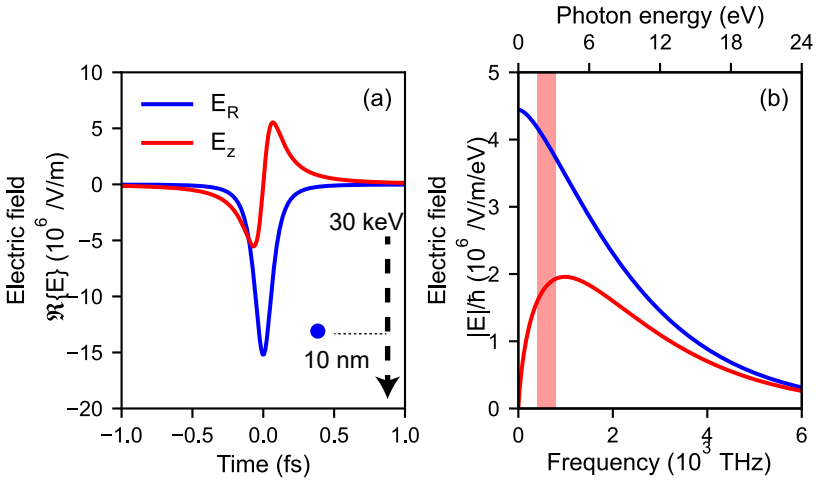

Figure 1.1: Real part of the radial (E_R) and axial (E_z) component of the electric field of a 30 keV electron at 10 nm distance from the e-beam trajectory (a) in time and (b) in frequency. The top axis in (b) shows the corresponding photon energy, with the red window indicating the visible energy range. Figure created on basis of Ref. [31].

prize in 2017[28] for the development of cryo-EM as a technique for high-resolution structural imaging of biological specimen[29].

In addition to their particle-like nature, electrons exhibit wave-like properties, which can be exploited to extract complementary structural information. In 1937, G. P. Thomson first observed electron diffraction from crystalline lattices[30], establishing the wave nature of electrons. This gave rise to the development of a range of diffraction-based techniques such as selected-area electron diffraction (SAED), electron backscatter diffraction (EBSD), and convergent-beam electron diffraction (CBED), each providing unique insights into the crystallographic structure of materials.

1.3. Electron spectroscopy techniques

Electron microscopy is an ideal tool for determining the structural properties of a specimen. However, secondary or transmitted electrons alone do not provide information on how the specimen interacts with light. To probe these interactions, the energy exchange between the electron and the material has to be measured and understood. Due to its electric charge, an electron carries an accompanying electric near field. Figure 1.1a illustrates the real part of the radial and axial components of this near field as a function of time, at a distance of 10 nm from the trajectory of a 30 keV electron. Due to the high velocity of the electron, the total duration of the electric-field pulse is only about a femtosecond. Taking the Fourier transform yields the corresponding frequency spectrum, shown in Figure 1.1b. The

broad spectrum, which extends from 0 to over 20 eV, reveals that a passing electron can act as a broadband source of optical excitation while simultaneously providing the nanoscale spatial resolution characteristic of electron microscopy. This dual capacity makes the electron beam (e-beam) a powerful tool to probe electric near fields at the nanoscale.

1.3.1. Electron energy-loss spectroscopy

Several techniques have been developed to exploit this property of the e-beam, one of which is electron energy loss spectroscopy (EELS). In this technique, typically performed in the TEM, the energy spectrum of the electron is measured after it passed through or near a thin specimen. The induced electric field in the specimen acts back on the electron, slowing it down. The resulting electron-energy loss provides a measure of the strength and spatial distribution of the electron-induced electric near fields at the nanoscale. EELS has been widely used to map plasmonic or dielectric resonances[32–36]. Furthermore, the development of momentum-resolved EELS has enabled the measurement of phonon dispersion[37, 38]. More recently, a combined energy loss and momentum transfer measurement technique has been demonstrated[39].

1.3.2. Cathodoluminescence

A complementary approach to probe light-matter interaction in the electron microscope is to measure light emitted due to electron excitation, termed cathodoluminescence (CL). CL can be categorized into incoherent and coherent CL. In incoherent CL, the electron excites bandgap transition or other excited states in a material, which then relax via spontaneous photon emission[40, 41]. Due to the statistical nature of the process in time, the emitted photons bear no temporal phase relation to the incidence of the electron. In coherent CL, however, the phase relation between the electron and the emitted photon is preserved. As the electron polarizes the material, it excites optical resonances in the specimen that can decay radiatively, emitting photons that carry phase information of the excitation. By analyzing the spectrum, angular distribution and polarization of the light, the underlying resonances can be identified. The coherent nature of this emission also enables interference effects when a single electron sequentially excites multiple scatterers, as demonstrated for example by the Smith-Purcell effect[42], which is the result of constructive interference of multiple excited scatterers, creating broadband light emission[43, 44].

1.3.3. Ultrafast electron microscopy

In recent years, electron microscopy has started to further explore the quantum nature of the interaction between electrons, matter, and light[45]. In free space, an electron cannot directly exchange energy with light due to momentum mismatch. However, in the vicinity of a nanostructure illuminated by an external light field, the induced optical near field carry a broad range of spatial frequencies that enable overcoming this mismatch. Using an external laser, it is possible to perform

photon-induced near-field electron microscopy (PINEM)[46], in which the electron loses or gains an integer multiples of the photon energy ($\hbar\omega$). This process enables manipulation of the energy spectrum of a single electron, providing a powerful means to shape the electron wave function in space and time[47–49]. This control over the electron wave function enables the generation of attosecond electron pulses[50, 51], spatial shaping of the electron wave packet[52], and acceleration of the electron[53, 54]. Such quantum-mechanical shaping of the electron may enable new forms of ultrafast spectroscopy, or even aberration correction in the electron optics of the electron microscope[55, 56].

These tailored electrons can be used to investigate nanophotonic structures at high temporal and spatial resolution. By varying the time delay between the electron and the laser field, Gaida *et al.* reconstructed the phase of optical electric near fields at the nanoscale[57]. Nabben *et al.* used an electron shaped into a train of ultrashort pulses to produce a movie of the electric near fields in time[58]. These developments open up a wide range of possibilities and has inspired numerous theoretical proposals exploring new regimes of electron-light-matter interactions[45, 59–61].

Coincidence techniques reveal additional information that is often lost in conventional CL or EELS measurements that integrate data from multiple excitations. Studies of coincidence between the primary electron and the generation of an X-ray[62] or a visible photon [63] has been explored. Such measurements provide effective background subtraction[64] and have been used to identify the nature of electron excitations[65], and to measure excited-state lifetimes[66].

Beyond the classical correlations, coincidence measurements also open the door towards studying entanglement between electrons and photons, as first proposed theoretically[67–70]. Electron-photon entanglement has recently been experimentally demonstrated by Henke *et al.*[71]. Bogdanov *et al.* achieved ghost imaging using electron-photon pairs[72]. Treating the electron as a quantum object thus paves the way for exploring the quantum properties of materials.

1.4. Scanning electron microscope

Most of the techniques discussed above are performed in a TEM operating at energies in the range 80-300 keV. This is primarily due to two factors. First, the more advanced electron optics, including aberration correction in the TEM, provides the best spatial resolution. Second, since most techniques rely on analyzing transmitted electrons, sufficiently high energies are required for the electrons to travel through the specimen. The highly advanced electromagnetic lenses in modern TEMs enable the formation of high-quality images, better energy resolution in EELS and higher angular resolution (on the order of μrad) in diffraction. However, TEMs also have significant limitations. The small size of the specimen chamber makes it technologically challenging to implement techniques that require additional optical components, as are needed for advanced CL spectroscopy. Furthermore, TEMs

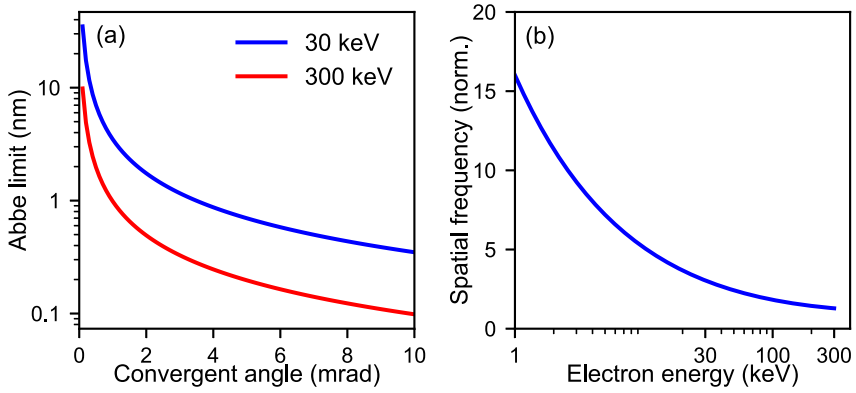

Figure 1.2: Characteristic of the electron microscope. (a) Abbe resolution limit as a function of semi-convergent angle for a 30 keV (blue), or 300 keV (red) electron. (b) Normalized spatial frequency ($q/k = c/v$) as function of electron energy.

are expensive, and their operation demands highly trained people and precise control of the environment.

In this respect, the scanning electron microscope (SEM) offers several advantages. The specimen chamber is more spacious, allowing for the integration of CL collection system[73], optical in-coupling systems, and larger custom sample holders. SEMs are also more affordable and easier to operate. Furthermore, as we will also show in this thesis for certain geometries, the electron-matter coupling strength is higher at lower energies. However, the SEM electron energies (1-30 keV) result in poorer spatial resolution. Figure 1.2a shows the diffraction-limited spatial resolution as a function of semi-convergence angle for 30 keV and 300 keV electrons showing the difference in resolution for typical TEM and SEM conditions. Nevertheless, for many applications the resolution reached in the SEM is sufficient.

In experiments of electron-light-matter interaction, it is useful to define the spatial frequency caried by the electron, $q = \omega/v$, with v the velocity of the electron, ω the frequency of the light. When q is matched to the excited mode, the interaction between the electron and the mode can be optimized. Figure 1.2b shows that the wider range of spatial frequencies accessible in the SEM is much higher than that in the TEM. This is the result of the fact that the electron velocity converges to the speed of light at high electron energies. The large range of spatial frequencies offered by electrons with energy in the range of 1 and 30 keV makes the SEM more suitable for phase-matching conditions, where the velocity of the electron matches the temporal field evolution of the excited optical mode.

In recent years, performing scanning transmission electron microscopy (STEM) in the SEM has become increasingly popular[74, 75]. The increasing scattering cross

section with decreasing electron energy proves to be both beneficial and disadvantageous. For thin samples, such as van der Waals materials, it yields higher image contrast. For thicker specimens, however, multiple scattering events become more prominent, complicating data interpretation. Finally, the use of lower electron energies reduces knock-on damage, where lattice atoms are displaced by incident electrons[76].

1.5. Motivation for this work and outline

In this thesis we investigate the use of scanning electron microscopy to study optical properties of nanomaterials at the nanoscale. We explore how we can use CL spectroscopy in an SEM to reconstruct electric near fields in three dimensions (3D). In **Chapter 2** we control the coupling between the e-beam and a dipolar plasmon mode in a Au nanoparticle by varying the electron velocity. We demonstrate how we maximize the coupling, and thus the CL emission, by phase-matching the electron velocity to the time evolution of the dipolar mode. The electron-energy dependent coupling strength directly represents the Fourier transform of the electric near field along the electron trajectory at spatial frequency q determined by the velocity of the electron. In non-aloof geometries, the phase-matching model does not fit due to inelastic scattering and we develop a recoil model that fits the experiments well.

To further investigate the phase-matching and electric near-field reconstruction, we study Mie resonances in Si nanoparticles. These particles offer two main advantages over plasmonic particles made of noble metals: (1) the lighter atoms have a smaller inelastic scattering cross section, and (2) Mie modes show many resonances over the entire spectrum that can be tuned by changing the particle's diameter, creating control over the near field distribution. In **Chapter 3**, we show that we can reconstruct the impact-parameter-dependent path length inside the particle by analyzing the coupling strength of the electron to the electric dipole mode. Moreover, by systematically varying the electron energy and impact parameter, we can selectively excite specific Mie modes. Since the resonances are coherently excited, they interfere in the far field, allowing us to control the angular emission distribution. By controlling constructive and destructive interference between electric dipole and magnetic dipole modes we achieve directional emission, similar to the Kerker effect used for optical metasurfaces[77].

Next, in **Chapter 4** we expand our perspective towards using CL as a metrology technique. Earlier research has shown that if an electron excites a plasmonic surface, it simultaneously creates free-space transition radiation (TR) and launches guided surface plasmon polaritons (SPPs). If the SPP encounters a scattering defect or particle on the surface, light can scatter out and interfere with the TR[78]. In this thesis, we investigate CL interference from scatterers that are sequentially excited by the same electron. Since the excitation of both scatterers have a well-defined phase relation with passing of the electron, their CL emission also has a mutual phase relation, producing spectral and angular interferences in the far field. Analyzing the interferograms through Fourier transformations allows us to extract

the spacing between the sources, the time-of-flight of the electron to travel from one scatterer to the next, and the decay time of the resonant optical modes. Our experiments match very well with an analytical model that we further corroborate by performing polarization-resolved measurements.

In **Chapter 5**, we explore conditions under which the wave-nature of the electron may affect the interaction that leads to CL by studying the lateral coherence properties of the e-beam. We demonstrate that, when the e-beam extends laterally far enough to interact with several scatterers at once, the resulting emission arises from an incoherent superposition of the individual excitation contributions. This indicates that in these experiments, the CL emission is insensitive to the transverse structure of the e-beam. Further experiments are required to clarify whether this is due to the finite lateral coherence of the e-beam or that this represents a more fundamental limitation of coherent free-electron plasmon excitation.

To prepare for such investigations we study diffraction of electrons in a STEM geometry in the SEM at 30 keV. In **Chapter 6**, we use single-crystalline Au flakes and monolayers of graphene, to show SAED, and CBED, respectively. We develop a method, adapted from techniques used in TEMs, to measure the degree of spatial coherence. We measure CBED patterns of a twisted bilayer of graphene and find a degree of spatial coherence of 60 % between two wave vectors separated by $0.031\,\text{Å}^{-1}$.

Overall, this thesis studies fundamental aspects of the coupling between high-energy electrons and resonant optical modes in nanostructured geometries. It gives insight into the retrieval of 3D distribution of optical near fields in individual nanostructures and multiple spatially separated structures. Furthermore, it introduces the first step toward measuring spatial coherence in an SEM and explores how it affects coherent CL emission of resonant and non-resonant nanostructures. This thesis presents the first steps towards the use of coherent CL in 3D metrology and reports the first explorations towards the study of quantum-coherent measurements using CL in the SEM.

2

Free electron-plasmon coupling strength

In this chapter, we use electron-energy-dependent CL spectroscopy to study the tightly confined dipolar mode in plasmonic Au nanoparticles. Tightly confined optical near fields play a pivotal role in important applications ranging from optical sensing to light harvesting. To measure the optical near fields, energetic electrons are ideally suited by collecting the resulting cathodoluminescence (CL) light emission. Intriguingly, the CL intensity strongly depends on the near-field profile along the electron trajectory and the optimum coupling strongly depends on such fields. These mechanisms remain experimentally unexplored.

By systematically scrutinizing Au nanoparticles with diameters in the range of 20-100 nm, using electron energies from 6-30 keV, we determine how the coupling between swift electrons and optical near fields depends on the energy of the incoming electron. The strongest coupling is achieved when the electron speed equals the mode's phase velocity, meeting the so-called phase-matching condition.

In aloof experiments, the measured data are well reproduced by electromagnetic simulations, which explain that larger particles and faster electrons favor a stronger electron-near-field coupling. For penetrating electron trajectories, scattering at the particle produces severe corrections of the trajectory that defy existing theories based on the assumption of non-recoil condition. Therefore, we develop a first-order recoil correction model that allows us to account for inelastic electron scattering, rendering better agreement with measured data. Finally, we consider the albedo of the particles and find that, to approach unity coupling, a highly confined electric field and very slow electrons are needed, both representing experimental challenges. Our data paves the way towards unity-order coupling between free electrons and confined excitations, helping us to understand fundamental aspects of light-matter interaction on the nanoscale.

2.1. Introduction

Understanding the nanoscale distribution of light fields in the optical spectral range is of great importance in many technologies. For example, in photovoltaics, nanoscale near-field scattering determines the light trapping efficiency[3, 5], in photochemistry the strength of surface modes determines the efficiency of generating chemical fuels[10, 79], and in integrated optics near-field coupling determines the propagation and coupling of optical signals[80]. Noble-metal and dielectric nanostructures support strong plasmonic and Mie resonances that can be geometrically tailored to better trap light, or more effectively capture heat[81]. Their optical near fields are tightly confined to the nanoparticle surface within a typical range of 10-50 nm[82]. To design these nanostructures, it is crucial to have a method to probe the electric near-field distributions at the nanoscale. However, probing the amplitude and phase of the electric near field is proven to be challenging with optical techniques because it displays small features, far below the optical diffraction limit. In recent years, high-energy (1 −200 keV) electron beams (e-beams) have emerged as unique probes of optical near fields[83–85]. Energetic electrons act as a broadband excitation source, which, due to their small de Broglie wavelength (39 −2.5 pm for 1 −200 keV electrons) and the numerical aperture of an electron microscope, can be spatially positioned with far better resolution than light[82].

Although the absorption or emission of a net number of photons by an electron is kinematically forbidden in free space, an energetic electron passing near or through a polarizable structure can efficiently couple to the near-field components of electromagnetic modes which, in turn, can radiate to the far field. The interaction of the electron with the induced optical near field can be sensitively probed by measuring the electron energy in electron energy-loss spectroscopy (EELS)[86], while cathodoluminescence (CL) spectroscopy relies on the study of the emitted radiation, which is collected in the far field[40]. The inverse process (far-field photons illuminating a structure and coupling to the electron through the induced near fields) has emerged as an exciting approach to gain control over electron-light-matter interaction in the so-called photon-induced near-field electron microscopy (PINEM) technique, which leverages the near field created by an intense external laser to dramatically enhance the interaction strength[46]. Such strong coupling then reshapes the electron wave function into a superposition state observed with an electron spectrometer as a set of energy-loss and -gain sidebands corresponding to the emission or absorption of one or more photons. In this context, control of the optical near-field distribution provides a unique way to tailor the electron wave function[56, 87].

In all three techniques, EELS, CL, and PINEM, the electron-near-field interaction strength for an electron moving along the z direction is determined by the spatial distribution of the z-component of the electric field $E_z(z)$ that is probed. Yet, so far, a detailed experimental study of the electric near field along the electron trajectory and its associated coupling strength have remained missing. EELS, CL, and PINEM

investigations of near fields have focused mostly on acquiring maps of the near-field strength in the x-y plane (i.e., perpendicular to the incident electron direction), integrating the electron-near-field interactions along the z axis. For example, EELS and CL measurements showed x-y maps of the resonant modes of plasmonic nano-triangles and nanowires with ultra-high spatial resolution[34, 88]. Likewise, CL and PINEM measurements have revealed x-y maps of the transverse-electric modes in photonic crystal cavities[89, 90]. In 3D reconstruction techniques, like electron tomography, information about the third dimension can be obtained by rotating the sample and subsequent numerical processing[91], as exemplified by Nicoletti *et al.*,[92] who visualized the 3D distribution of localized surface plasmon resonances in Au nanocubes using EELS, and also by Atre *et al.*[93], who demonstrated the 3D and spectral reconstruction of nanocrescents using CL. However, the reconstruction of the actual electric field is not a trivial task and has only been tackled partially with these different techniques. The near field has three spatial components, each of them complex for each optical frequency. In addition, the electron only couples to the field component along the e-beam direction.

In this chapter, we leverage the electron-energy dependence of CL spectra to experimentally study tightly confined plasmonic optical near fields in Au nanoparticles. Specifically, we investigate spherical plasmonic Au nanoparticles with diameters in the 20 −100 nm range. We address the question of how the coupling strength depends on electron energy, the induced near-field distribution, and the dependence on e-beam position (impact parameter). From this, we derive previously inaccessible spatial information on the induced electric near field along the z direction (i.e., the e-beam direction). We study the coupling strength between Au nanoparticles and electrons with energies in the range of 6 −30 keV in two different configurations: aloof excitation, in which the electron passes close to the particle (grazing with respect to the surface); and penetrating excitation, where the electron passes through the center of the particle. In agreement with theory, we find that faster electrons couple better to optical near fields described by lower spatial frequencies. Additionally, we introduce a first-order recoil correction to the coupling strength for penetrating electrons, accounting for the strong effect of elastic and inelastic electron scattering inside the particle. Finally, by correcting for the plasmonic scattering efficiency of the nanoparticles, we extract absolute values for the electron-to-near-field coupling. Overall, the data provide insight into the electron-energy dependence and optimization of electron-plasmon coupling, the near-field distribution, and the subsequent CL emission. Our data are relevant to tailor electron-light-matter interactions in CL, EELS, and PINEM experiments, especially when specific conditions of strong coupling are sought.

2.2. Theory

Fundamentally, EELS, CL, and, PINEM signals are governed by the coupling dynamics between individual free electrons and the induced electric field by the bare field of the moving electron (EELS, CL) or by an external laser pulse (PINEM). In

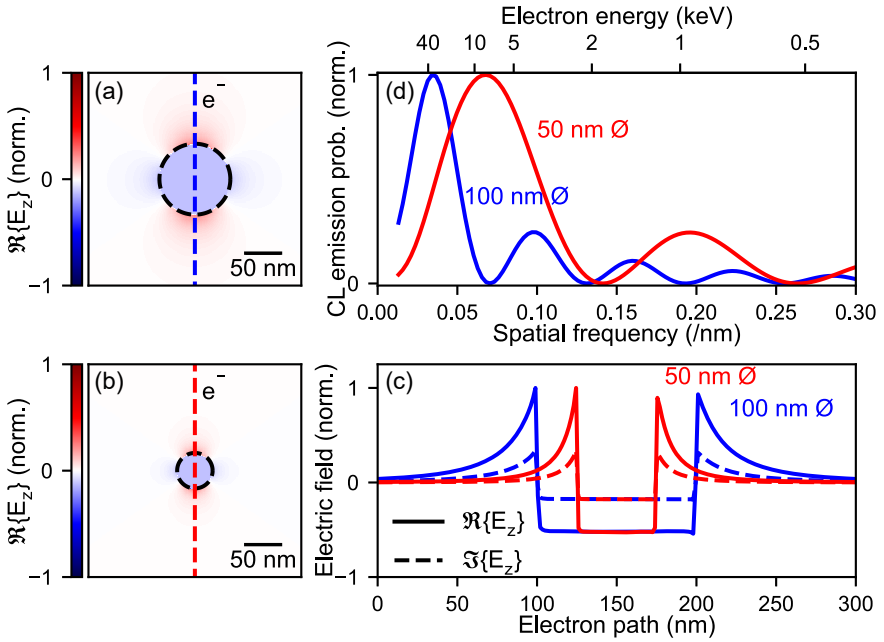

Figure 2.1: (a-b) Electric field of a z-oriented plasmonic dipole induced by a plane wave at 530 nm in (a) a 100 nm and (b) a 50 nm diameter Au spherical particle, calculated using BEM[94, 95]. (c) Real (solid) and imaginary (dashed) parts of the z-component of the electric field along the z axis for $x, y = 0$ in particles of 100 nm (blue) and 50 nm (red) diameter. (d) Square modulus of the spatial Fourier transform of the complex z component of the electric field in panel (c), which is proportional to the CL emission probability.

the non-recoil approximation (i.e., assuming the electron velocity vector remain unchanged during the time of interaction), the CL emission probability (Γ_{CL}) for a single mode excited by an electron moving at a constant speed v along the z direction is proportional to the work done by the electron on the optical modes of the system along its trajectory [83, 84, 96, 97],

$$\Gamma_{\mathrm{CL}}(\mathbf{R},\omega) = \frac{2e^2\omega^3}{3\pi\hbar c^3} A|f(\omega)|^2 \left| \int dz E_z(\mathbf{R},z) e^{-i\frac{\omega}{v}z} \right|^2, \tag{2.1}$$

with E_z denoting the z-component of the induced electric near field along the e-beam trajectory, $\mathbf{R} = (x, y)$ the impact parameter of the electron, ω the resonance frequency of the excited mode ($\omega = \frac{2\pi c}{\lambda}$), e is the electron charge, $f(\omega)$ is the frequency dependent polarization function, and A entails the radiative efficiency of the mode ($A = 1$ for a dipolar mode). From a classical perspective, this expression can be understood as the effect of an alternating acceleration and deceleration of the electron as it passes through traverses the induced electric near field, with a net deceleration resulting in energy loss and subsequent emission of radiation. Equation 2.1 shows how Γ_{CL} directly represents the Fourier transform of E_z at a spatial

frequency $q = \frac{\omega}{v}$. This implies that a near-field distribution that is phase-matched with the passing electron (i.e., fields characterized by a central wave vector centered near $\frac{\omega}{v}$) leads to the strongest CL intensity. Consequently, slow electrons (high q) induce CL mostly for near-field distributions with large spatial frequencies, corresponding to small spatial features, while fast electrons couple best to near-field components with small spatial frequencies. So far, no CL experiments have systematically studied these trends.

We start by examining the theory for the excitation of a dipolar plasmonic mode in a Au spherical nanoparticle. Figure 2.1 shows the amplitude of the real part of E_z for a dipolar mode in Au nanospheres of (a) 100 nm and (b) 50 nm diameter placed in vacuum and excited by a light plane wave at the resonance wavelength of 530 nm. The electric fields are computed through a robust numerical solution of Maxwell's equations based on the Boundary Element Method (BEM)[94, 98]. We consider the excitation of this dipolar mode by a fast electron penetrating the particle along the central particle axis (dashed line). The dipolar field profile that is induced by the electron, and acting back on it, along the trajectory is shown in Figure 2.1c, for both particle sizes. Both cases show a homogeneous field inside the particle and a strong, highly confined near field at the edge of the particle. Following eq. 2.1, we take the Fourier transform of the E_z profiles in Figure 2.1c to calculate the CL emission probability as a function of the spatial frequency q carried by the electron (Figure 2.1d). The corresponding electron energy is shown on the top axis. For resonances in the optical range, we corroborate that fast electrons ($30-40$ keV) induce CL mostly for near-field distributions with small spatial frequencies, corresponding to the larger features in the 100 nm diameter particle. In contrast, slower electrons couple best to near-field components with higher spatial frequencies (small features). Figure 2.1d also reveals that, to achieve a maximum of CL emission for a dipolar mode, the spatial electron frequency q should match the excited mode, such that $q \approx (2n+1)\pi/D$, with n an integer and D the diameter of the particle. For a 100 nm particle, the dipolar mode is optimally excited with an electron carrying a spatial frequency $q = 0.03\,\mathrm{nm}^{-1}$ (30 keV for λ=530 nm), while $q = 0.06\,\mathrm{nm}^{-1}$ (8 keV) is best for a 50 nm diameter particle. We stress that these electron energies are all accessible in a standard scanning electron microscope (SEM).

To experimentally study the strength of the coupling between electrons and plasmonic nanoparticles, we perform CL measurements in a SEM operating at acceleration voltages of $4-30$ keV. The SEM is equipped with a CL collection system consisting of a half-parabolic mirror and an optical spectrometer. The mirror is positioned between the electron column and the sample plane. Using a micro-actuation stage, the focal point of the mirror is aligned with the e-beam and the emitted light is directed through a vacuum port onto an optical spectrometer. To minimize the influence of the substrate, single-crystalline Au nanospheres are drop-casted on a 15 nm thin Si_3N_4 membrane and cleaned using an oxygen plasma to remove the PEG carboxyl ligands (see section 2.5.5). We measured the CL spectrum for particles of 20 nm to 100 nm diameter in two configurations: a penetrating e-beam configuration, described above, and an aloof configuration in which the

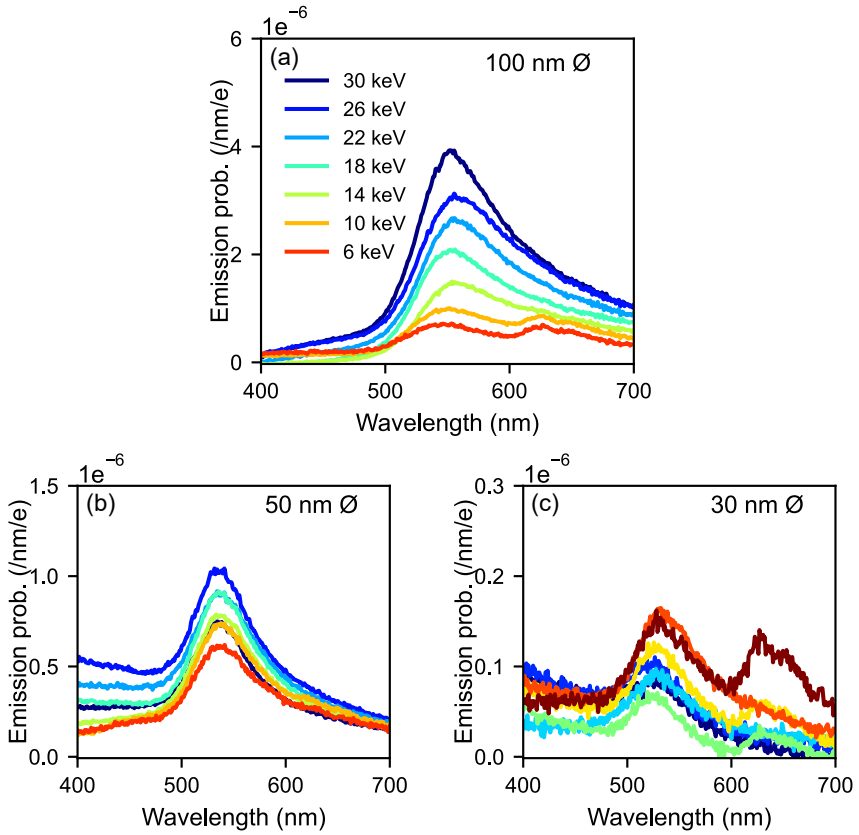

Figure 2.2: Measured CL emission probability for Au spheres of (a) 100 nm, (b) 50 nm, and (c) 30 nm diameter, excited by 6 −30 keV electrons (dark red to blue, respectively), which graze the particle at a distance of 5±2.5 nm.

electron is passing near the particle at a distance of 5 ± 2.5 nm from its surface. For every particle diameter, the electron energy is decreased from 30 to 6 keV, and every measurement is repeated five times on an unexposed particle. Additionally, we measured the angular emission profile of the dipolar mode and observed the characteristic emission for a dipole mode (data not shown). To complement our data, we use BEM simulations and the analytical dipole model.

2.3. Results

2.3.1. Aloof configuration

Figure 2.2 shows the measured CL spectra for aloof excitation of Au particles with diameters of (a) 100 nm, (b) 50 nm, and (c) 30 nm for electron energies in the 4 to 30 keV range. We refer to section 2.5.6 for details on the spread in the measure-

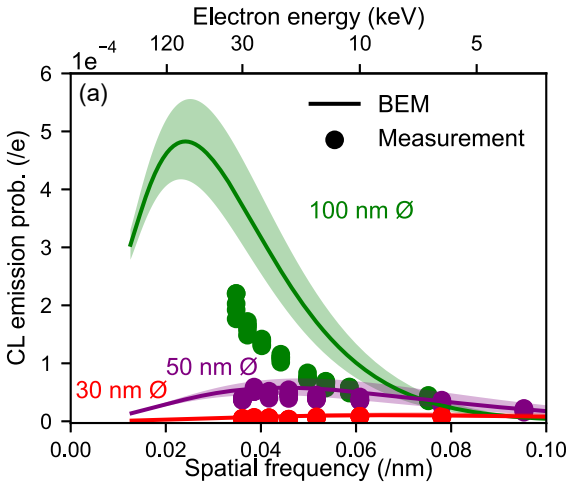

Figure 2.3: Measured (dots) and simulated (solid) CL emission probability for aloof excitation of Au nanospheres with a diameter of 100 nm (green), 50 nm (purple), and 30 nm (red). The emission probability from Figure 2.2 is integrated over a bandwidth of 60 nm around the peak wavelength in the spectra of Figure 2.2. The bandwidth around the solid line shows the uncertainty of the impact parameter, which is estimated as $b = 5 \pm 2.5nm$. Figure 2.9 shows the same data on a logarithmic scale to reveal details in the lower-signal data.

ments and comparison to BEM simulations. All spectra exhibit a strong dipolar resonance at an emission wavelength of 550 nm, varying in intensity with electron energy. While the intensity for the largest particle monotonically increases with electron energy up to 30 keV, we observe a maximum for the 50 nm diameter particle at 26 keV electron energy. For the smallest particle, no clear trend can be observed because of the large relative error in the measured spectra (note the difference in vertical scale for the three different particle sizes). Furthermore, the spectrum first shows a slight redshift with decreasing electron energy and then a blueshift. This is due to the small irregularities in particle shape that cause the peak to shift. In some measurements for slow electrons and small particles, we observe a spectral feature around 650 nm superimposed on the plasmon spectrum. We ascribe this feature, which does not depend on particle size, to emission from carbon deposited as a result of exposure to the e-beam.

To compare the trends in Figure 2.2 to theory, we integrate the plasmon peak over a 60 nm bandwidth around the peak wavelength. We plot the resulting emission probability versus the spatial frequency q carried by the electron, for the three particle sizes in Figure 2.3 together with BEM simulations for the same geometries. Overall, the decreasing trend of CL emission with spatial frequency is well represented by the data for the 100 nm diameter particles. However, if we compare the absolute values measured in the experiments with the BEM simulations, we see that, for the 100 nm diameter particles, this is half of the value that BEM pre-

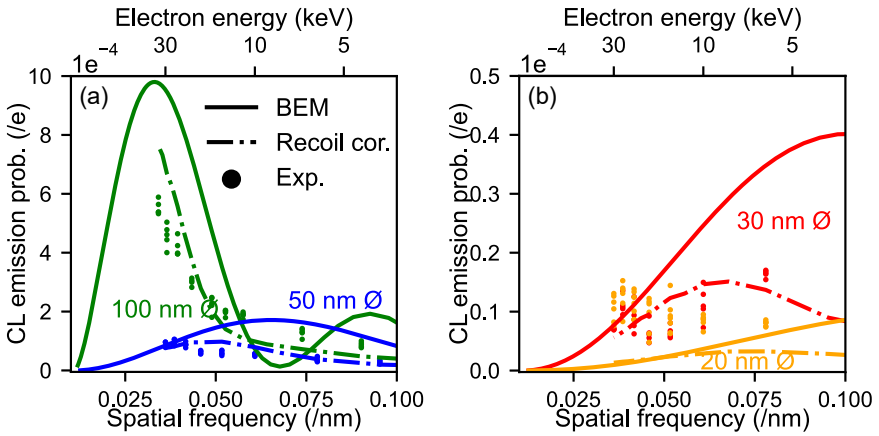

Figure 2.4: Measured (dots) and simulated (solid) CL emission probability for electrons passing through the center of Au nanospheres with a diameter of 100 nm (green) and 50 nm (purple) in (a), and 30 nm (red) and 20 nm (blue) in (b). The emission probability is integrated over a 60 nm bandwidth around the peak wavelength. The dashed curves show the CL emission probability calculated using a recoil correction on Eq 2.1, taking into account the penetration depth of the electron, normalized to the analytical non-recoil calculation (see section 2.5.2).

dicts. We attribute this discrepancy to the interaction with the substrate, which is not incorporated in the BEM simulations. A substrate can cause a large part of the light to be emitted into the substrate, reducing the intensity that is collected by the parabolic mirror. In the 50 nm diameter particles, a maximum coupling strength is found at $q = 0.04\,\mathrm{nm}^{-1}$, representing the fact that these particles have display a more tightly confined near field with less prominent low-q components. No clear trend is observable for the 30 nm diameter particles.

2.3.2. Penetrating configuration

Next, we investigate the coupling strength of electrons to plasmonic modes for excitation along the particle axis. Figures 2.4a,b show the CL measurements versus electron energy for particles of 100 nm (green) and 50 nm (purple) diameter, and 30 nm (red) and 20 nm (blue), respectively (see Figure 2.10 for the spectral data). BEM simulations show the same behavior predicted from the analytical description above, with maximum CL emission probability where the spatial frequency matches the excited mode such that $q = \frac{\pi}{D}$. However, in contrast to the data for aloof excitation in Figure 2.3, we observe significant differences between experiments and simulations: firstly, for the largest particle, BEM simulations show an emission probability that is roughly twice larger than the one measured for high electron energies; and secondly, for the 50 nm diameter particles, the recorded spectra show a reduced coupling with increasing q, while the simulations predict an increase up to q =0.07 nm^{-1}. Most notably, the upward trend in the calculations for the 30 nm diameter particles is not seen in the experiments. We argue again that,

for the smallest particles (Figure 2.4b), the data do not reveal a clear trend due to the higher signal-to-noise ratio.

BEM simulations are based on the assumption that an electron maintains its velocity and momentum during the entire time of interaction — the so-called "non-recoil" approximation. Here, this assumption proves to be invalid because the electrons have a high probability to of undergoing elastic and inelastic collisions within the nanoparticle. We ascribe the discrepancy between the measured CL emission probability and the numerical predictions to the effect of such scattering. As a first-order correction to the model to take these recoil effects into account, we modify the integration boundaries in Eq 2.1 to include only the range of the electron trajectory inside the nanoparticle. We use Monte-Carlo simulations[99] to obtain statistics of on the penetration depth for a given electron energy. We then evaluate the integral in Eq 2.1 and normalize it to the maximum coupling efficiency found for the simulated non-recoil scenario. The data derived using this recoil-corrected model is plotted in Figure 2.4 (dotted lines) for the four particle diameters under consideration.

The recoil calculation shows a lower emission probability due to the termination of the integral, bringing the model closer to the data for the particles of 100 nm, 50 nm, and 30 nm diameter. While the BEM simulation shows a vanishing emission probability at $q = 0.07\,\mathrm{nm}^{-1}$ for the 100 nm particle because the near field does not have a component at this spatial frequency, the recoil-corrected model produces a finite probability, consistent with the measurement. This is a direct result of electron recoil, associated with the fact that the electron trajectory ends inside the particle and, therefore, does not probe the full Fourier integral through the entire particle.

This analysis shows the importance of accounting for electron recoil effects in quantifying absolute CL emission probabilities. Furthermore, it provides insight into the best conditions for coupling free electrons and nanoparticle plasmons. In brief, for the larger particles, faster electrons (energies around 30 keV) match best to the large spatial features, while for the smaller particles the electron velocity must be carefully matched to the spatial frequency. In addition, recoil, which corrects the distribution of such frequency, needs to be considered to obtain optimal coupling.

While the analysis of CL emission allows us to estimate the coupling between an electron and free electromagnetic radiation mediated by the confined excitations supported in the sample, the direct electron-mode coupling is of particular relevance in the study of electron-light correlations[100]. To estimate this quantity, we consider the plasmonic scattering albedo that is determined by the balance between radiative and non-radiative plasmon decay processes. The plasmon radiative efficiency ranges from 1 % to 30 % for particles of 30 nm to 100 nm diameter. Correcting for the albedo (see section 2.5.4), we can derive the electron-plasmon coupling strength in our experiments.
Figure 2.5 shows the CL emission probability from a BEM simulation corrected for the albedo of Au spherical nanoparticles of 10 −100 nm diameter. To study the fundamental limit of electron-plasmon coupling, we use an e-beam full-width at

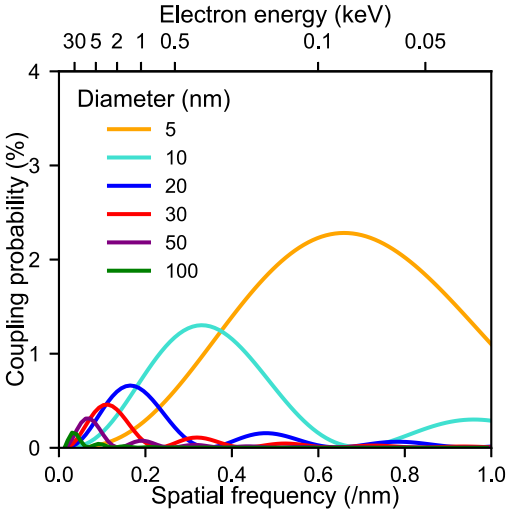

Figure 2.5: Simulated coupling probability between the electron and the induced near field in spherical Au nanoparticles with a diameter of 100 nm (green), 50 nm (purple), 30 nm (red), 20 nm (blue), 10 nm (turquoise), and 5 nm (orange) for penetrating trajectories (passing near the particle center), calculated using BEM with a FWHM of the e-beam of 0.1 nm, and corrected for the plasmon scattering albedo (see section 2.5.4).

half-maximum (FWHM) of 0.1 nm (see Figure 2.7 for an analogous calculation with a FWHM of 5 nm). This graph directly represents the electron-plasmon coupling strength. By using the results shown in Figure 2.5, we can now compare the absolute coupling strength between particles of different sizes. The spatial frequency for which a maximum coupling is observed increases for smaller particles, in agreement with the Fourier analysis described above. Furthermore, we observe that the peak in coupling strength increases with decreasing particle diameter. Quantitatively, we find a highest coupling strength of 2.5 % for a 5 nm diameter particle at an electron energy of 100 eV. Further increased coupling can be achieved for even more strongly confined near fields (<5 nm) and very slow electrons (<100 eV). Such experiments would be challenging in a SEM and inspire novel geometries where electrons are accelerated in specially tailored vacuum geometries using a strong electric field.

To further investigate the scaling properties in electron-driven resonant excitations, we performed a theoretical study of electron-near-field coupling for a range of resonant plasmonic, dielectric, and polaritonic excitations[101]. In particular, we show that a few percent coupling strength can be achieved for Au nanospheres with a diameter of 5 nm excited by low-energy electrons (1 keV). This can be further improved to unity-order coupling for ultrasmall (few nanometer diameter) resonant particles at low electron (<100 eV) energies. This is due to phase-matching (see

above) combined with the higher overall coupling strength at lower electron velocity. The insights from these calculations, combined with the experimental study in this chapter, inspire practical geometries for the use of electrons as sources for spectroscopy at the nanoscale.

2.4. Conclusion

In conclusion, we have systematically examined the coupling strength between swift electrons and the dipolar mode in Au plasmonic nanospheres for both aloof and penetrating configurations. Under aloof excitation, our measurements confirm the validity of the non-recoil approximation model. In contrast, for penetrating e-beams, the non-recoil model approximation breaks down because of the large changes produced in the electron trajectory due to elastic and inelastic scattering inside the nanoparticle, including substantial deflection and deceleration. We present a modified model, taking these recoil effects into account, and find better agreement with the measured data.

To investigate the absolute electron-to-near-field coupling strength, we corrected the simulated data for the effect of radiative losses by dividing the CL emission probability by the albedo of the particle and extrapolated this to very small particle sizes. The extrapolated data show a maximum coupling strength of 2.5 % for strongly confined near fields (<5 nm) and low-electron energy (100 eV).

These results lie at the edge of the capabilities of conventional SEMs and inspires new geometries for high-efficiency CL generation from ultrasmall optical near fields excited by using low-energy (<100 eV) electrons. Our work not only paves the way toward meeting strong-coupling conditions for electron-plasmon interaction, but it also and provides fundamental insight into the control and optimization of optical-model excitations in nanostructures, with a potential future in nanoscale optoelectronic circuits for a wide range of applications.

2.5. Appendix

2.5.1. BEM simulation

Numerical calculations were performed using the BEM[95] as implemented in the MNPBEM17 Matlab toolbox[94, 98]. Spherical nanoparticles were used and parametrized by 144 triangular face elements, with optical constants for Au taken from Olmon *et al.*[102]. For the computation of the induced dipole field inside the Au nanoparticle (Figure 2.1), a plane-wave excitation was introduced at a wavelength of 530 nm, incident along the x axis with polarization along the z axis. The induced dipole corresponds to the excited mode upon electron excitation along the z axis. For calculations of the CL emission probabilities, built-in functions were used, assuming a FWHM of the e-beam waist of 5 nm.

2.5.2. Recoil correction

Next, we incorporate the effect of electron scattering while traversing through a Au spherical nanoparticle. Eq 2.1 was corrected to truncate the integral at the penetrating depth of the electron:

$$\Gamma_{CL}(\mathbf{R},\omega) = A \sum_{z_{max}=-R}^{R} C_{z_{max}} \left| \int_{-\infty}^{z_{max}} dz E_z(\mathbf{R},z) e^{-i\frac{\omega}{v}z} \right|^2, \tag{2.2}$$

with A the proportionality factor, z_{max} the electron penetration depth, and $C_{z_{max}}$ a weighting factor describing contributions from electrons for a given penetration depth, shown in Figure 2.6. The proportionality factor A is taken equal to the one for the non-recoil picture and is used to normalize the analytical expression to data from BEM calculations.

2.5.3. Monte Carlo simulations

A CASINOv2.5 Monte-Carlo program[99] was used to obtain the distribution of electron paths in the electron cascade and determine $C_{z_{max}}$ for every electron energy and penetrating depth z_{max} considering electrons incident on a planar Au slab (density of 19.3 g cm^{-1}). The maximum depth that was reached before the electron was either backscattered or absorbed was assigned to z_{max}. If the electron passed further than the diameter of the particle, it was set to be transmitted, with $z_{max} = \infty$. Figure 2.6 shows the electron penetration statistics for an incident e-beam with energy of (a) 4 and (b) 10 keV. The inset shows the dispersion of electron trajectories due to inelastic scattering events, with the contour of a 100 nm-diameter Au particle shown as reference. We clearly see an increased interaction volume for electrons with an energy 10 keV (b) compared to electrons with an energy of 4 keV (a). Furthermore, comparing the penetration depth statistics, we see that the low-energy electrons get absorbed, while for faster electrons electron can penetrate through 100 nm of Au.

2.5.4. Albedo correction

We correct for the albedo of the particle to extract the coupling strength between the electron and the electro-magnetic modes. To account for the optical radiative efficiency of the Au nanoparticle, we compared the analytical formulation for EELS and CL emission probabilities. We used the analytical expressions obtained for an induced electrical dipole by a grazing electron, given by[59]

$$\begin{pmatrix} \Gamma_{\mathrm{EELS}}(\omega) \\ \Gamma_{\mathrm{CL}}(\omega) \end{pmatrix} = \frac{4e^2\omega^2}{\pi\hbar v^4\gamma^2} \left[K_1^2\left(\frac{\omega R_0}{v\gamma}\right) + \frac{1}{\gamma^2} K_0^2\left(\frac{\omega R_0}{v\gamma}\right) \right] \begin{pmatrix} \Im\{\alpha(\omega)\} \\ \frac{2\omega^3}{3c^3}|\alpha(\omega)|^2 \end{pmatrix}. \tag{2.3}$$

The EELS signal represents the total energy loss of the electron along the trajectory while the CL signal corresponds to the excitation fraction that is radiated toward the far field. We use this as an approximation to obtain the CL radiative efficiency (η) for penetrating trajectories, by dividing the EELS probability by the CL emission

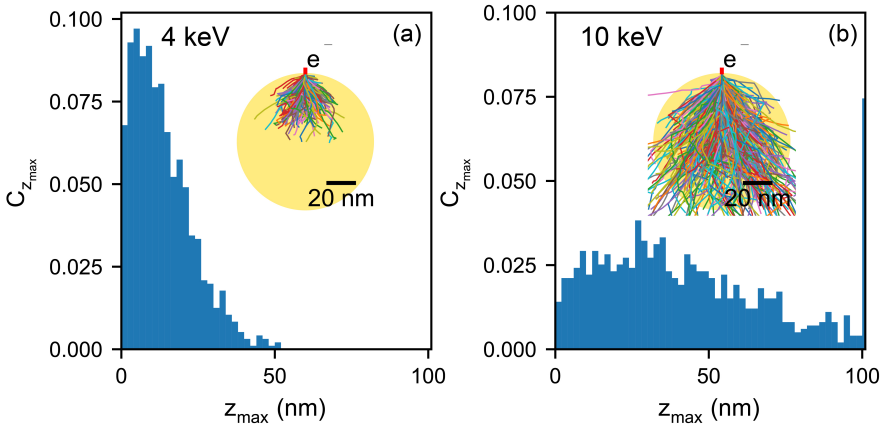

Figure 2.6: Monte-Carlo statistics of the penetration depth (z_{max}) of (a) 4 keV and (b) 10 keV electrons penetrating a planar Au surface. The insets show the dispersion of electron trajectories during propagation through the Au material. Contours of a spherical Au particle (100 nm diameter, yellow) are shown for reference.

probability, which results in

$$\eta = \frac{\Gamma_{CL}(\omega)}{\Gamma_{EELS}(\omega)} = \frac{2\omega^3|\alpha|^2}{3c^3\Im\alpha(\omega)}. \tag{2.4}$$

In the electrostatic limit ($a \ll \lambda$), the polarizability tensor, α, is given by[103]

$$\alpha(\omega) = a^3\frac{\epsilon(\omega)-1}{\epsilon(\omega)+2} \tag{2.5}$$

with a the radius of the particle and ϵ_1 and ϵ_2 the dielectric constants of the surrounding medium and the particle, respectively. However, for the used sizes of our particles, we need to use Mie theory to incorporate retardation corrections in the description of the particle polarizability, so we set

$$\alpha = \frac{3t_1^E}{2k^3}, \tag{2.6}$$

where t_1^E is the dipolar electric Mie scattering coefficient[85].

The coupling efficiency between a free electron and the electro-magnetic mode is calculated by dividing the CL emission probability by the radiative efficiency given by eq. 2.4, shown in Figure 2.5. This is calculated using a FWHM of the e-beam of 0.1 nm, in Figure 2.7 we shows the same data for a e-beam waist of 5 nm. We clearly see a decrease in coupling efficiency for small particles, due to relative size of the e-beam compared to the particle.

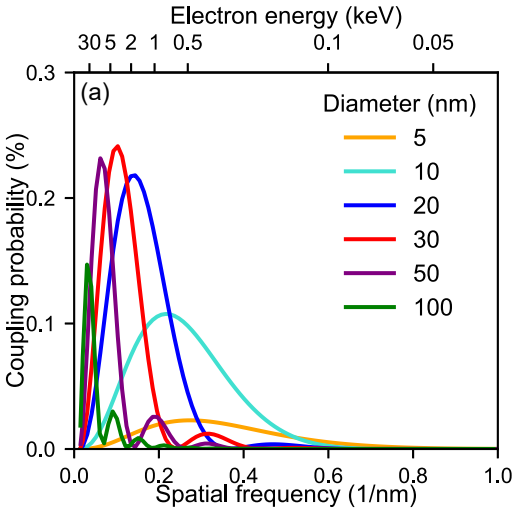

Figure 2.7: Simulated coupling probability between the electron and the induced near field in spherical Au nanoparticles with a diameter of 100 nm (green), 50 nm (purple), 30 nm (red), 20 nm (blue), 10 nm (turquoise), and 5 nm (orange) for penetrating electron trajectories, as calculated with BEM for an electron waist of 5 nm FWHM, corrected for the plasmon scattering albedo

2.5.5. Experimental setup and methods

Sample preparation

Au colloidal particles were purchased from nanoComposix (San Diego), with diameters of 20 nm, 30 nm, 50 nm, and 100 nm. The particles had PEG carboxyl ligands and were delivered as an aqueous solution with a 0.05 mg mL^{-1} concentration of Au. The particles were diluted 1 to 100 in demi water and sonicated for 2 minutes. Before drop-casting 2 µL from the suspension onto a 15 nm thin Si_3N_4 grid (Ted Pella), the surface was made hydrophilic using a UV-zone cleaner (Bio-Force UV/Ozone ProCleaner) for 10 minutes. After drop casting, the sample was cleaned with an Oxygen plasma for 2 minutes using an Oxford Instruments Plasmalab 80 Plus tool.

CL measurements

CL measurements were performed in an FEI Quanta FEG 650 SEM (Thermo Fisher Scientific Inc., MA, USA) equipped with a Schottky electron source. The CL collection system was composed of a parabolic mirror between the sample and the pole piece and collected the emitted light from the top hemisphere. The light was directed into an optical detection system (SPARC Spectral, DELMIC BV, The Netherlands)[73]. The measurements were done with an e-beam current of 230 to 1000 pA, depending on the electron energy, with an acquisition time of 0.2 s for 100 nm diameter, 1 s for 50 nm and 30 nm diameter, and 2 s for 20 nm diameter

particles. In the aloof configuration, a 2D map of the entire particle was collected using a pixel width of 5 nm. By analyzing the secondary-electron images, the pixels at 5 nm from the edge were found with an accuracy of 2.5 nm. To correct for CL background signal, dark counts were subtracted from the data for the penetrating geometry, while CL from the Si_3N_4 support membrane was subtracted from the aloof data. The system response was calibrated using the measured transition radiation (TR) of single-crystalline Al. The TR was benchmarked to an analytical expression and used to obtain the absolute CL probabilities.

2.5.6. Additional data

CL spectra in the aloof configuration

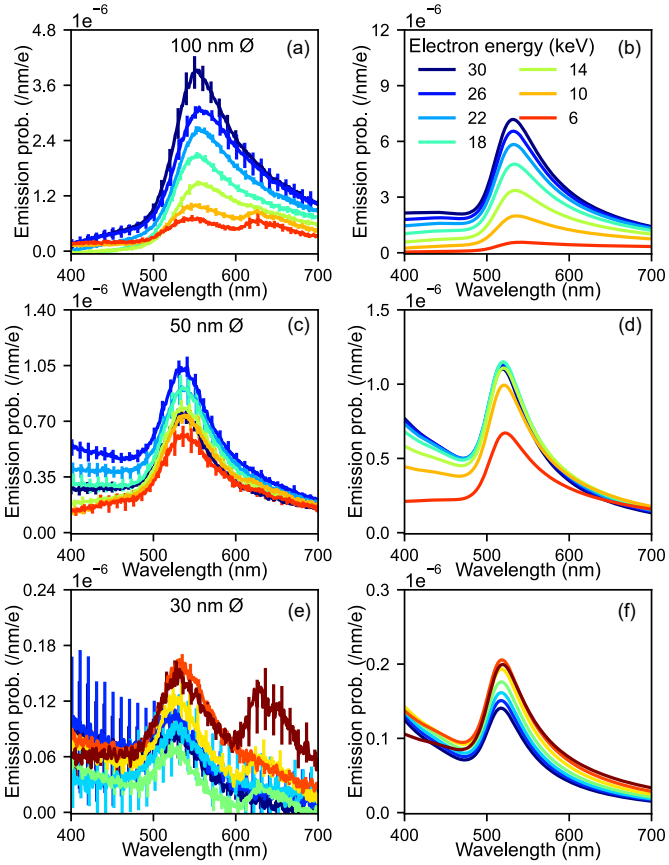

Figure 2.8: Measured (a-c) and simulated (d-f) CL spectra for particles of 100 – 30 nm diameter excited with a 6 – 30 keV e-beam in the aloof configuration (electrons that graze the particle surface). The error bars in the measured data show the variance for different measurements from spheres of the same size.

CL emission probability for the dipolar mode excited in the aloof configuration

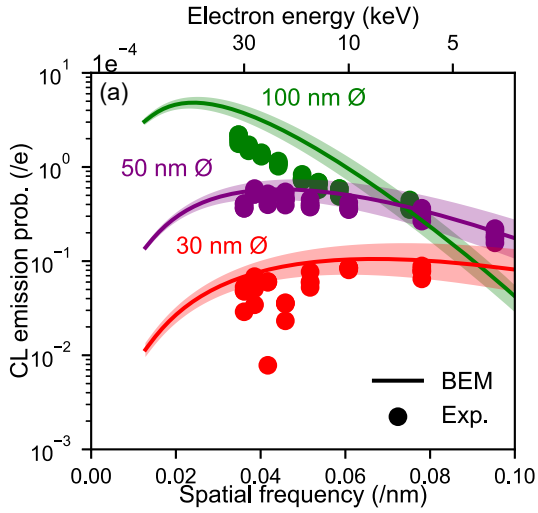

Figure 2.9: Measured (dots) and simulated (solid) CL emission probability for aloof excitation of Au nanospheres with a diameter of 100 nm (green), 50 nm (blue), and 30 nm (red). Experimental data points are obtained by integrating the emission probability spectra from Figure 2.2 over a bandwidth of 60 nm around the peak wavelength. The bandwidth around the solid curves shows the effect of uncertainty in the impact parameter, which is estimated as $b = 5 \pm 2.5$nm.

CL spectra for penetrating e-beams

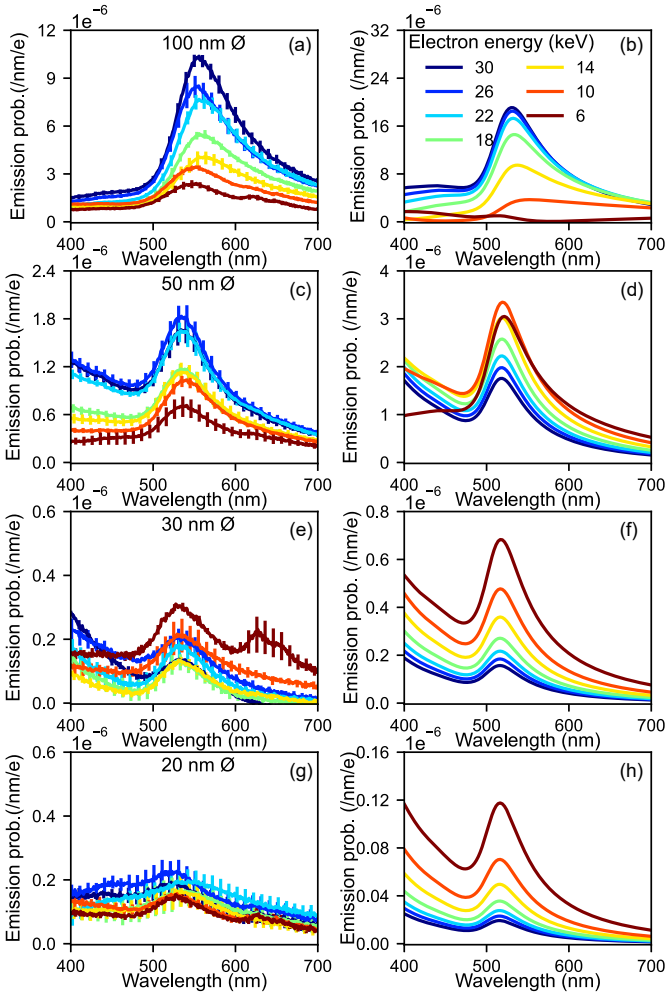

Figure 2.10: Measured (a-d) and simulated (e-h) CL spectra for particles of 100 – 20 nm diameter excited by penetrating 6 – 30 keV electrons aimed at the particle center. Error bars in the measured data show the variance for different measurements from spheres of the same nominal size.

3

Free electron-dielectric coupling for directional emission

Building on the results of the previous chapter, we explore the coupling strength of electrons to dielectric particles, which provide a complementary platform for studying confined near fields. High-energy electron beams (e-beams) with energies in the 15-30 keV range are used to excite optical Mie modes in crystalline Si nanospheres with radius 80-100 nm. Cathodoluminescence (CL) spectra show emission from resonant electric and magnetic dipole and quadrupole modes, with relative intensities that depend strongly on electron energy and impact parameter. The measured trends are explained by a coupling model in which the electron-energy dependent CL excitation probability – and thus the CL emission – is proportional to the Fourier transform of the modal electric field at a spatial frequency determined by the electron velocity. As a result, the coupling to a specific resonant mode is strongly dependent on the electron energy and the impact parameter of the e-beam. This enables the selective enhancement of CL emission from a resonant mode by phase-matching with the electron velocity. A systematic study of spatial excitation probability for the electric dipole mode as a function of electron energy further confirms the validity of the coupling model. Angle-resolved cathodoluminescence measurements show strong directional emission due to far-field interference of coherently excited Mie modes. By varying the electron energy and impact parameter the intensity and interference of these modes can be controlled and the angular distribution tailored. The insights in the localized deep-subwavelength coherent excitation of resonant Mie modes explored here are important for studies in light-emitting nanostructures, sensors, and photovoltaics, in which the interplay of local modes and far-field directional emission must be controlled.

3.1. Introduction

Controlling light in photonic nanostructures at a deep-subwavelength scale is crucial for many technological advancements, ranging from quantum technologies to solar applications[81]. In particular, directional light emission from photonic structures is important for optimizing the performance of light-emitting diodes and lasers, sensors, and photovoltaics[104, 105]. As previously shown, selective coupling to resonant optical nanoantennas provides a unique means to tailor the directionality of optical emitters[106, 107]. Both metallic and high-index dielectric nanostructures are of interest for these applications. While the former can support plasmonic resonances which are mainly governed by the material properties, high-index dielectric nanostructures are particularly interesting since they can support a wide range of Mie resonances that are electric and magnetic in nature with very low absorption losses (much lower than for plasmons) and high Q-factor (narrow emission linewidth)[19, 105, 108, 109]. Previous works have investigated the resonances of Si nanostructures due their ability to support dipolar and quadrupolar Mie modes in the visible spectral range where Si shows relatively low loss due to its indirect electronic bandgap[110, 111]. This allows for strong tunability of light-matter interactions by tailoring the size, shape and dielectric environment of the Mie particles, thereby controlling the resonant energy and angular emission distribution of the electric and magnetic multipolar modes. Furthermore, it has been shown that the interference of these multipolar modes can lead to light emission in specific directions, similar to the Kerker effect in Mie theory[112]. In order to take advantage of these properties, it is crucial to control and probe the electric fields at the nanoscale.

To study optical near fields of nanostructures at a spatial resolution below the optical diffraction limit, three different electron microscopy techniques have been developed in recent years: cathodoluminescence (CL) spectroscopy, electron energy loss spectroscopy (EELS) and, more recently, photon-induced near-field electron microscopy (PINEM). In all cases the electron is used to probe the electric field along the electron trajectory that is either induced by the electron itself (for CL and EELS) or by an external laser (for PINEM). In the case of CL and EELS, a bypassing electron polarizes the material, creating an electric near field that acts back on the electron, causing it to lose energy. The total energy loss is measured in EELS, while the radiating part can be detected in the far field as CL[84]. The CL emission from plasmonic or Mie particles has a coherent phase relation with the electron impact[40]. The advantage of CL spectroscopy is its capability to probe the electric field with nanometer precision due to the small focus dimension of the e-beam[82]. The femtosecond electromagnetic field oscillation created by a bypassing electron offers a broadband source of modal excitation, enabling broad spectral analysis in a single CL measurement[31].

In nanophotonics, CL and EELS have mostly been used to study plasmonic nanostructures[34, 84, 85, 113]. Recently, dielectric structures have also been investigated using e-beams. Coenen *et al.* characterized higher-order electric and mag-

netic Mie resonances in lithographically fabricated Si nanodisks using CL in a scanning electron microscope (SEM)[108]. Matsukata *et al.* experimentally demonstrated CL spectra of resonant modes in Si nanospheres in a transmission electron microscope (TEM) and observed strong directionality in the CL radiation[114]. And recently, Fielder *et al.* explored the interplay of Mie resonances and transition radiation in CL spectra of Si nanospheres[115]. These works show the potential of CL spectroscopy to investigate and control directional light emission. However, so far, the relation between the strength of the electron-mode coupling, the spectrum and the directionality of the CL emission in dielectric nanostructures has not been studied in a comprehensive way.

In this chapter, we demonstrate that we can achieve directionality of the emission from electron-excited dielectric resonators, showing the e-beam analogue to the Kerker effect[112] that is known from optics. It also enables us to sensitively test the model for electron-mode coupling. We investigate the coupling of the e-beam to specific resonances in individual Si nanospheres both theoretically and experimentally. We take advantage of the fact that, at a given velocity, the electron resonantly couples to specific spatial frequency components of the oscillating electric near-field distribution in the particle[116]. By varying the electron energy and impact parameter in an SEM we selectively couple to modes with specific spatial near field distributions. We then control the interference of the excited modes to create specific far-field radiation patterns. We take advantage of the spherical symmetry to exploit analytical solutions for the mode profiles from Mie theory. Our results provide fundamental understanding of electron-mode coupling and provide a framework to control and design directional light emission from single dielectric nanostructures.

3.2. Theory

Fundamentally, the electron energy loss that leads to CL is determined by the coupling between the electron and the electric near-field component in the direction along the electron trajectory. The CL and EELS spectral intensities are then proportional to the work done by this field component on the electron. In the non-recoil approximation, i.e., assuming that the electron velocity remains constant when traversing the nanostructure, the CL emission intensity (Γ_{CL}) for an electron traveling along the z-axis for a particle with a single resonant mode is proportional to[84, 96]

$$\Gamma_{\mathrm{CL}}(\mathbf{R},\omega) = \frac{2e^2\omega^3}{3\pi\hbar c^3} A|f(\omega)|^2 \left| \int dz E_z(\mathbf{R},z) e^{-i\frac{\omega}{v}z} \right|^2, \tag{3.1}$$

with $\mathbf{R} = (x, y)$ the impact parameter in Cartesian coordinates, ω the angular frequency ($\omega = 2\pi c/\lambda$), E_z the z-component of the induced electric field along the e-beam trajectory, v the electron speed, e is the electron charge, A is the radiative efficiency of a specific mode ($A = 1$ for a dipolar mode), and $f(\omega)$ is the polarizability function depending on shape and material. Classically, Eq. 3.1 can be interpreted as the net energy loss along the electron trajectory: the integrated effect of

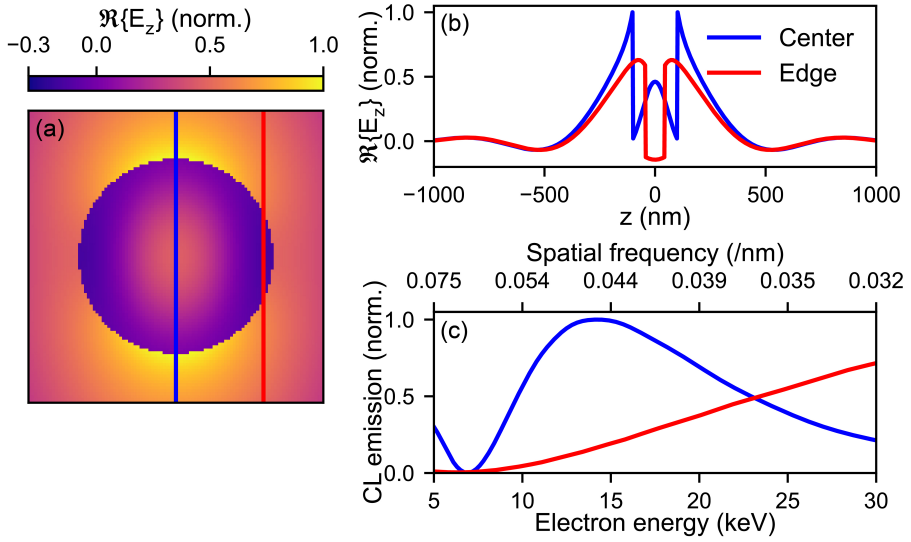

Figure 3.1: (a) Real part of the z-component of the electric field of a z-oriented electric dipole mode induced with a plane wave polarized along z at $\lambda = 600$ nm in a dielectric nanosphere with a radius $r = 100$ nm. (b) Real part of the z-component of the electric field along the electron trajectory for two e-beam impact parameters; one at $b = 0$ (blue) and the other at $b = 90$ nm (red), indicated by the lines in (a). (c) Calculated normalized CL emission intensity as a function of electron energy using Eq. 3.1. The CL emission intensity is proportional to the square modulus of the spatial Fourier transform of the z-component of the electric field for the two electron trajectories of panel (b). The top axis shows the corresponding spatial frequency ($q = \omega/v$) for $\lambda = 600$ nm.

the acceleration and deceleration of the electron caused by its interaction with the induced oscillating electric near field. The resulting absolute CL intensity is then determined by this energy loss and the nanostructure's albedo, given by the relative contribution of radiative and non-radiative losses. Eq. 3.1 shows that the e-beam effectively takes the Fourier transform of optical near fields at a spatial frequency ($q = \omega/v$): the observed coupling strength (CL intensity) at a given electron velocity then directly represents the strength of the spatial frequency q in the distribution of the near fields in the z-direction. The CL emission at a given impact parameter is maximized when the electron motion is phase-matched with the induced oscillating fields for that impact parameter. For a z-oriented dipole mode excited in the center - characterized by sharp features at the edge of the particle - the phase-matching condition is $q \sim (2n+1)\pi/D$, with D the diameter of the particle[116].

First, we theoretically study the configuration where an e-beam couples to the z-oriented electric dipole (ED) in a Si sphere with radius $r = 100$ nm. In Figure 3.1a, we show the real part of the z-component of the electric field incident at such a particle at $\lambda = 600$ nm. The induced electric fields are calculated using classi-

cal Mie theory[117] with optical constants for crystalline Si from Green *et al.*[118]. Next, we study the CL emission for two e-beam impact parameters (b) in spherical coordinates, given by the distance to the center of the particle: (1) electrons passing through the particle center ($b = 0$ nm) and (2) near the outer edge ($b = 90$ nm). Figure 3.1b shows the real part of the z-component of the induced electric field along the electron trajectory for the corresponding two impact parameters. By taking the Fourier transform of the E_z profiles, we calculate the CL emission probability associated with this mode for an electron energy in the range between 5 and 30 keV (Figure 3.1c). For electrons impacting in the center of the particle, we find a maximum CL excitation probability at 12 keV, corresponding to a spatial frequency of 0.047 nm^{-1}. Here, the electron is in phase with the excited mode (ED), causing maximal electron energy loss and hence maximum CL emission. This maximum CL excitation probability corresponds to the second-order phase-matching condition for center excitation, $q = 3\pi/D$. The first peak at lower q (higher electron energy) is found at 0.016 nm^{-1} (165 keV). For an e-beam exciting the nanosphere on the edge, no clear CL excitation probability maximum is observed in the studied range and the CL emission increases with electron energy.

The analysis in this section clearly shows that the e-beam coupling to dielectric Mie modes depends strongly on the impact parameter and electron velocity. As we will show next, this provides a unique means to tailor the coupling of the electron to specific resonant modes, thereby controlling both the spectrum and angular distribution of the CL emission. While the analysis above provides basic insight into the coupling concept, in experiments the modal field distributions depend on the electron energy and impact parameter and, due to the coherent excitation process, create modal interference in the far field. In the remainder of this work, we use the electrodynamical electron-mode coupling model to calculate the CL excitation and emission spectra and far-field angular distributions[119].

This model provides an analytical derivation for the electric and magnetic fields in the case of coherent excitation of multiple modes by an e-beam crossing the particle (see section 3.5.1). The resulting expression for the CL emission probability is a sum over the electric and magnetic modes for orders l and orientation with index m, given by

$$\Gamma_{\text{CL}}(\omega) \propto \sum_{l=1}^{\infty} \sum_{m=-l}^{+l} \left(\left| b_{lm}^{\text{II}} \right|^2 + \left| a_{lm}^{\text{II}} \right|^2 \right), \tag{3.2}$$

where b_{lm}^{II} denote the magnetic and a_{lm}^{II} the electric modes of the scattered electromagnetic field in the far field. Mode indices refer to the mode order – $l = 1$ for magnetic or electric dipole modes (MD, ED), $l = 2$ for electric and magnetic quadrupole modes (EQ, MQ) – and orientation (for an out-of-plane dipole, $m = 0$, and for an in-plane dipole, $m = \pm 1$).

Using this model, we can calculate the CL spectra for Si nanoparticles, and decompose it into the contributions from each mode. Figure 3.2 shows the CL spectrum for a 96 nm radius Si particle, excited at 86 nm from the particles center. We clearly see the very sharp electric and magnetic quadrupolar modes at low wavelength,

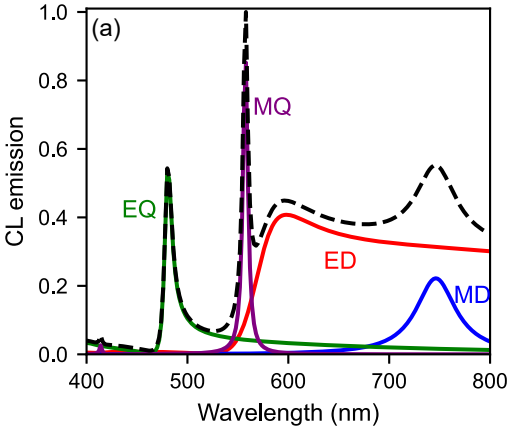

Figure 3.2: Calculated CL spectra for a 30 keV e-beam exciting a Si nanosphere with a radius of 96 nm at an impact parameter of 86 nm. The CL spectra are decomposed in the contribution of the different modes, and in black dashed the total spectrum with $l_{max} = 2$.

and the broader dipolar modes at higher wavelengths. Furthermore, we see that while the magnetic modes have a symmetric Lorentzian shape, the electric modes are asymmetric and have a tail towards higher wavelength.

3.3. Results

Single-crystalline Si nanospheres with radii between 80 and 100 nm were fabricated using the method developed by Sugimoto *et al.*[120] and deposited on a 15 nm thin Si_3N_4 TEM membrane (see section 3.5.5). CL experiments were performed using a SEM operating at acceleration voltages in the range of 15–30 keV. A half-parabolic mirror placed between the sample and the electron column collects the emitted CL and directs it to a spectrometer for spectral analysis. Angle-resolved CL was recorded in Fourier mode by projecting the emission on a CCD imaging sensor, using a 50 nm wide bandpass filter (see section 3.5.5).

3.3.1. CL spectral maps

First, we study the CL emission for a Si nanosphere with a radius of 96 nm, excited by a 30 keV e-beam. Figure 3.3a shows the measured and calculated CL spectrum at $b = 86$ nm using Eq. 3.2. The experimental spectrum is corrected considering the collection efficiency of the parabolic mirror and the spectrometer. In the spectra, we find four clear peaks, corresponding to the different modes supported by the Si nanosphere. Experimentally, we find peaks corresponding to MD at $\lambda = 744$ nm, ED at $\lambda = 605$ nm, MQ at $\lambda = 563$ nm, and EQ at $\lambda = 487$ nm. For all experimental resonances, the peak energy is redshifted compared to the theoretical ones. We ascribe this to the effect of mode coupling to the Si_3N_4 substrate[77, 121]. We observe good agreement between experiments and theory for the trend in linewidth of the

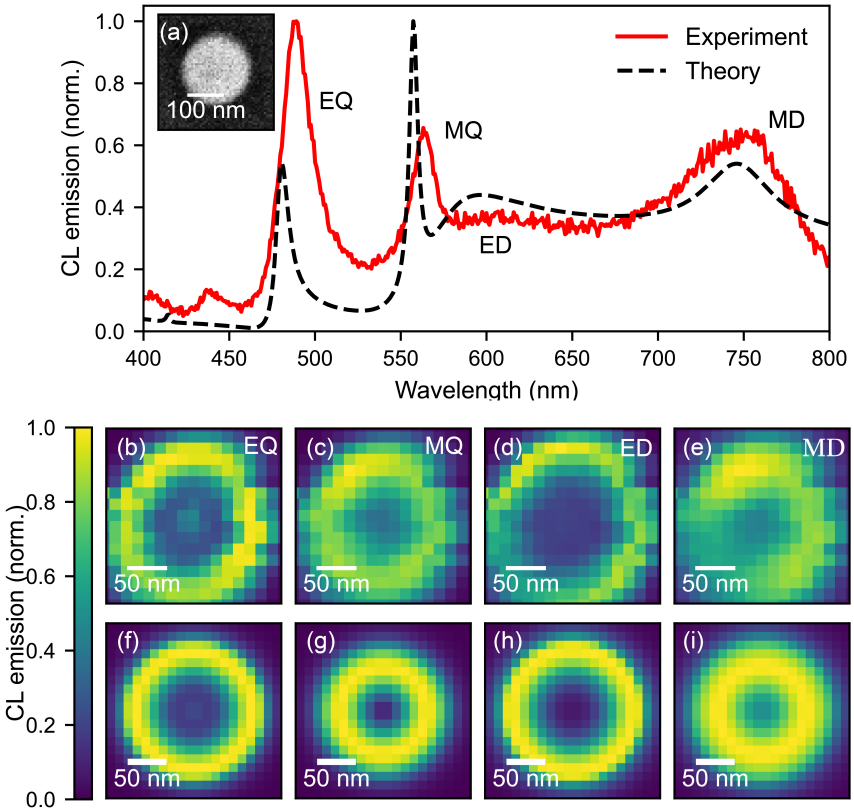

Figure 3.3: (a) Measured (red) and calculated (dashed black) CL spectra from a $r = 96$ nm Si nanosphere excited with 30 keV electrons. The measured spectrum is taken at $b = 86 \pm 5$ nm, while $b = 86$ nm is used for the calculated spectrum. The inset shows the SE image of the Si nanosphere with the red dot indicating the position of the e-beam excitation for the experimental spectrum ($b = 86 \pm 5$ nm). (b-e) Measured and (f-i) calculated CL maps at the resonance wavelengths of the different multipoles. The measured CL maps are averaged over a bandwidth of 4 nm with the center wavelength of 487 nm (EQ), 563 nm (MQ), 605 nm (ED), and 744 nm (MD). The theoretical CL maps are calculated using Eq. 3.2 considering all modes until $l_{max} = 2$ and for wavelengths of 450 nm, 557 nm, 595 nm, and 745 nm, respectively. Pixel sizes of 14 nm for the experimental and 12 nm for the theoretical CL maps are used, respectively.

modes, where quadrupolar modes exhibit narrower resonances compared to the broader dipolar modes. The modal intensities for ED and MD modes show a similar trend for experiment and theory, while an opposite trend is observed for the EQ and MQ modes. The experimental EQ mode is more intense than the MQ one, while theory shows the opposite. We primarily attribute this discrepancy to the increase of the absorption coefficient of Si below λ = 500 nm due to the direct bandgap at 450 nm, which strongly reduces the calculated intensity at that wavelength. In Figure 3.3b-i, we display the measured spatial distribution of the CL intensity for the same nanosphere for each of the Mie modes in (a). We show the CL intensity at the center wavelength of the four resonances. The experimental data (b-e) are averaged over a 4 nm bandwidth at λ = 487 nm (EQ), λ = 563 nm (MQ), λ = 605 nm (ED), and λ = 744 nm (MD). The corresponding theoretical data (f-i) are calculated at the peak wavelengths of 450 nm, 557 nm, 595 nm, and 745 nm, for EQ, MQ, ED, and MD, respectively.

CL analysis is an excitation spectroscopy technique in which the electron excitation is spatially well defined and the spatial resolution in the CL excitation maps is determined by the electron trajectory. The CL emission is collected from the entire particle within the focal collection area and numerical aperture of the parabolic mirror. The resolution of the SE image in the inset of Figure 3.3a is much higher than the CL resolution. SEs mainly originate from the surface of the sample, resulting in an estimated spatial resolution of 1–2 nm. This allows accurate determination of the radius of the Si nanosphere with simple post-processing.

The CL maps in Figure 3.3 show that e-beam excitation results in characteristic spatial excitation distributions for the different Mie modes, similar to previous findings[114, 122]. Many trends in the measured maps match well with the calculated CL emission maps. For all modes, the excitation efficiency is highest at the edge of the particle, in both experiment and theory. Small features such as the larger area of reduced intensity in the center for the ED mode are also observed theoretically and experimentally. The theoretical ED and EQ modes show higher intensities at the edges compared to MD and MQ modes; this is also visible in the measurements. The sharply concentrated ring in the experiment of Figure 3.3d directly shows the high lateral spatial resolution of the CL measurement. From comparison with the theoretical map, we derive that the spatial resolution is better than the pixel size in these experiments (i.e., below 14 nm). This is due to the e-beam focal diameter on impact (~5 nm) and small straggle of the e-beam due to inelastic scattering, consistent with Monte Carlo simulations of electron trajectories for the studied geometry. The non-spherical shape of the CL maps is attributed to small sample drift during measurements. Further asymmetries in the measurements are due to the asymmetry of the parabolic mirror light collection geometry, making CL collection efficiency for each mode dependent on its angular emission distribution. This effect is visible in the CL maps for the ED and MD modes, for which the bottom left corner is slightly dimmer: CL generated in that area beams towards the mirror's opening and is therefore only partly collected.

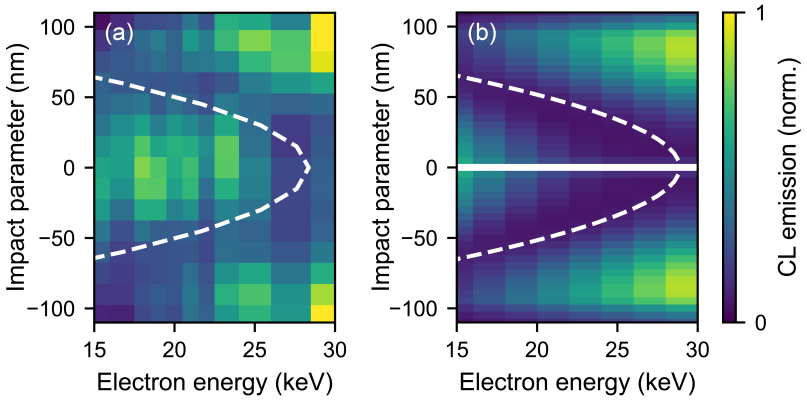

Figure 3.4: (a) Measured and (b) calculated CL maps obtained by a crosscut through the center line of a Si nanosphere of $r = 96$ nm excited with electron energies ranging from 15 to 30 keV. The experimental data are collected at a center wavelength of 605 nm with a 4 nm bandwidth. The theoretical calculations are performed at the ED resonance wavelength, $\lambda = 595$ nm, using Eq. 3.2 considering all modes until $l_{\max} = 2$. The white dashed line in experiments and theory shows the rule-of-thumb for the expected minima of the phase-matching condition for the ED, $q \sim 2n\pi/D^*$, for $n = 2$ and with D^* the height of the particle at a certain impact parameter (for a spherical particle with radius R, $D^* = 2\sqrt{R^2 - b^2}$).

3.3.2. Electron-energy dependent CL

The good agreement between experiment and theory now allows us to study the effect of electron energy on the electron-mode coupling and assess the spatial frequency formalism for resonant modal excitation as described above. To do so, we study the dependence of CL emission on the electron energy ranging from 15 to 30 keV, corresponding to a spatial frequency range of 0.044–0.032 nm^{-1} at the ED resonance wavelength (for electron-energy dependent spectra, see Figure 3.9). Figure 3.4 shows the experimental (a) and theoretical (b) CL maps as a function of electron energy and impact parameter along the center line of the sphere for the ED resonance ($\lambda = 605 \pm 2$ nm for experiments and $\lambda = 595$ nm for theory). The electron-energy dependency of the other Mie resonances is shown in Figure 3.10. The main trend of the measurements follows the calculated data: the excitation efficiency shows a minimum value which is strongly dependent on the electron energy. This clearly underlines the phase-matching condition for the ED: the minimal coupling strength is expected at $q \sim 4\pi/D^*$, with D^* the height of the particle at a certain impact parameter, which is visualized by the white dashed lines in Figure 3.4a,b. These electron-energy dependent CL measurements allow us to determine the thickness of the nanosphere at different impact parameters using the well-defined phase-matching condition of the ED resonance. Furthermore, for excitation at the edge of the nanosphere, the model predicts a decrease in CL intensity with decreasing electron energy; this is also found in the experimental CL maps, where the intensity at the edge vanishes at the lowest experimentally feasible energy of 15 keV. This originates from the lower CL excitation probability of both

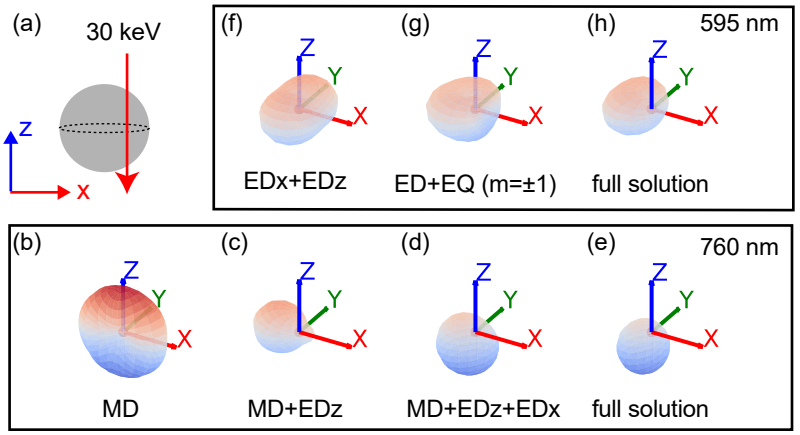

Figure 3.5: (a) Schematic of excitation configuration: a Si nanosphere with r = 96 nm is excited by a 30 keV e-beam at b = 86 nm. (b-h) Far-field radiation patterns at two emission wavelengths: (b-e) λ = 760 nm (MD and ED resonances) and (f-h) λ = 595 nm (ED and EQ resonances). The radiation patterns are calculated by taking the Poynting vector (**S**) of the scattered electromagnetic field of Eq. 3.3, coherently summing over the modes. For the full solution, the sum of all modes using l_{max} = 2 is considered. The color map visualizes the z-direction of the radiation (S_z): red for upward and blue for downward intensities.

the in-plane (x- and y-oriented) and the out-of-plane ED modes (z-oriented) near the edge of the particle (cf. blue line in Figure 3.1c).

3.3.3. Directional far-field emission

With the detailed understanding of selective mode coupling obtained in the previous section, we now study the angular distribution of the CL emission from an individual Si nanosphere and explore how it can be controlled by electron energy and positioning of the e-beam. This gives the possibility to control their interference in the far field, thereby creating directionality of CL emission. First, we theoretically study the angular emission profile for a Si nanosphere (r = 96 nm) excited by a 30 keV e-beam, as depicted schematically in Figure 3.5a. We choose an impact parameter of b = 86 nm as we know that close to the edge, the electron can couple to both magnetic and electric modes at this electron energy. The calculated CL spectrum corresponds to the one shown in Figure 3.2, decomposed into the different modes. To achieve directionality, we exploit the Kerker effect known for dielectric spheres. We study the angular emission distribution at two emission wavelengths where the interference of the modes creates directional emission: (1) λ = 760 nm, using the interference between the ED and the MD mode (Figure 3.5b-e), and (2) λ = 595 nm, using the ED and the EQ mode (Figure 3.5f-h). The data are derived by calculating the Poynting vector for the coherent sum in the far field of the indicated modes. The full modal solution is obtained by summing all relevant modes with $l_{max} = 2$.

In Figure 3.5b we recognize the typical radiation pattern for an MD mode with dipole moment along the y direction (MD_y). We note that the e-beam does not couple to the MD_x and MD_z modes because their electric field vectors are perpendicular to the e-beam trajectory[119]. When adding the contribution of the ED_z mode (Figure 3.5c), we observe directional CL emission opposite to the electron trajectory. This corresponds to the transverse Kerker effect that has been theoretically studied[123] and experimentally observed[124]. When we add the ED_x mode as displayed in Figure 3.5d, the combined effect with the MD gives a Kerker-type interference along the z-axis, creating downward directionality. In the full solution (Figure 3.5e), adding up all modes with $l_{max} = 2$, we observe both horizontal and vertical directionality: the CL radiation is directed towards negative x and negative z. This is the result of the interference of the MD + ED_z mode and of the MD + ED_x mode, respectively. We note that the vertical directionality is downward at wavelengths above the MD resonance wavelength (λ_{MD} = 726 nm) because the ED and MD resonance are in phase[124].

In Figure 3.5f-h, we follow the same steps for the ED resonance at λ = 595 nm. We start by only considering the contributions of the ED modes, namely ED_z and ED_x, resulting in a symmetric emission distribution around the y-axis (Figure 3.5f). Next, in Figure 3.5g the contribution of the EQ is added, which leads to directionality towards the opposite side of the e-beam impact position. This is due to the interference of the EQ and the ED modes. Comparing this to the full solution shown in Figure 3.5h, we see that this interference is the largest contribution to the full solution.

This theoretical study shows that controlling the interference of coherently excited Si Mie modes creates strong directional CL emission in the far field, both in the horizontal and vertical direction. For emission at λ = 760 nm there are two dominant mechanisms: interference of the MD mode with the out-of-plane ED mode (ED_z) resulting in horizontal directionality, and interference of the MD mode and the in-plane ED mode (ED_x) resulting in vertical directionality. At λ = 595 nm, the coherent addition of the EQ mode is necessary to generate horizontal directionality, due to the absence of the MD mode.

3.3.4. Angle-resolved CL

With this theoretical framework for directionality, we now experimentally exploit this formalism for the selective excitation of resonant modes, thereby controlling their interference and tailoring the angular emission distribution. In these experiments, in which we use a slightly smaller nanosphere (r = 85 nm), we vary both the electron energy and the impact parameter. Figure 3.6a shows the CL excitation probability as a function of electron energy at impact parameter b = 42 nm calculated for specific modes using Eq. 3.2. We consider the CL emission at λ = 585 nm, in between the ED and the MD resonance wavelength. We find a strong dependence of the CL excitation probability for specific modes on the electron energy.

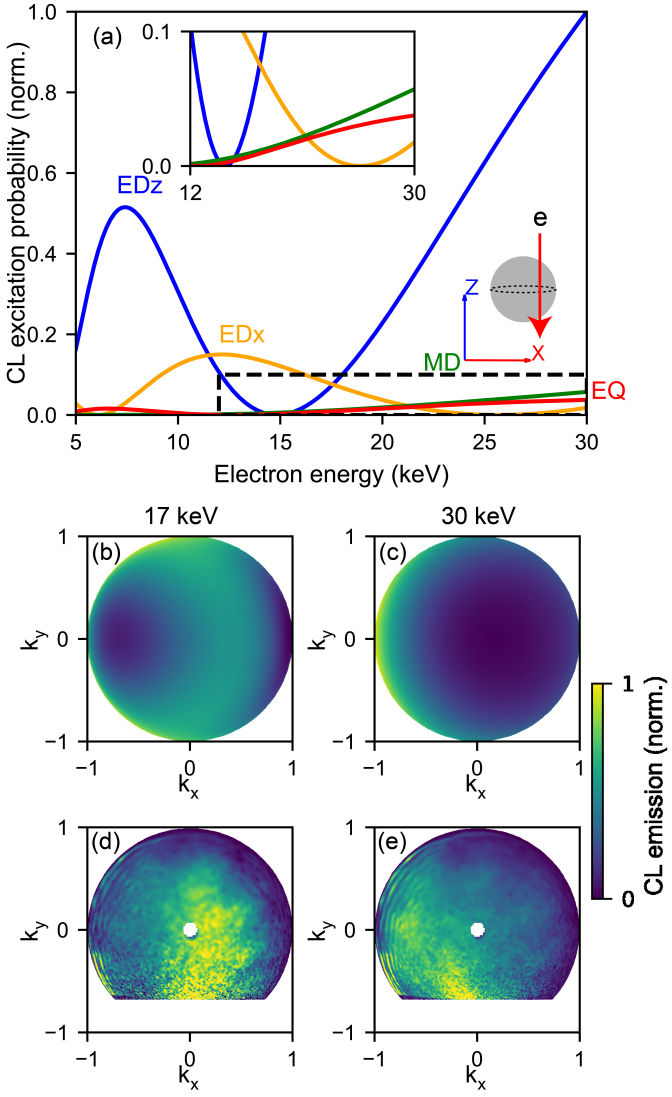

Figure 3.6: Analysis of directional CL emission towards the upper hemisphere from a Si nanosphere with $r = 85$ nm excited with an e-beam with energy ranging from 5 to 30 keV with $b = 42$ nm. (a) CL excitation probability between electron and ED_z (blue), ED_x (orange), MD (green), and EQ (red) modes versus electron energy, with the low CL intensity modes shown in the inset. (b,c) Calculated and (d,e) measured far-field radiation intensities in the positive z-direction (where the electron comes from), excited with a (b,d) 17 keV and (c,e) 30 keV e-beam. The experimental data are obtained with a $\lambda = (600 \pm 25)$ nm bandpass filter, and the theoretical data are calculated at $\lambda = 585$ nm

.

For example, at 15 keV the electron does not couple to the ED_z mode but excites only the ED_x mode, while at 30 keV the contribution of the ED_z mode is strongest. Using these CL excitation probabilities, we calculate the angle-resolved CL emission profile at two e-beam energies. At 30 keV (Figure 3.6c) the theory predicts a strong horizontal directionality towards the opposite side of the excitation (the negative x-direction), originating from Kerker-like interferences of ED_z + MD and ED_z + EQ modes. This strong directionality reverses to the opposite direction, and decreases in strength, for excitation with a 17 keV e-beam (Figure 3.6b). This comparison shows the strong effect of far-field interference of the coherently excited Mie modes in Si nanospheres on the angular radiation profile.

To experimentally study the far-field radiation profiles, we perform angle-resolved CL (AR-CL) measurements at $\lambda = (600 \pm 25)$ nm for electron energies of 17 and 30 keV (Figure 3.6d,e. The data show clear right and left beaming for the two energies, respectively. This is in good agreement with the calculated radiation patterns in Figure 3.6b,c. At 17 keV the interference of the ED_z and ED_x modes in the far field creates strong directionality towards the impact position, while at 30 keV we see a stronger contribution of the ED_z mode superimposed on contributions of MD and EQ modes that make the radiation pattern asymmetric. Consequently, selective mode coupling can be used to generate and tune CL emission with strong directionality by controlling the e-beam energy.

Another important parameter to tune the directionality of CL emission is the impact parameter b, which we investigate for the same Si nanosphere at a fixed e-beam energy of 30 keV. Figure 3.7a shows the coupling efficiency of the e-beam with the EQ, ED_z, ED_x, and MD modes as a function of impact parameter b. The inset shows a magnified view of the lower-intensity modes. We clearly observe two interaction regimes: close to the nanosphere's center (b = 20 nm) the ED_z mode contributes strongest, while closer to the edge the electron can couple to all modes. For two exemplary impact parameters (b = 42 nm and b = 76 nm) we calculate the AR-CL emission, shown in Figure 3.7b,c, respectively. In both cases we notice a strong directionality towards the negative k_x-direction, i.e., opposite to the e-beam excitation. However, for excitation closer to the edge (b = 76 nm), we also find a contribution of the ED_x mode which radiates into the upper hemisphere, as well as radiation from the ED_z mode in the horizontal (in-plane) direction. Similar trends are also seen in the experiments represented in Figure 3.7d,e, where we find a strong horizontal (in-plane) directionality for b = 42 nm, and an additional radiation component into the upper hemisphere for excitation at b = 76 nm. While experiments and theory generally agree well, we also notice in comparing Figure 3.7c,e that the relative contribution of MD + ED_z (horizontal directionality) and MD + ED_x (vertical directionality) to the overall directionality do not fully match. The experimental data indicate that the contribution of the ED_x mode is stronger than suggested by the calculations. We attribute this deviation to the effect of the substrate: the 15 nm thin Si_3N_4 substrate changes the induced electric field in the nanosphere and thereby changes the relative electron-coupling strength to the ED_z and the ED_x mode. Hence, the angular emission pattern can deviate, as also shown

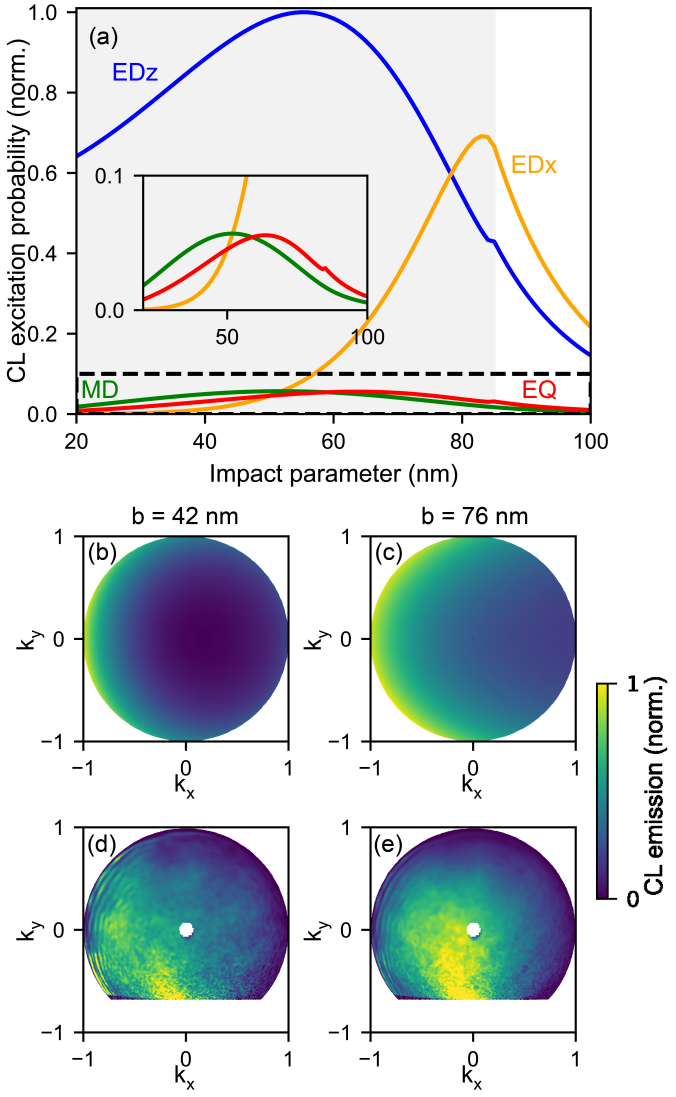

Figure 3.7: Measured and calculated effect of the impact parameter b on the directionality of the CL emission towards the upper hemisphere from a Si nanosphere with r = 85 nm excited with a 30 keV electron. (a) CL excitation probability between electron and ED_z (blue), ED_x (orange), and MD (green) versus b; the grey background shows the inside and the outside of the particle. The inset shows the magnified y-axis for low CL intensity modes. Calculated (b,c) and measured (d,e) far-field radiation intensities in the positive z-direction (where the electron comes from), for excitation at (b,d) $b = 42$ nm, and (c,e) $b = 76$ nm. The experimental data is obtained with a $\lambda = (600 \pm 25)$ nm bandpass filter, and the theoretical calculation is done at $\lambda = 585$ nm.

in Figure 3.7e in comparison to 3.7c.

3.4. Conclusion

In conclusion, we experimentally and theoretically studied the effect of the e-beam energy and impact parameter on the cathodoluminescence (CL) emission of crystalline Si nanospheres. In the experiments, we spectrally identified electric and magnetic dipolar and quadrupolar Mie resonances in the Si nanospheres upon e-beam excitation, in good agreement with theory. Two-dimensional spectral CL excitation maps show the modal excitation profiles at high spatial resolution, limited only by the e-beam spot size and small beam straggle. The spectral and spatial distributions are in good agreement with a model in which the electron resonantly couples to specific modal field distributions with characteristic spatial frequencies that are determined by the electron velocity and resonance wavelength. The accessible electron energies in the SEM offer a wide range of velocities and thus probe a wide span of spatial frequencies, enabling the studies presented here. We use the selective modal excitation mechanism to control the directionality of the CL emission. Both electron energy and impact parameter are used to selectively excite resonant modes that interfere in the far field to create well-defined angular beaming. The insights in this paper can inspire novel designs of lasers, light-emitting diodes, sensors, and photovoltaics, utilizing the coupling of nanosized optical emitters to resonant nanostructures. The resonant nanostructures can function as effective antennas by directing light generated at the nanoscale to the far field. With the resonant electron-mode coupling mechanism solidly confirmed in these experiments, it becomes possible to design this coupling for a wide range of electron-light-matter interactions, in further advanced CL spectroscopy, EELS, and PINEM.

3.5. Appendix

3.5.1. Analytical models

In our initial electron-to-mode coupling model, the CL emission is taken proportional to the energy lost by the electron as it passes through the electric field of a specific single mode. The CL emission is given by Eq. 3.1. This method, valid in the non-recoil approximation and when considering the modes individually, enables the study of electron coupling to single modes. We calculate the induced electric field for a single mode using Mie theory. By using vector spherical harmonics, we calculate the induced electric fields for different modes, excited by a plane wave[117]. While this model presents an intuitive way to determine the coupling to different modes, it does not consider how these modes couple with each other.

For the full solution, we use a Mie-based solution of the CL emission probability[119]. It enables us to consider multiple modes at the same time, which is crucial for the spectral and directionality study. The model gives the expansion of the electric (**E**) and magnetic (**H**) fields induced by an electron crossing a sphere in vector spherical

harmonics:

$$\mathbf{E}^{\mathrm{II}}(r,\omega)=\sum_{l=1}^{\infty}\sum_{m=-l}^{+l}\left\{b_{lm}^{\mathrm{II}}h_l^+(k_0r)X_{lm}(\theta,\phi)+\frac{i}{k_0}a_{lm}^{\mathrm{II}}\nabla\times h_l^+(k_0r)X_{lm}(\theta,\phi)\right\}, \tag{3.3}$$

$$\mathbf{H}^{\mathrm{II}}(r,\omega)=\frac{1}{Z_0}\sum_{l=1}^{\infty}\sum_{m=-l}^{+l}\left\{a_{lm}^{\mathrm{II}}h_l^+(k_0r)X_{lm}(\theta,\phi)-\frac{i}{k_0}b_{lm}^{\mathrm{II}}\nabla\times h_l^+(k_0r)X_{lm}(\theta,\phi)\right\}, \tag{3.4}$$

Here b_{lm}^{II} and a_{lm}^{II} are the expansion coefficients of the scattered field for mode $l>0$ and orientation $(-l\leq m\leq l)$ with the analytic formulas from Ref.[119], X_{lm} are the vector spherical harmonics, and h_l^+ the spherical Hankel function of the first kind.

The CL emission radiated at a point $\mathbf{r}=(R,\theta,\phi)$ in spherical coordinates is proportional to the Poynting vector:

$$\Gamma_{\mathrm{CL}}(\omega,\mathbf{r})\propto\frac{R^2}{\pi\hbar\omega}\mathrm{Re}\left\{\mathbf{E}^{\mathrm{II}}(\mathbf{r},\omega)\times\mathbf{H}^{\mathrm{II}*}(\mathbf{r},\omega)\right\}\cdot\hat{r}, \tag{3.5}$$

and the total CL spectrum after integration over the top hemisphere is given by

$$\Gamma_{\mathrm{CL}}(\omega)=\frac{1}{\pi\hbar\omega Z_0k_0^2}\sum_{l=1}^{\infty}\sum_{m=-l}^{+l}\left(|b_{lm}^{\mathrm{II}}|^2+|a_{lm}^{\mathrm{II}}|^2\right), \tag{3.6}$$

with Z_0 the impedance in free space ($\sqrt{\mu_0/\epsilon_0}$). By selecting the modes of interest (l,m), either magnetic or electric in Eq. 3.3, 3.4 and 3.6, we isolate the contribution of each multipole to the CL radiation.

3.5.2. Monte-Carlo simulations

The electron energies used in this chapter are from 15 to 30 keV, and we find good correspondence between the calculated and measured CL maps (as shown in Figure 3.3 and 3.4). If we use less energetic electrons, below 15 keV, the inelastic scattering of the e-beam will start playing a role. Figure 3.8 shows the Monte-Carlo[99] simulations of (a) a 15 keV and (b) a 30 keV e-beam traversing a 200 nm Si slab, with the edge of a 100 nm radius Si particle shown as reference. We clearly observe the increase in inelastic scattering for low-energy electrons, resulting in a mismatch between simulations and calculations. Therefore, we only use electrons with a higher energy than 15 keV in this chapter.

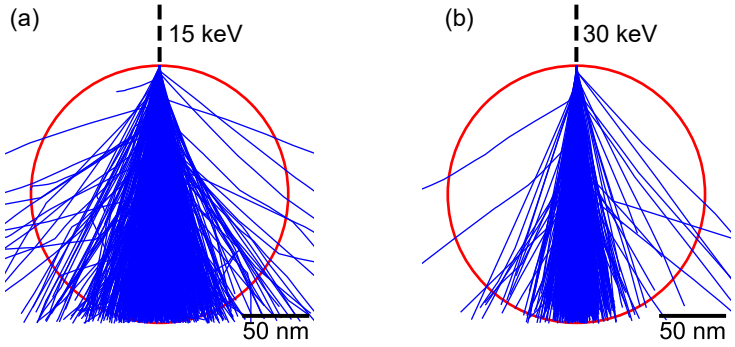

Figure 3.8: Monte-Carlo statistics of the penetration depth (z_{max}) of (a) 15 keV, and (b) 30 keV electrons penetrating a planar Si surface. The insets show the dispersion of electron trajectories during propagation through the Si. Contours of a Si particle with a radius of 100 nm are shown as a guide to the eye.

3.5.3. CL spectra for on-particle and off-particle excitation

The measured and calculated CL spectra corresponding to section 3.3.2 are shown in Figure 3.9 for (a,c) at center excitation and for (b,d) using an impact parameter of 86 nm. Especially when exciting in the center we see a strong modulation of the spectra with electron energy. This represents the phase-matching condition discussed in this chapter. It is visible in the calculated spectrum for on-center excitation (Figure 3.9c) when we focus on the minimum between the ED and the MD mode, found at 650 nm wavelength for 30 keV. For lower electron energies, this minimum shifts to longer wavelengths, in accordance with the phase-matching condition discussed in this chapter.

3.5.4. Electron-energy dependent CL emission

Figure 3.10 shows the line profiles of the CL emission along the center of the nanosphere. The data are shown for a 15-30 keV e-beam exciting the same Si nanosphere (r =93 nm) as shown in Figures 3.3 and 3.4, with the impact parameter varying from −100 nm to 100 nm. The experimental data (Figure 3.10a) clearly shows the different profiles for specific modes: while the magnetic modes show a high intensity at the edge of the particle (b ~75 nm) independent of electron energy, the electric modes show an electron energy dependent intensity. Especially in the minimum this is very clear: at 30 keV electron energy, the minimum appears in the center of the particle, around b =30 nm, and this minimum moves more towards the edge for slower electrons. This is due to the phase-matching condition. The rule of thumb for an electric dipole mode follows that the maxima of CL emission are found at $q \sim (2n+1)\pi/D$, and the minima at $q \sim 2\pi n/D$. In this case this follows the minima nicely; in Figure 3.10b the rule of thumb for the second order CL minima ($q \sim 4\pi/D$) is overlaid with the line profile in dashed white and it follows the minima perfectly. Effectively, electron-energy dependent CL measurements allow for the determina-

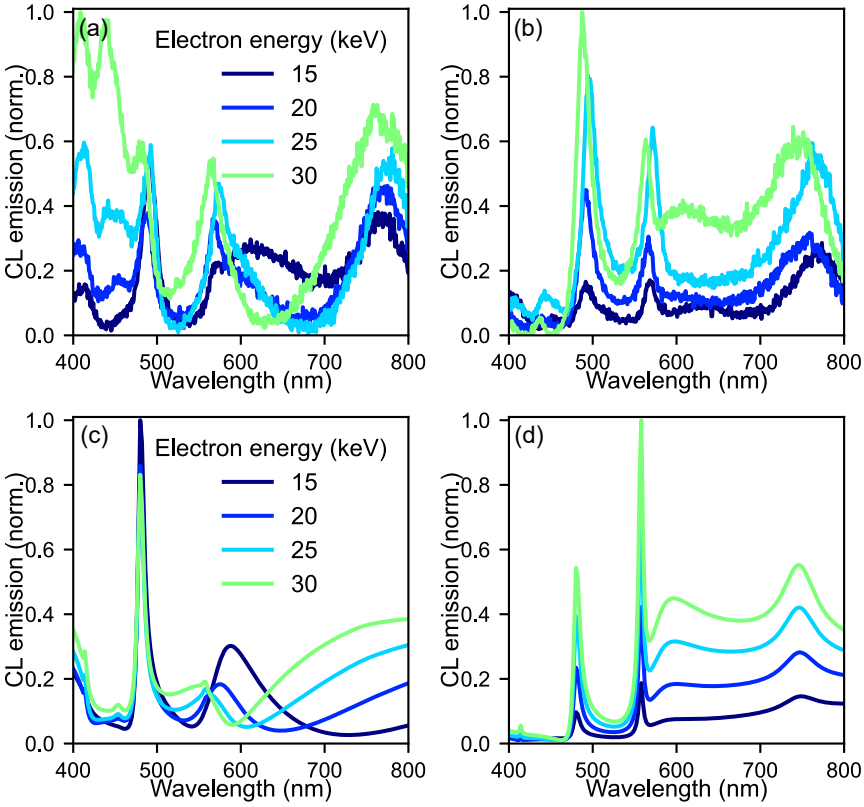

Figure 3.9: (a, b) Measured and (c, d) calculated CL spectra for a Si nanosphere with a radius of 96 nm, excited by a 15, 20, 25, and 30 keV e-beam with (a, c) center-excitation and (b, d) at $b = 86$ nm.

tion of the thickness of the particle at different impact parameters. This is less clear for the MD, MQ, and EQ mode, due to their less distinctive electric near-field distribution: unlike the other modes, the ED has high E_z components at the surface of the nanosphere (as visible in Figure 3.1b).

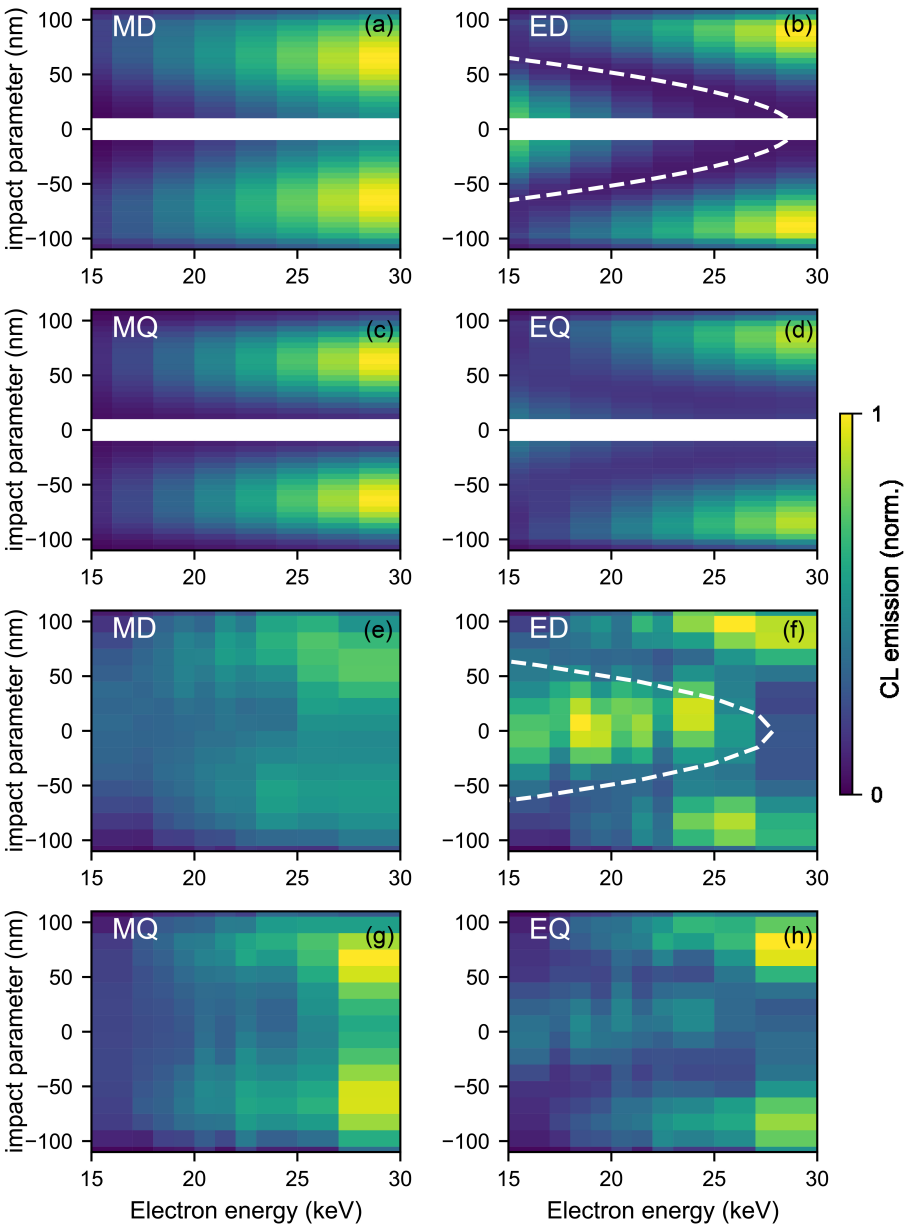

Figure 3.10: (a-d) Calculated and (e-h) measured CL line profiles along the particle's center. The line profiles are shown for a 15-30 keV e-beam exciting the same Si nanosphere (r = 96 nm) as shown in Figures 3.3 and 3.4, with the impact parameter varying from −100 nm to 100 nm. The theoretical CL maps are calculated for wavelengths of (a) 745 nm, (b) 595 nm, (c) 557 nm, and (d) 450 nm. Experimental data are averaged over a spectral bandwidth of 4 nm, with a center wavelength of (e) 744 nm (MD), (f) 605 nm (ED), (g) 563 nm (MQ), and (h) 487 nm (EQ). The white dashed line shows the rule-of-thumb for the expected minima of the phase-matching condition for the ED, $q \sim 2n\pi/D^*$, for $n = 2$ and with D^* the height of the particle at a certain impact parameter (for a spherical particle with radius R, the height at a certain impact parameter is given by $D^* = 2\sqrt{R^2 - b^2}$).

3.5.5. Experimental setup and methods

CL measurements

The measurements were performed in a FEI Helios 600 SEM (ThermoFisher Scientific, Inc.) equipped with a half-parabolic mirror and spectral and angle-resolved CL was acquired using a SPARC system (Delmic B.V.). The CL maps were acquired with a pixel size of 14 nm and an exposure time of 1 s. All spectra and maps were taken from the same nanosphere, and the CL background from the supporting Si_3N_4 membrane was subtracted. The system response was calibrated using transition radiation from a single crystalline Al sample as described in Ref. [107], and this calibration was applied to all experimental CL data.

Directional emission studies were performed on a smaller Si nanosphere of radius 85 nm. For the angle-resolved CL emission measurements, the grating was removed from the optical path, and the reflected light from the mirror was directed onto a 2D CCD camera for Fourier imaging. Bandpass filters of 50 nm bandwidth and 5 s exposure were used. The e-beam current was 1.4 nA in both spectral and angle-resolved CL measurements.

Sample fabrication

The Si nanospheres were fabricated by crushing SiO lumps to powder and annealing in N_2 atmosphere. The powder was etched in hydrofluoric acid (HF) to remove the SiO_2 matrices. The freestanding Si nanospheres were transferred to methanol, ultrasonicated, and filtered to obtain particle sizes around 100 nm radius[120]. We drop-casted 5 μL from the suspension onto a 15 nm thin Si_3N_4 TEM support film (PELCO®) and dried it. Post-processing of the SE images yielded particle radii of 96 nm and 85 nm for spectral and angle-resolved CL analysis, respectively.

4

Cathodoluminescence interferometry

Now that we have established how the electron couples to optical near fields, we extend our study to the sequential excitation of multiple particles. We demonstrate angle-resolved cathodoluminescence (CL) interferometry from electron-beam-excited plasmonic and dielectric nanostructures placed above a Au-coated substrate. We use 20-30 keV electrons to coherently excite plasmon-mediated radiation, which interferes with its mirror image, providing a method to determine the particle-substrate spacing. In an aloof excitation geometry, transition radiation emitted from the Au substrate adds to the interferogram and provides a means to probe the electron traveling time. To study different contributions of the interferogram, we use Fourier transforms and find characteristic peaks corresponding to the time delay of between the interfering sources. The measured CL interferograms are in excellent agreement with a scattering and interferometry model in which a single electron coherently launches plasmons at two separate locations. Polarization-resolved CL measurements confirm the interferometric scattering model. Electron-excited Si Mie scatterers show interferograms modulated with resonantly enhanced emission. To further study the time-characteristics of the interference patterns, we compare three particles with a different resonant behavior. The widths of the peaks in the time domain correspond to the quality factor of the excited resonance, effectively we are probing the decay time of the resonant particle. CL interferometry enables accurate measurement of critical distances in nanoscale geometries, in particular along the electron-beam direction, which are not easily accessible in electron microscopy, while offering a platform for studying optical interference in complex geometries.

4.1. Introduction

Optical interference is a powerful concept that provides key insights in the properties of light by probing the way differences in phase and amplitude of optical waves vary in space and time. Precise measurements of this phenomenon allow for performing high-precision metrology. With the growing importance of optical metamaterials and nanoscale metastructures, the use of optical metrology is becoming increasingly relevant to probe features at the nanoscale[125, 126]. For example, the integration of optical metamaterials can help improve the performance of photovoltaics and photo-catalysts[5, 9, 14], provided their geometries are precisely controlled. Likewise, optical metasurfaces can serve as flat optical components, with their precise functionality determined by precision in manufacturing[127], while plasmonic antennas that control the directionality of emission in lasers and light-emitting diodes must be accurately shaped and positioned to operate efficiently[18]. Developing methods to probe the structure and dimensions of nanoscale objects is therefore of great relevance.

In this context, scanning electron microscopy (SEM) is often used to image two- and three-dimensional structured surfaces. SEM collects secondary electrons created by an electron-beam (e-beam) that is raster-scanned over the surface. Conventional SEM typically provides two-dimensional surface information, but several methods have been developed to extract additional insight into the third dimension. One approach is to vary the sample inclination or use beam tilting in TEM tomography, enabling full 3D reconstruction of nanostructures[128]. This method can yield complete tomographic information but is limited to samples that are thin enough for electron transmission, which often require specialized preparation. Another approach, exemplified by photometric methods, analyzes variations in surface contrast detected at multiple positions relative to the sample[129]. Although this technique can measure surface gradients with high precision, it cannot resolve structures along the electron beam direction, making it unsuitable for stacked layers or situations where the absolute depth along the beam path is required. Furthermore, deriving precise length information is challenging in SEM, as charging and local beam deflection affect the recorded images. Finally, the use of optical methods using, for example, laser excitation to probe nanoscale features in structural metasurfaces is limited by diffraction affecting the light intensity distribution at the surface.

Here, we introduce cathodoluminescence (CL) interferometry as a method to determine the distance between nanophotonic objects and a substrate using e-beam excitation and collection of the angle-resolved emitted CL radiation. Previously, the coherent excitation of surface plasmon polaritons on a Au surface has been demonstrated[130] and polarized light emission has been achieved using a bullseye structure[131], while a spirally structured surface creates optical vortex beams[132]. Additionally, electron-excited plasmonic Yagi-Uda nanoparticle antenna arrays showed directional emission due to interference of different modes[107], and CL holography was demonstrated to measure the phase of plasmon scattering by in-

terference between transition radiation (TR) and radiation emitted from a single plasmonic scatterer[78]. In all these scenarios, a single point of electron impact led to the excitation of multiple radiation sources, which then interfere in the far field. CL interference between multiple points of impact has been demonstrated in Smith-Purcell radiation[133, 134] and interference was also observed between the radiation from electron-excited surface-plasmon polaritons and exciton polaritons in thin layers of WSe_2 and h-BN[135, 136].

In this work, we study the interference of plasmonic scatterers that are separately excited by a single electron at different moments in time. We collect the angle- and wavelength-resolved CL in the far field[73, 107]. Our experiments take advantage of the fact that the e-beam provides a controlled and highly localized source of optical excitation to measure an area of interest. Far-field interference of radiation originating from plasmon excitation provides a powerful means to determine spatial distances with nanoscale precision because the difference between the excitation times translates into a relative phase in the emission amplitudes as a function of emission frequency and angle. Due to different quality factors of optical resonances, there is a variation in temporal width of the contributions of the interference, which is observed in the measurements. Furthermore, CL interferometry can provide information on the coherence of plasmon radiation generated by high-energy electrons.

4.2. Results

4.2.1. On-tip excitation

Figure 4.1a shows a schematic of our CL interferometry experiments and an SEM image of a free-standing Pt nanopillar fabricated using electron-beam-induced deposition (EBID) from a Pt-organometallic precursor. The nanopillar is grown in an SEM at a 45° tilt angle on a Au-coated Si substrate and the entire sample is coated with another 50 nm of sputtered Au (see section 4.4.9 for the fabrication procedure). The e-beam (spot size ~5 nm) is placed on the top of the nanopillar. We then perform angle- and wavelength-resolved CL spectroscopy in an SEM equipped with a parabolic mirror placed in between the sample and the electron column. The mirror collects the emitted radiation, and, due to the focusing properties of its parabolic shape, angular information is maintained. Using a vertical slit, we select a narrow range of azimuthal angles (parallel to the length of the pillar) and project these onto a spectrometer to simultaneously retrieve spectrally and angularly resolved data.

Figure 4.1b shows the wavelength and angle-resolved intensity measured over a range from $\theta = 10°$ (sideways to the left in Figure 4.1a) to $\theta = 90°$ (corresponding to the surface normal, upward direction). These data are acquired for an e-beam that intersects the pillar at its center, such that it directly excites the tip and does not continue beyond the structure. A clear far-field interference pattern is observed, whose period in the spectral domain strongly depends on the emission angle. We assign these features to the interference of two sources of radiation as represented

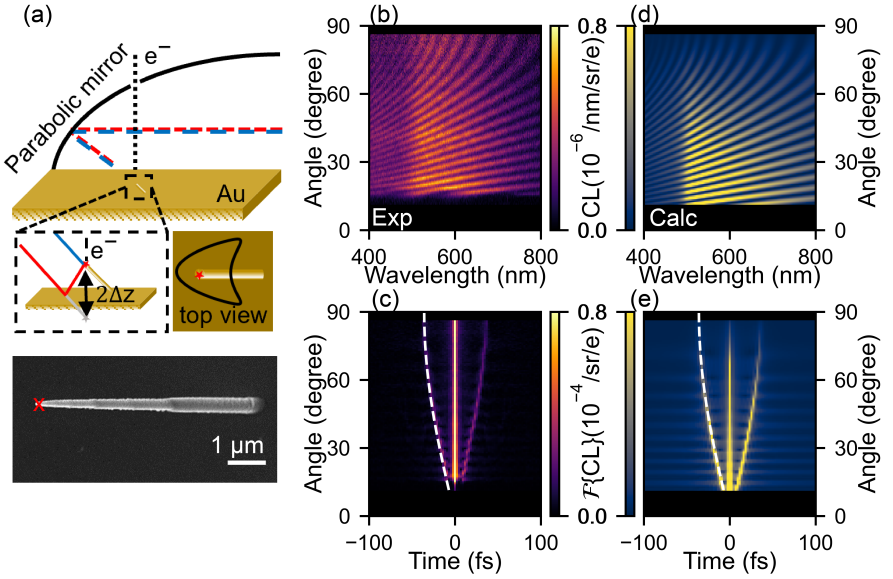

Figure 4.1: Demonstration of CL interferometry. (a) Schematic representation of the experimental setup and a top-view SEM image of the fabricated sample, with a red cross indicating the impact position of the e-beam. 30 keV electrons excite the tip of a Au pillar, producing light emission, which is collected by the parabolic mirror and directed towards the optical detection system. There are two possible light pathways (directly collected tip emission (blue) and collection of its reflection (red)). The pathlength difference depends on the emission angle (θ). (b) Experimentally measured angle- and wavelength-resolved CL intensity. (c) Fourier transform of (b) to the time domain. (d) Calculated angle- and wavelength-resolved CL spectra. (e) Fourier transform of (d) to the time domain. The white dashed lines in (c,e) correspond to the time delay given by eq 4.1 for a pillar with $\Delta z = 5.37$ µm.

in Figure 4.1a: a contribution from the plasmon scatterer directly to the detector (in blue), and another one associated with the plasmon radiation from the same source that is reflected at the metallic surface (in red). The time difference for emission between the two sources is

$$\Delta t(\theta) = \frac{2\Delta z \sin(\theta)}{c}, \tag{4.1}$$

where Δz is the height of the pillar and c the speed of light. For small angles, we observe a long spectral interference period, due to the small pathlength difference between the two radiation sources. In contrast, at 90° (perpendicular to the surface), the pathlength difference reaches a maximum ($\Delta t = 2\Delta z/c$) corresponding to the shortest spectral interference period, all in agreement with the interference model.

To analyze the data, we Fourier-transform the spectra at every emission angle to go to the time domain. To match the experimental data, we fit the pillar height to 5.37 µm (see section 4.4.4). The result is shown in Figure 4.1c, where the time delay calculated from eq 4.1 as a function of angle is overlaid and represents the data very

well. We then use this value to compute the angle- and wavelength-dependent CL emission intensity by summing the calculated individual electric-field distributions in the far field (see section 4.4.1 for the calculation), and the corresponding Fourier transform (see Figures 4.1d,e, respectively). We approximate the tip of the nanopillar as a large Au nanoparticle that supports a localized dipolar surface-plasmon resonance at 600 nm wavelength (see section 4.4.2 for CL spectra of a free-standing nanopillar). In the calculations, we use a Mie-based model[119] to obtain the CL emission from a 150 nm diameter spherical Au particle excited by an electron at 50 nm from the center, using the dielectric function from ref [102].

Comparing the experimental results and the calculations, several interesting features are observed. First, both theory and experiment show a broad resonance in the spectral intensity around a wavelength of 600 nm with a linewidth of ~200 nm, which we attribute to localized dipolar surface plasmons of Au at the tip. Furthermore, in both experiment and calculation, we observe a slight decrease in intensity as the emission angle increases. We assign this to the effect of directional emission from the tip: the electron mostly couples to the z-oriented dipole, which dominantly radiates to lower emission angles.

4.2.2. Off-tip excitation

Next, we study the angle- and wavelength-resolved CL emission in a geometry where the e-beam grazes the pillar at a distance of 5 ± 2.5 nm from the apex's surface, allowing the electron to excite TR as it reaches the Au substrate, after previously exciting the pillar. Figure 4.2a shows the schematic and SEM image of the geometry with the impact position indicated. The measured angular spectra for this configuration and their Fourier transforms are shown in Figure 4.2b,c, respectively. Here, a much more complex interference pattern is observed, especially at low emission angles. This is even clearer in the Fourier-transformed image, where two new interference branches show up at longer times, on either side of the ones found above in Figure 4.1c. The central branches are fitted with a pillar height of 5.34 µm (see section 4.4.5 for the fitting procedure).

We assign the additional interference branches to far-field interference between TR generated at the Au-coated substrate and the two sources that created the interference in Figure 4.1: direct plasmon radiation from the tip and its reflection from the Au-coated substrate. The expected time delay between radiation from the tip and the TR (Δt_+), and between reflected radiation from the tip and TR (Δt_-), is given by

$$\Delta t_{\pm}(\theta) = \frac{\Delta z}{v_e} \pm \frac{\Delta z \sin(\theta)}{c}, \tag{4.2}$$

where the first term on the right-hand side is the time of flight of the electron moving with a velocity v_e (~ $0.33c$ at 30 keV). The expected time delay matches very well the outer branches of the Fourier-transformed data (see the white dashed lines in Figure 4.2c). The time delay derived by extrapolating the outer branches to an angle of 0° is 55 fs, which corresponds to an electron velocity that matches that for 30 keV electrons within 2 %. Finally, there is a small part of the TR emission that scatters

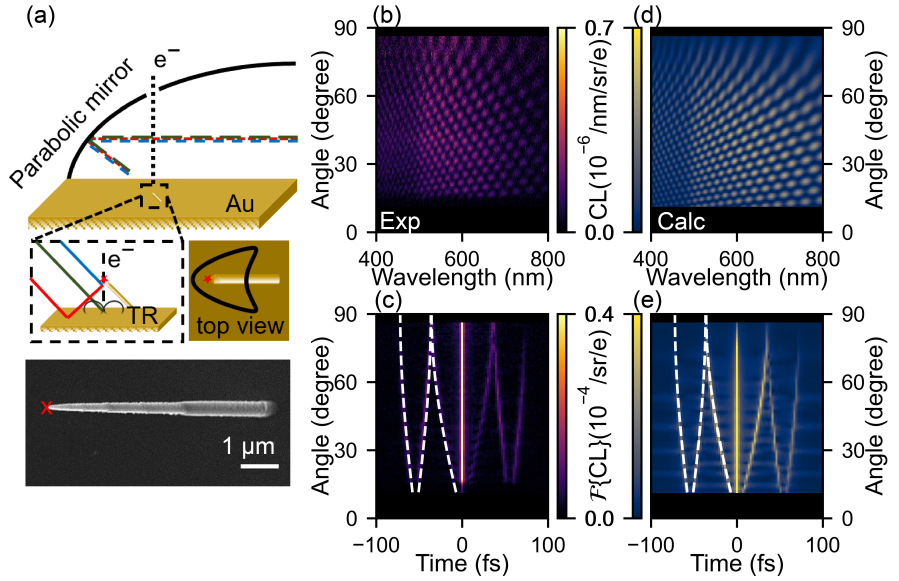

Figure 4.2: Three-way CL emission interference from tip, image, and TR. (a) Schematic representation of the experimental setup for off-tip excitation and an SEM image of the top view of the fabricated sample, with a red cross indicating the impact parameter of the e-beam. The fast electron (30 keV) grazes the tip of the free-standing Au pillar and later excites TR at the Au substrate. This results in CL emission along three possible pathways: light that travels directly from the tip to the mirror (blue), its reflection from the Au planar surface (red), and the TR emitted from the planar surface (green). (b) Experimentally measured angle- and wavelength-resolved CL intensity. (c) Fourier transform of (b) to the time domain. (d) Calculated angle- and wavelength-resolved CL intensity. (e) Fourier transform of (d). The white dashed lines in the outer branches in (c,e) correspond to the time taken by a 30 keV electron to travel from the tip to the substrate for a pillar with a height of 5.34 μm calculated using eq 4.2.

from the shaft of the nanopillar, although this is not significant in these measurements (see section 4.4.3).

We extend the model further and calculate the full interferogram by coherently summing the electric fields emitted from the three sources in the far field. For the TR, we use an analytical result (see section 4.4.1)[85]. In the calculations, we used a pillar height fitted from the inner branches in Figure 4.2c ($\Delta z = 5.34\,\mu$m). The calculated interferogram (Figure 4.2d) mimics the measured data well, with the strongest signal observed around the plasmon resonance. The angular distribution of the CL emission from the plasmonic tip shows a more Lambertian behavior compared to that in Figure 4.1. We assign this to a difference in the relative coupling strength of the electron to the in-plane and out-of-plane electric dipoles. From the previous chapters where we study the electron-coupling to resonant modes, we know that, by exciting close the center of a particle (Figure 4.1), the out-of-plane dipole is dominant, creating an angular emission profile that is maximum at smaller θ, while for electron grazing next to the particle (Figure 4.2), both the in-plane and out-of-plane dipole components are excited[116, 137]. The latter then creates a

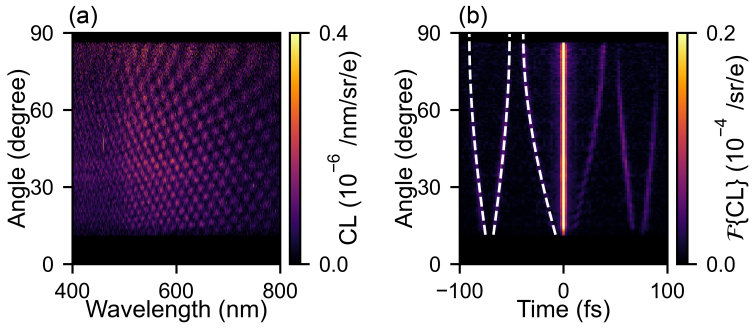

Figure 4.3: The role of electron velocity. (a) Measured angle- and wavelength-resolved CL intensity and (b) its Fourier transform to the time domain for every emission angle. The white dashed lines in (b) correspond to the time delays for the interfering radiation contributions for a 20 keV electron grazing the pillar at a height of 5.81 µm.

more Lambertian-like emission profile. Furthermore, in both experiments and calculations in Figure 4.2, the interference contribution from the TR vanishes at high emission angles, in agreement with the fact that TR has no upward radiation component. The validity of the multiple-interference model is further supported by the strong similarity between the measured and calculated Fourier transforms shown in Figure 4.2c,e, respectively.

4.2.3. Electron-energy dependence

To further evaluate the model, we conduct experiments at an electron energy of 20 keV. The corresponding spectral interferogram and its Fourier transform are shown in Figure 4.3a,b, respectively. The central branches in the Fourier transform are similar to those for 30 keV electrons, as they correspond to the time delay between the direct and reflected components of the tip radiation, which is independent of the electron velocity. By fitting the Fourier data, we determine the height of this pillar to be 5.81 µm. At the same time, Figure 4.3b reveals that the outer branches, which correspond to TR components, show up at a larger time delay compared to Figure 4.2c. The extrapolated time delay at an angle of 0° is 71 fs, which corresponds to the electron velocity at 20 keV ($v_e/c \approx 0.27$) within 0.3 %.

4.2.4. Polarization resolved spectroscopy

The data in figs. 4.1 to 4.3 clearly show the power of CL interferometry to measure characteristic length scales in the sample geometry as well as time delays in scattering events due to the electron traveling time. A so far unexplored degree of freedom is the polarization of the emitted light on the interferograms. As the TR component is p-polarized in the scattering plane defined in Figure 4.1a, it will only interfere with p-polarized emission from the plasmonic tip. To further investigate this effect, we perform polarization-, angle-, and wavelength-resolved CL measurements[138], with the e-beam grazing the pillar at a distance of 5 ± 2.5 nm. Figure 4.4a,b shows

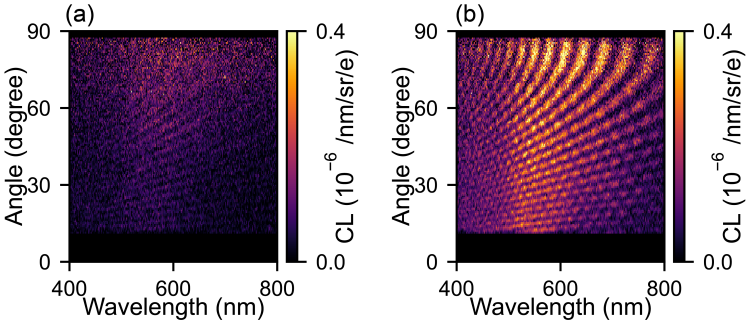

Figure 4.4: Light polarization analysis. Experimentally measured angle- and wavelength-resolved CL intensity for off-tip excitation for (a) s-polarized and (b) p-polarized light emission using 30 keV electrons.

the interferograms taken for s- and p-polarized light, respectively. For s-polarized detection, both contributions (pillar interfering with its mirror image and pillar interference with TR) are strongly reduced compared to the interferogram for p-polarized light emission in Figure 4.4. This is in accordance with the fact that TR emission is fully p-polarized and the tip emission is mostly p-polarized.

4.2.5. Interferometry with Si nanoparticles

To further test and exploit the capabilities of the CL interferometry method, we apply it to scattering from dielectric Mie resonators. We use crystalline Si nanospheres[120] with a diameter of 190 nm, which we place at a controlled distance above a Au-coated Si substrate. Si nanospheres support multiple spectrally narrow Mie resonances with characteristic angular emission patterns. Earlier work has explored the selective coupling between the e-beam and specific Mie modes and how that depends on the impact parameter and electron energy[114]. Selective excitation of Mie modes allows for tuning the angle-resolved CL emission profile by leveraging changes in constructive and destructive interference produced by these modes in the far field.

The sample geometry comprises a 10 µm diameter W wire coated with crystalline Si nanospheres. This structure is deposited on a Au-coated Si substrate. A schematic and an SEM image of the W wire with a number of Si nanospheres attached, is shown in Figure 4.5a. The distance from a Mie sphere at the edge of the W wire and the substrate is expected to be around 5 µm due to the curvature of the W wire, allowing measurements in a geometry similar to that above for plasmonic scatterers.

Figure 4.5 shows angle- and wavelength-resolved CL interferometry data for p-polarized emission for (b) on-particle and (d) off-particle excitation, corresponding to the blue and red dots in the inset of Figure 4.5a, respectively. For both configurations, we observe a clear angle dependence of the interference spectra. For on-particle excitation (Figure 4.5b), we see a similar interferogram as for the plas-

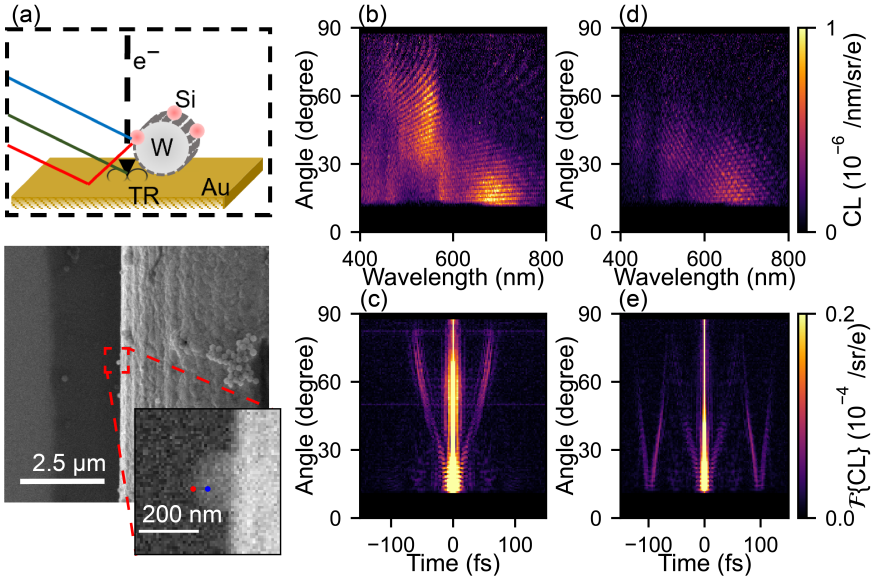

Figure 4.5: CL interferometry for a Si nanosphere. (a) Schematic representation and SEM image of the experimental configuration. An elevated Si particle is excited by the e-beam. For off-particle excitation, the e-beam grazes the Si particle and subsequently excites TR at the Au surface. (b,d) Experimentally measured angle- and wavelength-resolved CL intensity for p-polarized CL emission for (b) on-particle excitation (corresponding to the blue dot in (a)) and (d) off-particle excitation (red dot in (a)). (c,e) Fourier transform of (b) and (d) to the time domain.

monic tips: slow spectral oscillations at low emission angles and faster oscillations toward higher angles. However, in contrast to the earlier data, the intensity of the interferences is strongly modulated by the strong resonant nature of Mie scattering in the dielectric particles. We observe a strong magnetic dipole component around a wavelength of 700 nm that emits mostly toward low angles and a quadrupolar mode at 500 nm that emits over the entire angular range (except low angles). This matches well with the angular emission trends found in earlier work[114, 137]. For off-particle excitation, we observe an additional interference contribution due to the emission of TR at lower emission angles, as was also observed for the plasmonic nanotip.

To reconstruct the height of this specific nanoparticle, we take the Fourier transform of the angle- and wavelength-resolved spectra. This is shown in Figure 4.5c,e for on-particle and off-particle configurations, respectively. The resulting distance retrieved between the particle and the substrate is 9.18 µm. In the Fourier-transformed data, we observe the same behavior as we found in the examples using a Au nanopillar: if the electron impacts the particle in the center, only the central branches are obtained; in contrast, for off-particle excitation, outer branches are present, indicating that TR is excited and interferes with the emission from the par-

ticle. Yet, there are notable differences compared to the plasmonic nanotip.

First of all, the central branch deviates from the expected sinusoidal behavior, particularly at low emission angles. Instead, it shows a plateau with a nearly constant time delay up to approximately 20°, beyond which the delay begins to increase. This is a result of the parabolic shape of the mirror: at low emission angles, there is a large effect of the particle being out of focus, especially for these large distances; as the particle (and thus also its reflection) is not in the focal position of the mirror anymore, light does not come out in parallel directions, and this creates distortions in the interferogram. This behavior aligns well with the numerical predictions (see section 4.4.6). Therefore, we use the time delay at high emission angles to reconstruct the height of this particle. At 85°, the time delay of the center branch is 61 fs, which corresponds to a particle height of 9.18 µm. Secondly, the temporal width of the branches is significantly broader: several femtoseconds rather than the ~2 fs width that was previously observed. This broadening reflects the resonant response of the Si nanoparticle, which supports various Mie modes (MD, ED, MQ, EQ). Each resonance has a distinct quality factor, leading to different lifetimes and, thus, temporal broadening in the Fourier domain.

4.2.6. Time characteristics of resonant nanoparticle excitation

To further study how CL interferometry reveals information about the temporal characteristics of resonant CL exitation, we compare three samples with a different resonant optical response; the plasmonic tip with a broad resonance, a Si nanosphere with multiple Mie resonances within the measured spectral range, and a Au nanostars of which a tip supports a resonance at 700 nm with a large quality factor (see section 4.4.7 for the spectrum of the Au nanostar). For all cases, the e-beam is placed onto the material, making sure that there is only a single source of excitation in the system, and we observe only the interference between the direct particle emission and its reflection.

We take the Fourier transform to study the behavior in the time domain and compare the three samples at two emission angles. Figure 4.6 shows the Fourier transform of the experimental data (solid) of (a) the plasmonic tip, (b) the tip of a Au nanostar, and (c) the Si nanosphere. The height of the nanoparticles above the substrate is 5.37 µm, 6.6 µm, and 9.18 µm, for the plasmonic tip, the Au nanostar and the Si nanosphere, respectively. Due to the differences in pathlength, the location of the temporal peaks shifts to longer time delays for larger distances. Comparing the widths of the peaks, we see clear differences, with the sharpest peak for the plasmonic tip, and a very broad time distribution for the Si nanosphere.

We fit the spectra to three Lorentzian peaks (dashed), according to eq 4.13. The fitting parameters are shown in Table 4.1. For the plasmonic tip we find a very narrow peak, with a full-width-at-half-maximum (FWHM) of 2.5 fs. This matches with the broad spectral emission from the tip resulting in the fast decay time of a TR-like emission of only a few optical cycles. In contrast, for the Au nanostar, the temporal width is much larger, of 6.5 fs, corresponding to the sharp resonance at 700 nm.

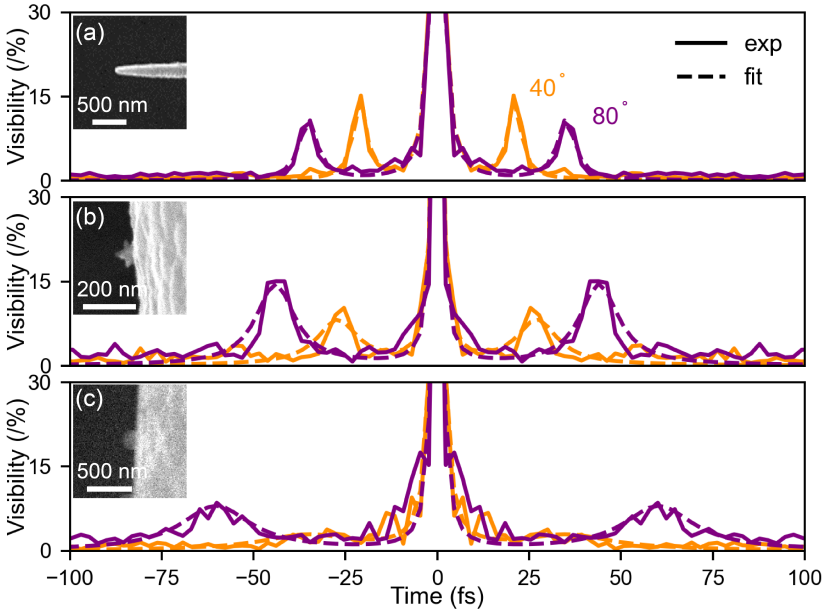

Figure 4.6: Comparison of the temporal width in CL interferograms for several nanostructures. We show the Fourier transform of experimental data (solid) and fitted Lorentzian spectra (dashed) at two CL emission angles, 40° (orange) and 80° (purple). Three samples are compared: (a) plasmonic tip (experimental data from Figure 4.1), (b) Au nanostar, and (c) Si nanosphere (experimental data from Figure 4.5). The SEM images of the particles are shown in the insets.

Finally, for the Si nanosphere, that supports multiple resonances in the spectral domain, we observe even broader peaks. For CL emission at an emission angle of 80° the fitted width is 11.6 fs, indicating the higher quality factor associated with the Mie resonances in the Si particle. The small differences in decay times observed for the two angles, are within the temporal resolution of the measurements. Variation in coupling of near fields to the environment and varying angular distributions for specific modes, could cause a difference in decay time for different emission angles. Interestingly, we discern oscillations within the individual peaks, which we assign to interference of multiple coherently excited resonances (see section 4.4.8 for an analytical description).

4.3. Conclusion

In summary, we have demonstrated angle-resolved CL interferometry from resonant plasmonic scatterers in a geometry where a single electron coherently excites multiple plasmons. Free-standing plasmonic nanotips show interference between the tip emission with their mirror image, and in an excitation geometry where the

Table 4.1: Fitting parameters of the data from Figure 4.6 to multiple Lorentzian peaks.

Fitting Parameter	**Emission angle**	**Au tip**	**Au nanostar**	**Si particle**
Width (γ_i)	40°	2.0 fs	6.7 fs	-
	80°	2.9 fs	6.3 fs	11.6 fs
Visibility (A_i / A_0)	40°	14 %	8 %	-
	80°	11 %	14 %	8 %

electron is not intersected by the tip, TR from the substrate adds to the interference. The interferograms are in excellent correspondence with a coherent interference model that allows for the determination of the distance between the scatterers as well as the electron traveling time (and hence, the velocity). This method can be further expanded to a wider range of geometries. Polarization-resolved CL measurements further corroborate the validity of the interferometric scattering model. Replacing the nanotip by Si Mie scatterers, more complex interferograms are observed, modulated by the resonantly enhanced emission from the particles and resulting in a broadening of the peaks in the Fourier domain. We study the relation between the temporal width in the Fourier domain and the linewidth of the resonance by comparing CL interferometry from three samples with a different optical response; broadband emission from a Au tip, sharp plasmon resonance in the tip of a Au nanostar, and multipolar Mie resonances in a Si nanosphere. The different temporal widths of the peaks in the Fourier domain represent the expected trends in the decay time of the excited resonances. We observe a beating pattern in the temporal distributions due to interference of overlapping resonances.

The CL interferometry presented here opens new applications in the characterization of 3D nanostructures, in particular in the z-direction, normal to the sample's substrate, which is not easily accessible in an SEM. The visibility of the observed interference fringes agrees well with the coherent summation of the radiation intensities from the individually excited sources. This implies that the dephasing of a tip plasmon in the time between its excitation and the generation of TR does not affect the interference, as expected from the nature of free-electron-driven excitations (i.e., they are independent of the electron's temporal extension)[59]. Our experiments also inspire further studies to use the interference technique to separate coherent and incoherent contributions to CL emission, as the visibility of the interference fringes depends on the mutual coherence of the different sources involved. For example, the ratio between coherent and incoherent emission from a substrate (e.g., polaritonic vs inelastic emission) directly impacts the visibility of the interference fringes when the electron passes near a reference similar to the tip or Si sphere used in this work. Future work could extend the present analysis to semiconductor substrates, where incoherent CL becomes comparatively sizable (unlike the Au substrates used in the present study).

4.4. Appendix

4.4.1. Analytical model for far-field interferograms

The total electric field ($\mathbf{E}_{\text{tot}}$) is given by the coherent sum of the field from three sources: TR generated by the electron exciting the Au-coated substrate ($\mathbf{E}_{\text{TR}}$), direct plasmon radiation from the tip ($\mathbf{E}_{\text{tip}}$), and its reflection from the Au-coated substrate ($\mathbf{E}_{\text{tip,r}}$):

$$\mathbf{E}_{\text{tot}}(\mathbf{r},\omega) = \mathbf{E}_{\text{TR}}(\mathbf{r},\omega)e^{i\phi_0} + \mathbf{E}_{\text{tip}}(\mathbf{r}-\mathbf{r'},\omega) + \mathbf{E}_{\text{tip,r}}(\mathbf{r}+\mathbf{r'},\omega), \tag{4.3}$$

where

$$\phi_0 = \frac{2\pi c}{\lambda} TOF, \tag{4.4}$$

is a phase term to take into account the time-of-flight (TOF) of the electron to travel from the tip to the surface (i.e., $TOF = \Delta z / v_e$, corresponding to a distance Δz and a velocity v_e). For the grazing excitation geometry, we model the radiation produced by the plasmonic nanotip as that of a Au nanoparticle with a radius of 75 nm, and both in-plane and out-of-plane electric dipole contributions are obtained using the analytical Mie theory-based model of electron-induced dipole excitation from Stamatopoulou *et al.*[119] for an electron impact parameter of 85 nm measured from the center of the particle. Light reflection at the Au surface is modeled using standard Fresnel reflection coefficients[1]. The electric far field of the TR is calculated for an electron normally impinging a homogeneous planar surface as [85]

$$\mathbf{E}_{\text{TR}}(\mathbf{r},\omega) = i k_0 \cos\theta D \mu_1 \frac{\exp i k_0 r}{r}\hat{\theta}, \tag{4.5}$$

where k_0 is the vacuum wavenumber ($k_0 = 2\pi/\lambda$) and D is given by

$$D = \frac{2ieq_{||}/c}{q_{z1}\epsilon_2 + q_{z2}\epsilon_1}, \tag{4.6}$$

with $\epsilon_{1,2}$ being the relative permittivity and q_{z1} and q_{z2} the perpendicular wave vector components in vacuum and Au, respectively. Here, $q_{||}$ is the in-plane wave vector of light in vacuum, and μ_1 given by

$$\mu_1 = \frac{1}{|v|}\left(\frac{\omega\epsilon_2 + v q_{z2}\epsilon_1}{q^2 - k^2\epsilon_1} - \frac{\omega\epsilon_1 + v q_{z1}\epsilon_2}{q^2 - k^2\epsilon_2}\right). \tag{4.7}$$

The angle- and frequency-dependent CL emission intensity (in units of number of photons per electron per photon-energy bandwidth per srad) is then given by

$$\text{CL}_{\text{tot}}(\theta,\mathbf{r}) = \frac{c}{4\pi^2\hbar\omega}|\mathbf{E}_{tot}|^2 r^2 \sin\theta. \tag{4.8}$$

The calculated CL interferogram and its Fourier transform (from frequency to time) for each emission angle are shown in Figure 4.2e,f. We approximate our plasmonic nanotip as a Au nanosphere with a radius of 75 nm that only supports an electric dipole at the wavelength range under consideration. For the on-tip excitation, we

use an impact parameter of 10 nm, relative to the particle center. For the off-tip excitation, an impact parameter of 85 nm is used. We incorporate optical constants from Olmon *et al.*[102] for Au.

To model the electron-induced radiation spectra from plasmonic and dielectric Mie particles, we use an analytical model from Stamatopoulou *et al.*[119] (also developed independently by Matsukata *et al.*[114]). The electric field at a frequency $\omega = 2\pi c/\lambda$ and position $\mathbf{r} = (r, \theta, \phi)$ is given by

$$\mathbf{E}_{\text{tip}}(\mathbf{r}, \omega) \approx \sum_{m=-1}^{1} \frac{i}{k_0} a_{1m} \nabla \times h_1^{(+)}(k_0 \mathbf{r}) X_{1m}(\theta, \phi), \tag{4.9}$$

for the contribution of components with dipolar, transverse-electric (TE) symmetry. Here, a_{1m} are the corresponding expansion coefficients, which depend on particle radius, electron velocity (v_e), and impact parameter (b). Furthermore, $h_1^+(s) = (1/s - i)e^{is}/s$ is a spherical Hankel function of the first kind, k_0 is the free space wavenumber ($k_0 = 2\pi/\lambda$), and $\mathbf{X}_{1m}(\theta, \phi)$ are the spherical harmonics defined as

$$\mathbf{X}_{1m}(\theta, \phi) = \frac{1}{\sqrt{2}} \mathbf{L} Y_{1m}(\theta, \phi), \tag{4.10}$$

where $Y_{1m}(\theta, \phi)$ are spherical harmonics and $\mathbf{L} = -i\mathbf{r} \times \nabla$ is the angular momentum operator.

4.4.2. CL spectrum of a free-standing nanopillar

To support the interpretation of the CL interferometry measurements presented in the main text, we investigate the CL emission characteristics of the free-standing nanopillar tip. Figure 4.7 shows CL spectra for the free-standing tip of a nanopillar. In particular, Figure 4.7a shows the CL map at a wavelength of 600 nm and a bandwidth of 20 nm, clearly revealing an enhanced emission at the tip. Figure S4.7b shows the CL spectrum at two impact parameters: at the tip (blue) and at the shaft (purple). The enhanced emission from the tip compared to the shaft corroborates the assumption used in the main text that we excite a localized surface plasmon resonance. In theory, we approximate this tip as a nanoparticle with a radius of 75 nm.

4.4.3. Spectral and angular dependence of TR emission next to a nanopillar

As a check that we can assign for all the different interfering contributions in this chapter, we measure TR emitted from 100 nm next to the tip. Figure 4.8 shows the normalized wavelength and angle distribution of TR emission from a Au surface for an electron passing 100 nm away from a nanopillar, indicated by the red dot in Figure 4.8a. In Figure 4.8b, we find the absence of interference, indicating that light scattering from the shaft is not significant.

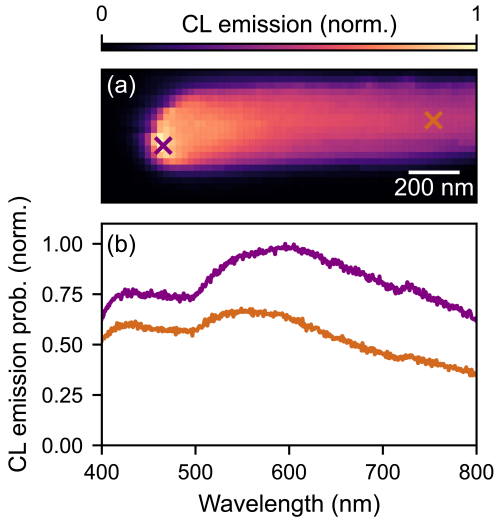

Figure 4.7: CL spectrum of a free-standing nanopillar. (a) CL emission map of the nanopillar at a wavelength of 600 nm with a bandwidth of 20 nm. (b) CL spectra for two impact parameters: at the tip (blue) and at the shaft (purple), corresponding to the crosses in (a).

4.4.4. Fitting procedure for on-pillar excitation

To reconstruct the characteristic dimensions of our geometry, we analyze the interferogram normalized to the spectral response corresponding to Figure 4.9a. We take the discrete inverse Fourier transform according to

$$x_k = \frac{1}{N}\sum_{n=1}^{N} X_n e^{\frac{2i\pi kn}{N}}. \tag{4.11}$$

The Fourier transform in Figure 4.9b shows clear branches corresponding to the emission of the tip interfering with its reflection at the substrate. The angle-dependent time delay of the branch follows the relation

$$\Delta t(\theta) = 2\Delta z \sin\theta / c. \tag{4.12}$$

To recover the height (Δz) from the Fourier transform, we fit the image to three Lorentzian peaks: one at $t = 0$ and the other two at $t = \pm\Delta t$, as given by

$$y(t,\theta) = \frac{A_0(\theta)\gamma_0^2}{\gamma_0^2 + t^2} + \frac{A_1(\theta)\gamma_1^2}{\gamma_1^2 + (t-\Delta t)^2} + \frac{A_1(\theta)\gamma_1^2}{\gamma_1^2 + (t+\Delta t)^2}, \tag{4.13}$$

with γ_0 and γ_1 the temporal widths of the Lorentzian peaks, treated as global parameters, and $A_0(\theta)$ and $A_1(\theta)$ the angle-dependent amplitude of the interference. The resulting fit is shown in Figure 4.9d, producing $\Delta z = 5.370\,\mu$m, $\gamma_0 = 0.7$ fs, and $\gamma_1 = 1.94$ fs.

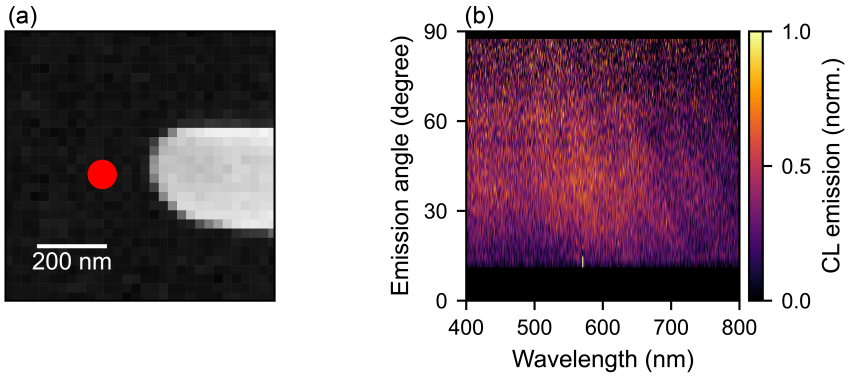

Figure 4.8: Spectral and angular dependence of TR emission excited 100 nm away from the nanopillar. (a) Top-view SEM image of the nanopillar, with the red dot indicating the excitation spot of the electron. (b) Corresponding spectral and angular dependence of CL emission.

The residuals (data minus fitted data) are shown in Figure 4.9c, and we see that the fit is rather accurate, with some characteristic features observed. First, the horizontal red lines correspond to artifacts that occur when the Fourier transform of a finite spectral domain is taken. Furthermore, around the branches, the residuals are a few percent, either positive or negative. This is due to the limited temporal resolution of 2.3 fs. If we examine line traces at specific angles in Figure 4.9e, corresponding to emission angles of 20°, 50°, and 80° in blue, orange, and green, respectively, we observe that the fit nicely captures the data. Finally, from the fitted amplitudes, we can extract the angle-dependent visibility ($v(\theta)$) of the fringes as

$$v(\theta) = \frac{A_1(\theta)}{A_0(\theta)}, \tag{4.14}$$

shown in Figure 4.9f, and we find a visibility of around 15 %.

4.4.5. Fitting procedure for off-pillar excitation

To reconstruct the characteristic dimensions of our geometry, we analyze the interferogram normalized to the spectral response shown in Figure 4.10a. The Fourier transform in Figure 4.10b shows clear branches corresponding to: (1) the emission of the tip interfering with its reflection at the substrate (inner branch), (2) the interference between the reflection of the tip and TR (middle branch), and (3) the interference between the tip and TR (outer branch).

The angle-dependent time delay of the outer branches follows the relation

$$\Delta t_{\pm}(\theta) = \frac{\Delta z}{v_e} \pm \frac{\Delta z \sin(\theta)}{c}, \tag{4.15}$$

with v_e the electron velocity and Δz the vertical separation between the sources.

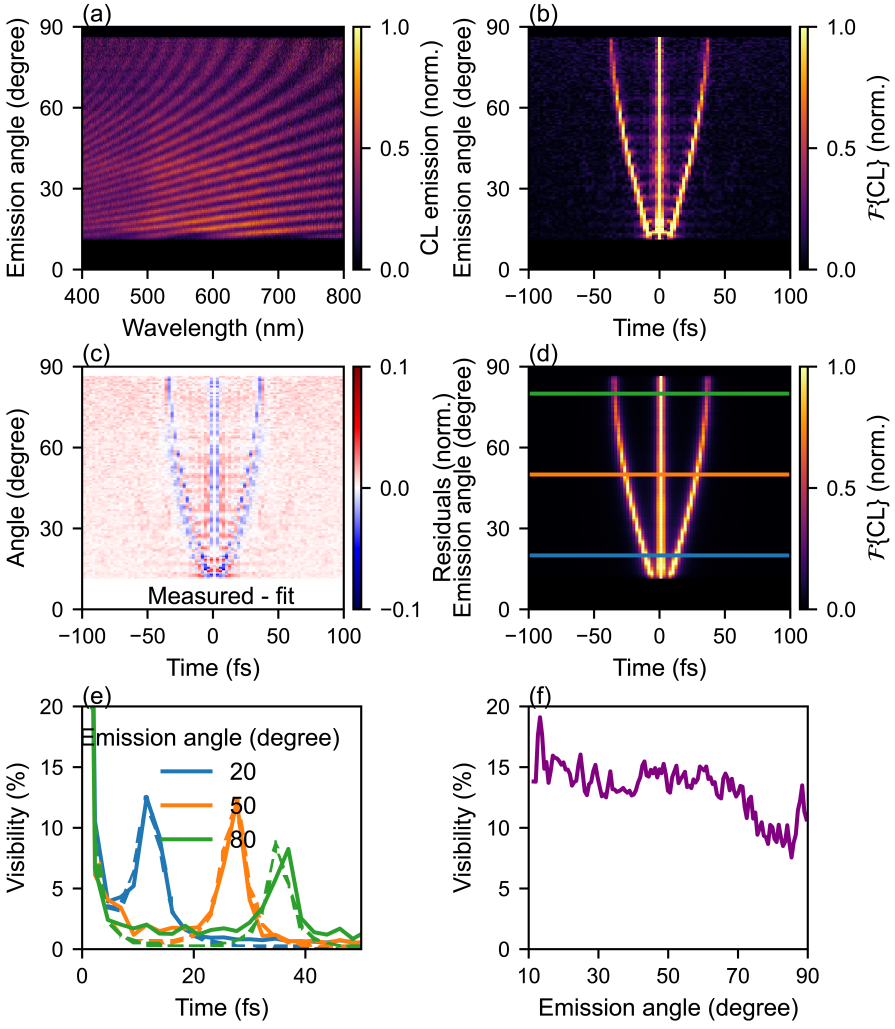

Figure 4.9: Fitting procedure for the on-tip excitation. (a) Spectrally normalized measured interferogram and (b) its Fourier transform, (d) the fit of (b) to three Lorentzian peaks as given by eq 4.13, and (c) the residuals of the data minus the fit. Panel (e) shows line traces of the experimental data (b) and the fit (d) as solid and dashed curves, respectively, for three specific emission angles: 20° (blue), 50° (orange), and 80° (green). Panel (f) shows the angle-dependent visibility of the interference given by eq 4.14.

To recover the height Δz from the Fourier transform, we fit the time-domain response to a sum of seven Lorentzian peaks: one centered at $t = 0$ and three symmetric pairs at time delays $\pm\Delta t$, $\pm\Delta t_+$, and $\pm\Delta t_-$:

$$\begin{aligned} y(t,\theta) = &\frac{A_0(\theta)\gamma_0^2}{\gamma_0^2 + t^2} + \frac{A_1(\theta)\gamma_1^2}{\gamma_1^2 + (t-\Delta t)^2} + \frac{A_1(\theta)\gamma_1^2}{\gamma_1^2 + (t+\Delta t)^2} \\ &+ \frac{A_2(\theta)\gamma_2^2}{\gamma_2^2 + (t-\Delta t_+)^2} + \frac{A_2(\theta)\gamma_2^2}{\gamma_2^2 + (t+\Delta t_+)^2} \\ &+ \frac{A_3(\theta)\gamma_3^2}{\gamma_3^2 + (t-\Delta t_-)^2} + \frac{A_3(\theta)\gamma_3^2}{\gamma_3^2 + (t+\Delta t_-)^2}. \end{aligned} \tag{4.16}$$

Here, γ_0, γ_1, γ_2, and γ_3 represent the temporal widths of the Lorentzian peaks, and $A_0(\theta)$ through $A_3(\theta)$ are the angle-dependent amplitudes.

The resulting fit is shown in Figure 4.10d, from which we retrieve a slightly smaller height than previously reported: $\Delta z = 5.340\,\mu$m. The corresponding fit parameters are summarized in Table 4.2.

Table 4.2: Resulting fit parameters from Figure 4.10d, including the width and visibility of the different interference components contributing to the interferogram in Figure 4.10a.

Fitting Parameter	**Center**	**Tip with Reflection**	**Reflection with TR**	**Tip with TR**
Width (γ_i) [fs]	0.70	1.95	1.48	1.65
Visibility (A_i/A_0)	n/a	10–15%	20–10%	20–5%

The residuals (data minus fit) are shown in Figure 4.10c. Line traces at specific emission angles (20°, 50°, and 80° shown in blue, orange, and green, respectively) are plotted in Figure 4.10e, showing that the fit accurately captures the experimental features. Finally, Figure 4.10f compares the angle-dependent visibility of the different components: the tip with its reflection (purple), the reflection with TR (red), and the tip with TR (pink). At large emission angles (70°), the peaks corresponding to the tip–reflection and reflection–TR paths begin to merge, making them indistinguishable. In contrast, the visibility of the tip–TR interference (pink) clearly decreases from 20% to 0% as the angle increases from 60° to 90°, consistent with the angular emission profile of TR.

4.4.6. Distortions in the interferogram for large spacings

Since we are working with relatively large spacings in this chapter, of the order of a few microns, we have to consider the effect on the light collection by the parabolic mirror. In our calculations, we assume small angles: the mirror is positioned so far away from the sample relative to the height of the pillar ($R >> \Delta z$) that we treat the light rays from the tip and from its reflection as parallel rays and use Eq. 4.12 to derive the time difference at the mirror. However, in practice, the distance between the sample surface and the mirror is of a few millimeters. While this is still large compared to the optical wavelength, for large pillar height, the parallel ray

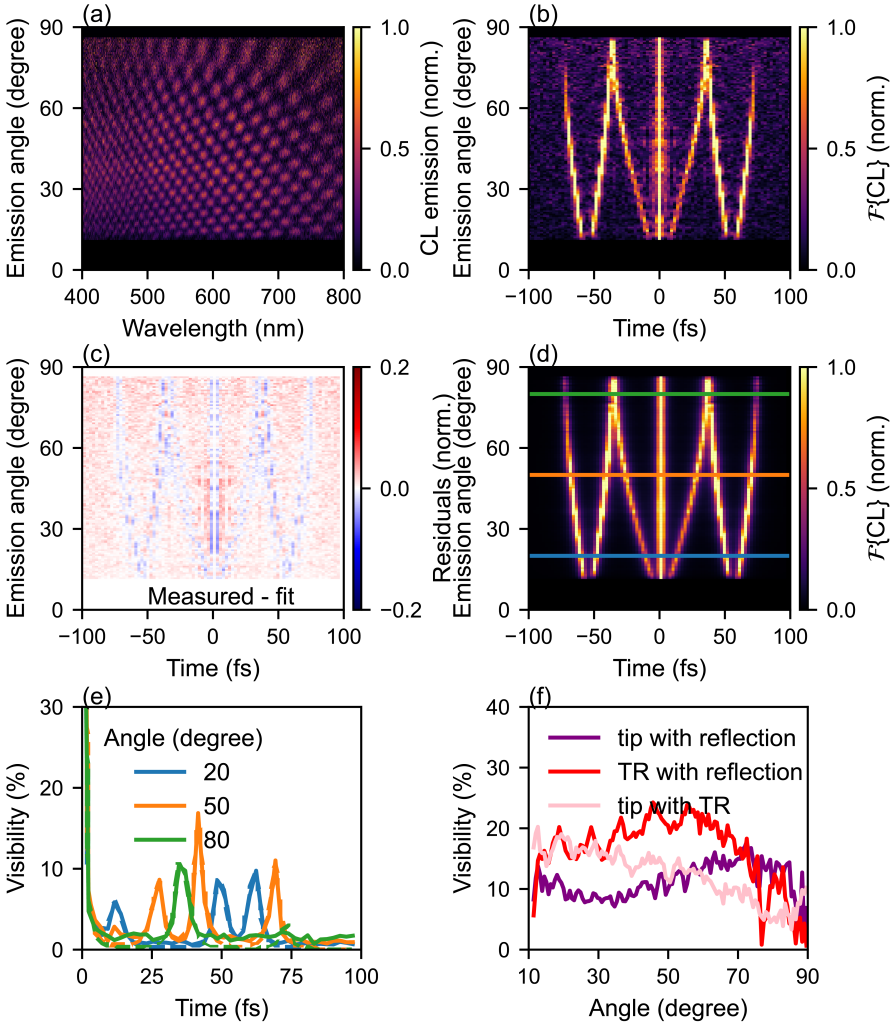

Figure 4.10: Fitting procedure for the off-tip excitation. (a) Spectrally normalized interferogram and (b) its Fourier transform, (d) the fit of (b) to seven Lorentzian peaks as given by eq 4.16, and (c) the residuals of the data minus the fit. Panel (e) shows line traces of the data (b) and the fit (d) as solid and dashed curves, respectively, for three specific emission angles: 20° (blue), 50° (orange), and 80° (green). Panel (f) shows the angle-dependent visibility of the interference for the center peak (purple), the first side peak (red), and the second side peak (pink).

approximation breaks down. This has two main consequences on the measured interferogram. First of all, this slightly modifies the time difference between the sources (e.g., for a 5 µm high tip, this effect amounts to 2×10^{-5} fs at its maximum). Secondly, there is a modification to the emission angle. Although this angular deviation is small (only a few mrad), it propagates through the collection system and leads to a significant error for large spacing. Figure 4.11a shows a schematic representation of this effect, for an exaggerated tip spacing of 0.5 mm: the ray from the surface (black dashed) reflects horizontally, while the ray from the tip (red) is displaced lower on the detector, and the ray from the reflection (green) is displaced higher on the detector. Next, we calculate this difference and estimate the expected error. We use the expression of the parabolic mirror at the azimuthal angle ($\phi = 0$), given by

$$x(z) = az^2 - \frac{1}{4a}, \tag{4.17}$$

with a =0.1 mm^{-1}. A schematic is shown in Figure 4.11a, indicating the emission angle (θ_0), which is given by

$$\theta_0(z) = \tan z/x. \tag{4.18}$$

The angles for the tip emission (θ_+) and the reflection emission (θ_-) are given by

$$\theta_\pm(z) = \tan \frac{z \pm \Delta z}{x} \tag{4.19}$$

Since the incoming angle equals the outgoing angle for a mirror, the deviation on the reflected angle is given by the difference in emission angle,

$$\alpha_\pm(z) = \theta_\pm(z) - \theta_0(z). \tag{4.20}$$

As a result, the displacement on the detector reads

$$d_z = \frac{d_x \tan \alpha_\pm}{A}, \tag{4.21}$$

with d_x the propagation length (40 cm), and A the magnification ($A = 3$). The resulting distortion of the emission angle measured on the detector is shown in Figure 4.11b for pillar heights up to 10 µm. We can clearly observe that this distortion is worse for low emission angles, while for higher emission angles the result is still correct even for pillars of 10 µm in height. Next, in Figure 4.11c,d, we show the resulting interferogram and corresponding Fourier transform (c) without and (d) with the distortion, for a spacing of 10 µm, along with the expected temporal delay, overlaid in white dashed.

4.4.7. CL spectrum of a Au nanostar

The Au nanostars used in this chapter are tuned to have a resonance at the tip of the nanostar centered at 700 nm wavelength. Figure 4.12 shows the CL spectrum of a Au nanostar excited at the tip and we clearly observe resonant emission at a center wavelength of 700 nm, with a FWHM of ~100 nm. The inset shows an SEM of a W wire coated with such a nanostar.

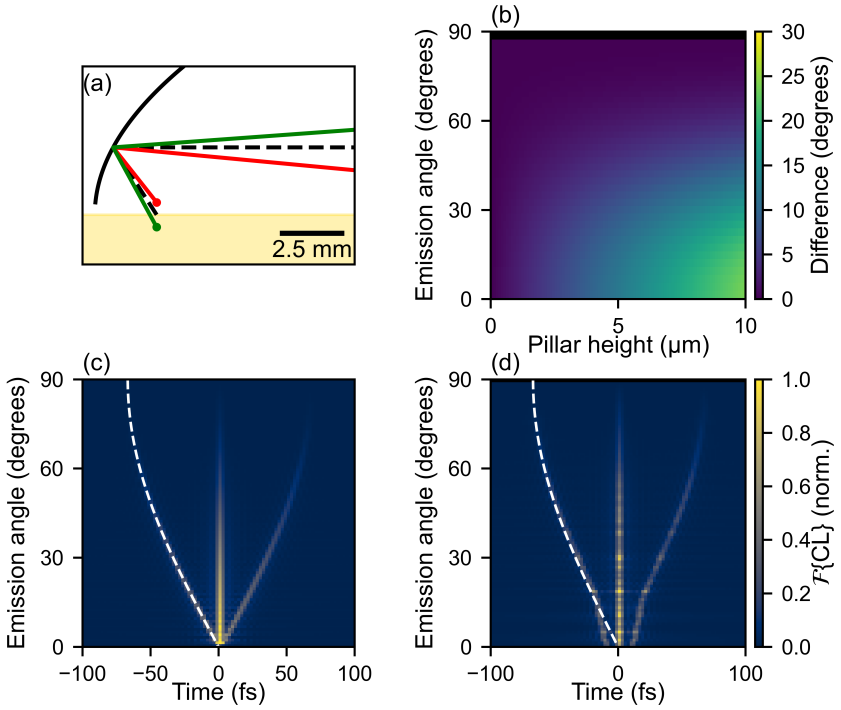

Figure 4.11: Distortion of the interference due to the limited focal area of the parabolic mirror. (a) Exaggerated schematic of the rays from different points reflecting of the mirror, for two points sources at ± 0.5 mm from the focus. (b) Calculated error in the measured angle as a function of scatterer displacement and emission angle. (c,d) Temporal dependence for two scatterers that are vertically spaced by 20 µm, calculated according to the model of Eq. 4.8 (c) without and (d) with the correction on the angular distortion. The white-dashed lines denote the uncorrected time delay expected according to eq 4.12.

4.4.8. Analytical calculation for different scattering spectra

To study the effect of particles with different resonant scattering spectra, the interference is calculated using particles with a Lorentzian scattering spectrum given by

$$A(k) = \frac{\gamma_0}{k - k_0 - i\gamma_0}, \tag{4.22}$$

where γ_0 is the damping rate of the resonance and k_0 is the wavenumber corresponding to the resonance frequency. Figure 4.13a shows the scattering spectra of three test cases: a broadband scatterer (orange), a particle with a Lorentzian resonance centered at 700 nm (green), and a multipolar spectrum with a center wavelength at 500 and 700 nm (blue). In order to study the time-characteristics of these particles, we calculate the interference pattern from the direct CL emission with its reflection from the substrate and take the Fourier transform. Figure 4.13b shows the resulting Fourier transform of the interfering spectra corresponding to (a) at an

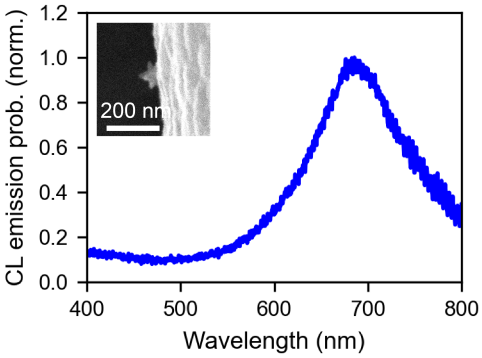

Figure 4.12: CL spectrum of Au nanostar excited at the tip. The inset shows a W wire coated with such a nanostar.

emission angle of 30°.

4.4.9. Experimental setup and methods

Angle- and wavelength-resolved CL measurements

Cathodoluminescence (CL) measurements were conducted in an FEI Quanta FEG 650 scanning electron microscope (SEM; Thermo Fisher Scientific Inc., MA, USA) equipped with a Schottky electron source. To collect the CL emission, the setup includes a parabolic mirror positioned between the sample and the electron column, directing the light into an optical detection system (SPARC Spectral, DELMIC BV, The Netherlands)[73]. Angle- and wavelength-resolved CL measurements were performed by positioning a vertical slit of 100 µm width in the image plane to select CL from a narrow azimuthal angular emission range. The CL is dispersed by a diffraction grating to retrieve spectral information. To measure the polarization-dependent CL emission, a horizontal or vertical polarizer is used to filter p- and s-polarized light, respectively[138]. The measurements were performed with an e-beam current of 1.4 nA and either 30 keV or 20 keV acceleration voltage. For the measurements on the plasmonic tip, an acquisition time of 360 s was chosen for the full angular and spectral interferogram. A line scan with pixels of 10 nm was made to control the position of the e-beam close to the tip. For the dielectric particles, a 2D map was made with pixels of 50 nm and 240 s acquisition time. For all measurements, a dark measurement with the same settings was subtracted and the data was corrected for the system's response. The latter was calibrated using TR emission from a single-crystal Al sample as a reference[139].

Fabrication of the free-standing plasmonic tip

As a substrate, a single-crystalline polished Si (100) substrate was used. First, the substrate was cleaned using base-piranha cleaning and sputter-coated with 2 nm chrome adhesion layer and a 50 nm thick Au film (EM ACE600, Leica, Inc.). Next,

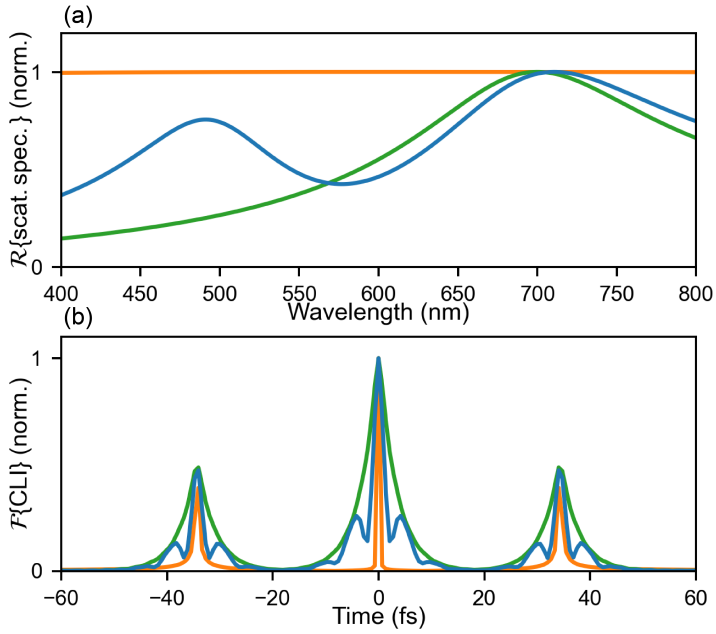

Figure 4.13: Analytical calculation of CL interferometry for different scattering spectra. (a) Real part of the scattering spectra used for the calculation, a broadband scatterer (orange), a broad Lorentzian resonance that peaks at 700 nm wavelength (green), and a multipolar spectrum with a center wavelength at 500 and 700 nm (blue). (b) Fourier transform of the CL interferogram for a particle with scattering spectra from (a) interfering with the reflection of the substrate measured at a collection angle of 30°.

a free-standing Pt nanopillar was grown using e-beam-induced deposition (EBID) in the SEM (FEI Helios NanoLab 600, Thermo-Fisher Scientific, Inc.). EBID was performed with an e-beam of 2 keV energy and a current of 170 pA at a tilt angle of 45° and a dwell time of 1.5 ms. The base of the pillar was 300 nm, decreasing to a diameter of 40 nm at the tip. After the growth, the entire sample was covered with a 50 nm thick layer of Au through sputter-coating. This resulted in a free-standing Au nanotip above a 100 nm thick Au film.

Fabrication of an elevated dielectric sphere

Si nanospheres were fabricated by crushing SiO lumps to a powder. The powder was annealed in N_2 and etched with hydrofluoric acid (HF). The single Si nanospheres were suspended in methanol, ultrasonicated, and filtered to a particle size of around 200 nm diameter[120]. As a substrate, the same fabrication was used as for the free-standing plasmonic tip. The elevated dielectric spheres were fabricated using a 10 µm diameter W wire. First, 1 cm of W wire was cleaned with isopropanol (IPA) and dried using N_2 gas. Next, a wire was deposited in a droplet of a suspension of Si nanoparticles in IPA on a glass substrate. When all IPA was evaporated, the wire

was taken from the substrate and rinsed in IPA. Next, the wire was deposited on the Au-coated Si substrate with a 10 µL droplet of water to ensure that the wire was attached to the surface. This was dried at 60 °C, resulting in elevated Si nanospheres around 5 µm above the Au surface, depending on the location of the nanosphere with respect to the curvature of the wire.

Fabrication of an elevated Au nanostar

The nanostars were prepared through chemical synthesis. First, Au seeds were produced by a modification of the Turkevich method. The Au seeds where added to a polyvenylpyrrolidone (PVP) solution to creat PVP-coated Au seeds, after which they were transferred to an ethanol solution. To grow the nanostars, PVP solution in N,N-dimethylformamide (DMF) containing $HAuCL_4$. When the color turned blue indicates the formation of nanostars. To ensure reduction of all reactants, the solution was stirred overnight. By controlling the amount of reactants, the optical response of the nanostars can be tuned[140]. Next, the dispersed nanostars in ethanol were dropcasted on a 10 µm diameter W wire, and transported onto a Au-coated Si substrate in the same method as the dielectric particles.

5

Studying electron beam coherence using plasmon interference

The interaction between free electrons and optical excitations in nanostructures forms the basis of electron-induced light generation and spectroscopic techniques such as cathodoluminescence (CL), transition radiation (TR), and Smith–Purcell emission. While these methods are commonly interpreted using a classical description of the electron as a point charge, recent developments in the study of the quantum electron-light-matter interactions have revealed conditions under which the electron's quantum mechanical wave packet nature must be taken into account to describe the interaction.

Here, we investigate how the transverse shape of the electron beam (e-beam) affects the CL distribution. Using transition radiation from a thin Si_3N_4 film, we find that the angle-resolved CL emission remains unchanged when the e-beam is broadened from a tightly focused 4-nm spot to a 6-µm diameter beam, indicating that the emission corresponds to an incoherent sum of contributions within the beam spot size. We then use pairs of Au nanopillars to test whether a laterally extended beam can coherently excite multiple scatterers. For closely spaced pillars (200 nm separation), we observe interference in the CL signal and identify coherent excitation from the two emitters. However, when the separation is increased to 400 nm and the e-beam is spread by 500 nm, the interference vanishes, even though both pillars show clear CL. These findings demonstrate, that in this configuration, the coherent excitation of transversely spaced emitters is not observed. Further experiments are required to evaluate if this is due to the limited lateral coherence of the e-beam, or a fundamental aspect of coherent free-electron excitation.

5.1. Introduction

Since the invention of the electron microscope, its applications have revolutionized many different fields. From visualizing the structure of human proteins[141–144] and viruses[145], to optimizing quality control in the semiconductor industry[146, 147], the use of free electrons as a probe has proven versatile. Due to their short de Broglie wavelength electrons provide an extremely small probe size, and decades of technological development have resulted in highly advanced electron optics and many ways to detect and exploit the interaction between electrons and matter. As a result, we can now image periodic crystal lattices and identify defects with atomic precision. Next to the fact that electrons exhibit particle-like interactions, they also exhibit wave properties that can be exploited to gain insight in the structure of matter. In 1937, G. P. Thomson discovered electron diffraction from crystalline lattices[30], establishing the wave nature of electrons. This has emerged as a powerful property and resulted in many technological developments like selected-area electron diffraction (SAED), electron backscatter diffraction (EBSD), and convergent beam electron diffraction (CBED). All these techniques are now widely used to study the lattice structure of material. While the electron microscope has made great strives in material science, traditional imaging only yielded structural information. To obtain insight into to optical material properties, spectroscopic techniques were developed that analyze the energy exchange between electrons and matter, like electron energy-loss spectroscopy (EELS), and cathodoluminescence (CL) spectroscopy. In EELS, the energy loss of the electron is measured, which enables mapping of spectral and spatial distribution of resonant plasmonic modes in metallic nanostructures. CL spectroscopy allows the imaging of photonic crystals, and plasmonic and dielectric nanostructures, to mention a few examples. Furthermore, free-electron induced light can be generated through the Smith-Purcell effect[42] when an electron grazes a periodic structure[43, 44, 134, 148].

More recently, interest is shifting towards treating the electron as a quantum object[45]. In photon-induced near-field electron microscopy (PINEM)[46], an electron can gain or lose quanta of energy due to interaction with a strong optical near field. This interaction shapes the electron energy spectrum into a distribution with multiple sidebands. As a result, it shapes the electron wave packet in space and time as the electron propagates after the interaction. By controlling the temporal overlap between the laser and electron pulse, the complex optical near fields have been reconstructed[57]. The ability to shape the electron wave packet has inspired many theoretical investigations[49, 59, 97]. It paves the way towards entanglement between electrons and photons, proposed in different theoretical geometries[67–70, 149]. Notably, Henke *et al.*[71] and Bogdanov *et al.*[72] experimentally observed the entanglement between a single electron and a single photon, opening the use of electron beams (e-beams) to study the quantum behavior of materials at the nanoscale. One key factor in these experiments is that the electron is described by a wave packet that can be shaped in transverse and longitudinal directions with respect to the e-beam, in contrast to the classical description of the electron as a charged particle, as is typically used in EELS and CL.

In this work, we perform CL experiments aimed at obtaining information about the lateral coherence of the e-beam. We demonstrate that when the e-beam is transversely broadened to interact with multiple scatterers simultaneously, the resulting emission represents an incoherent sum rather than a coherent sum of the scatterers, making the CL emission independent of coherence effect associated with the transverse shape of the e-beam (i.e., it is the incoherent superposition of emission weighted by the lateral density distribution of the e-beam). In a related context, the Smith-Purcell radiation from a metagrating was found to be independent on the transverse broadening of the e-beam[150]. We then investigate how electrons interact with multiple isolated scatterers. First, we study transition radiation (TR) emitted from a thin Si_3N_4 film, excited by a laterally extended e-beam. We investigate individual scatterers, using the excitation of free-standing plasmonic tips by a single electron. Although the e-beam's spatial profile simultaneously covers multiple tips, we do not observe the interference of the CL emission from the two tips. We discuss the data in terms of the limited lateral coherence of the e-beam, and also address the quantum-mechanical concept of which-path information that is either or not erased.

5.2. Results

5.2.1. Transition radiation from a thin film

To study the effect of the transverse shape of the e-beam on CL excitation, we investigate the TR emitted from a thin Si_3N_4 film. TR is a coherent emission process with a characteristic angle-resolved CL emission distribution (Γ_{CL}), given by[85]

$$\Gamma_{CL}(\mathbf{r},\omega) = \left| ik_0 \cos\theta D \mu_1 \frac{e^{ik_0 r}}{r} \right|^2, \tag{5.1}$$

where θ is the azimuthal emission angle, and D depends on the relative permittivity $\epsilon_{1,2}$ and the wave vector components in vacuum (q_{z1}) and Si_3N_4 (q_{z2}) as

$$D = \frac{2ieq_{||}/c}{q_{z1}\epsilon_2 + q_{z2}\epsilon_1}. \tag{5.2}$$

Here, $q_{||}$ is the in-plane wave vector of light in vacuum, and μ_1 is given by

$$\mu_1 = \frac{1}{|v|}\left(\frac{\omega\epsilon_2 + vq_{z2}\epsilon_1}{q^2 - k^2\epsilon_1} - \frac{\omega\epsilon_1 + vq_{z1}\epsilon_2}{q^2 - k^2\epsilon_2}\right). \tag{5.3}$$

To investigate how the transverse coherence of the e-beam affects this emission, we measure the angle-resolved (AR) CL intensity under two conditions: (i) when the e-beam is tightly focused onto the sample, resulting in a spot diameter of approximately 4 nm (see section 5.4.3 for details on the spot size determination), and (ii) when the sample is positioned above the e-beam's focal plane, resulting in a defocused spot of approximately 6-µm diameter. A schematic representation is shown

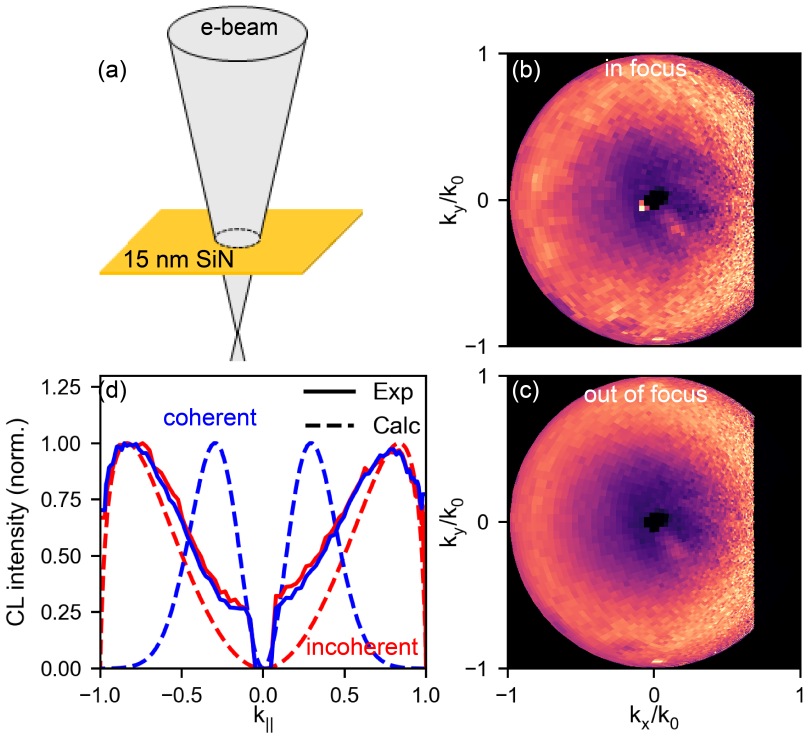

Figure 5.1: Transition radiation from a 15-nm Si_3N_4 thin film excited by 30-keV electrons at a beam current of 1.6 nA. (a) Schematic representation of the experiment when the sample is placed above the focal point of the electron beam. (b,c) AR CL data measured with a 50-nm bandpass filter centered at a wavelength of 500 nm, for (b) the Si_3N_4 film in the focal position, and (c) with a spread e-beam of 6-µm diameter. (d) Calculated (dashed) and experimental (solid) data for TR emitted from a thin film of Si_3N_4. The calculation shows both the characteristic AR CL emission (red), and the coherent sum of sources of TR over the spot of the e-beam using a Gaussian distribution with a FWHM of 500 nm (see section 5.4.2 for the calculation). The experiments show the corresponding angular distribution of TR emission from a focused e-beam (red) and a defocused e-beam (blue). The region with vanishing CL signal around $k_{||} = 0$ corresponds to the hole in the mirror, where no CL is collected to direct to the detector.

in Figure 5.1a. We use a 30-keV e-beam and collect the angle-resolved CL emission through a 50 nm bandpass filter centered at a wavelength of 500 nm. The e-beam current was 1.6 nA, corresponding to an average arrival time between electrons at the sample is 100 ps, much larger than the TR decay time of a few fs. Figure 5.1d shows the normalized angular emission calculated from Eq. 5.1 for the focused beam (red dashed curve) and for the coherent sum of TR emitted over the entire e-beam spot, assuming a Gaussian excitation distribution with a full-width-at-half-

maximum of 500 nm (blue dashed curve). If the TR were coherently excited over the full beam area, the resulting emission would be expected to shift toward the surface normal compared to the characteristic TR angular profile for a point dipole.

The angle-resolved CL results for the focused and defocused beams are shown in Figures 5.1b,c, respectively, plotted as maps of the in-plane wave vectors normalized to the free-space wavenumber ($k_0 = 2\pi/\lambda$), with λ =500 nm. We observe a similar angular emission distribution for both conditions. To better compare the angular emission profiles, Figure 5.1d shows the angular intensity for in-focus (red) and out-of-focus (blue) conditions, integrated over an angular range of 0.05 rad, along $k_x/k_0 = 0$. The similarity between them indicate the incoherent excitation of TR within the e-beam spot size. The remaining discrepancy between the experimental and calculated results is likely due to contributions of scattered light, visible in the k-resolved images (Figure 5.1b,c) as a bright spot near the surface normal that is superimposed on the TR emission.

These results show that in a thin film, we measure the incoherent sum of TR emitted within the e-beam spot size, indicating that the transversal shape of the e-beam does not influence the angular distribution of the emitted CL. One possibility is that the widened e-beam does not have sufficient lateral coherence to result in a angular profile that is different from a TR from a point source. This raises the question what happens if we perform experiments in which we create subsequent excitations by a single electron and space them only slightly in the transversal direction?

5.2.2. Vertically spaced Au pillars

To answer this question, we study a sample where we place two plasmonic nanotips spaced by several 100 nm in the horizontal plane, and a few μm in the vertical direction. We use vertical spacing to build up a phase difference of the CL emission and use a transversely spread e-beam with a diameter of a few 100 nm. This system has been studied in case of one free-standing plasmonic tip in the previous chapter[151], showing that we can coherently excite multiple scatterers that are vertically spaced. The resulting interference pattern can be used as a measure for the height between them. We create the tips by growing either a W or Pt nanowire under a 45° tilt angle using electron beam induced deposition (EBID) in the SEM, and we coat the sample with 50 nm of Au (see section 5.4.4 for the fabrication). Using EBID to fabricate the sample gives us control over the spacing between the wires in the horizontal plane and over the difference in their heights.

We first measure the interference from two nanowires that are placed above each other. Figure 5.2a shows a schematic representation of this geometry, and an SEM image of the fabricated sample taken from the top and at a 15° tilt angle. As the nanowires are placed above each other, we can coherently excite them with a single electron in an aloof geometry, treating the electron as a classical point charge. To study the interference of CL generation by the subsequently excited plasmons, we perform AR spectral CL measurements, where we both measure the angular emission and the spectra simultaneously (see section 5.4.4 for an experimental descrip-

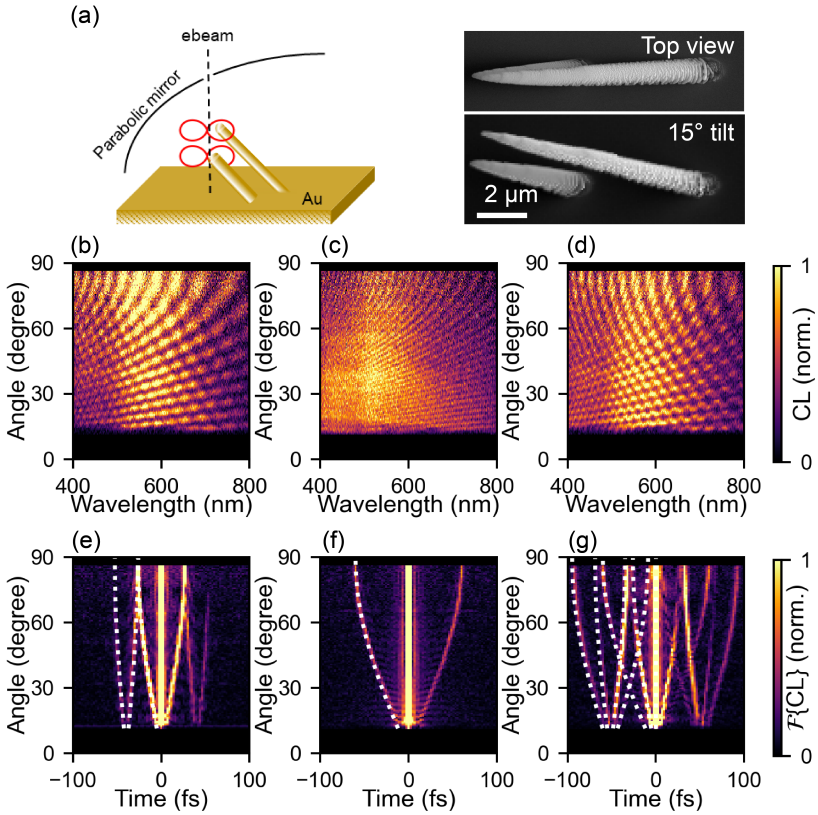

Figure 5.2: Coherent excitation of two Au pillars placed above each other. (a) Schematic representation of the measurement and the SE image of the fabricated sample taken from the top and at a tilt angle of 15°. (b-d) AR spectral CL data from the double pillars and (e-g) their Fourier transformed data in the time domain for three configurations: (b,e) the e-beam grazes the small pillar, (c,f) the electron impinges on the large pillar, and (d,g) the e-beam grazes the tall pillar and impinges on the smaller one. The white dashed lines in (e-g) indicate the calculated time delay components corresponding to a pillar height of 3.9 µm and 9.0 µm for the small and large pillar, respectively.

tion). To analyze the different components that are creating the observed interferences, we take the Fourier transform at every emission angle, to translate the data from the frequency domain to the time domain.

Figure 5.2 shows the experimental data for three configurations: (1) where the e-beam grazes the small pillar, (2) when placed on top of the larger pillar, and (3) for an electron grazing the larger pillar, and impinging on the small pillar. Figures 5.2b,e show the experimental AR spectral data and the Fourier transform for the first scenario where the electron grazes the small pillar. In the spectral data, we clearly observe a cross-interference pattern indicating that we have more than two sources of radiation. Examining the Fourier transform, we identify these components from small to large time delays as (1) the interference between the direct tip-radiation and the signal reflected from the surface, (2) the interference of TR emitted from the Au surface with tip radiation reflected from the substrate, and (3) the interference of TR emission with the direct tip radiation. From this interference pattern, we find a pillar height of 3.9 µm.

Next, Figures 5.2c,f show the AR spectral data and its Fourier transform, respectively, for an electron impinging on the large pillar. Instead of a cross-pattern, we only find a single curved interference pattern, indicating that we only measure the interference of tip radiation and the reflected signal. The Fourier transform further corroborates this conclusion, where we see only one contribution, which we match to a pillar height of 9.0 µm.

Finally, we analyze the configuration of the electron grazing the tall pillar and impinging on the smaller one, shown in Figure 5.2d,g. Here, we observe a richer and more complex interference pattern compared to the previous data, further supported by many additional components in the Fourier transformed data. We identify two components that originate at $t = 0$ for 0° emission angle that correspond to the interferences found before due to the direct and reflected tip radiation from both pillars. In addition, we observe four bands originating at t =51 fs at 0° emission angle. These represent the interference of radiation from the two pillars: the intersection with the x-axis at 51 fs corresponds to the time-of-flight (TOF) of the electron to travel from the large to the small pillar (TOF = $\Delta z / v_e$, with Δz the difference in height between the pillars, and v_e the speed of the electrons). The time delay of the inner band is due to the interference of radiation from the large tip and the small tip (Δt_+) and the interference of their reflecting signals (Δt_-), given by

$$\Delta t_\pm = \mathrm{TOF} \pm \Delta z \sin(\theta)/c. \tag{5.4}$$

The time delay of the outer bands is due to the interference of the tip radiation of one pillar with the reflected signal of the other pillar. Since the distance between the pillar and the mirror image of the other pillar ($\Delta z_{\mathrm{ref}} = z_1 + z_2$) is larger than the distance associated with the inner bands. These bands follow a different relation and the time delay associated with this interference is given by

$$\Delta t_\pm = \mathrm{TOF} \pm \Delta z_{\mathrm{ref}} \sin(\theta)/c. \tag{5.5}$$

From the observation of the interference between radiation from both pillars, we conclude that both pillars are coherently excited. In particular, the fact that we identify a component that includes the TOF of the electron is an indication for their coherent excitation.

Next, we investigate a geometry in which we place the pillars next to each other, but purposely still close enough together that the electric near field of the electron can couple to both when the electron passes in between the pillars. Figure 5.3a shows the schematic representation of this geometry and the SEM image of the resulting sample from a top view. The wires, with different lengths, are grown 200 nm next to each other, resulting in a V-groove where we can precisely place the e-beam in the center to assess if we can couple to both tips simultaneously. We measure the AR spectral CL emission from the tall wire, the short wire, and when the e-beam passes between them, shown in Figures 5.3b, c, and d, respectively. In Figure 5.3b,c we clearly see the curved interference bands from the direct tip radiation and the reflected signal, and by analyzing the Fourier transform of the data shown in Figures 5.3e,f, we identify the height of the pillars to be 4.2 µm and 1.7 µm, respectively. For the e-beam passing between the tips, the data is shown in Figure 5.3d,f. We observe a richer interference pattern and the Fourier transform reveals more temporal contributions. On top of the two symmetric bands originating from t =0 fs, we also see bands that intersect with the time-axis at t =25 fs. This is associated with the TOF of the electrons to pass from the tall pillar to the smaller one. The found TOF corresponds to a difference in height of 2.5 µm, which exactly matches the height difference between the pillars. Due to the small difference in height between the pillars, the bands are overlapping and it is difficult to identify their sources, however, from the presence of the component containing the TOF of the electron, we confirm the coherent excitation of both pillars.

5.2.3. Laterally spaced Au pillars

So far, we have shown that by closely examining the AR spectral CL data, we can identify the heights of different contributions of plasmonic scattering and by observing the presence or absence of the cross products between them can reveal if the pillars are coherently excited. However, as the pillars are very closely spaced in the horizontal plane, we can describe their excitation by the coupling of a single particle-like electron to the pillars' evanescent fields. To investigate a geometry that could reveal coherent excitation using the wave-nature of an electron that is defocussed and has sufficient lateral coherence, we have to place the pillars further apart. To do so, and to reduce the complexity of the interference, we partly remove the Au-coated membrane using focused ion beam milling, eliminating the interference between the direct tip-radiation contribution and their reflected component. As a result, the only interference that we would observe must be originating from the two tips being coherently excited.

Figure 5.4a shows a schematic representation of the sample, where again we grow two nanopillars of different heights, but now spaced 400 nm in the horizontal di-

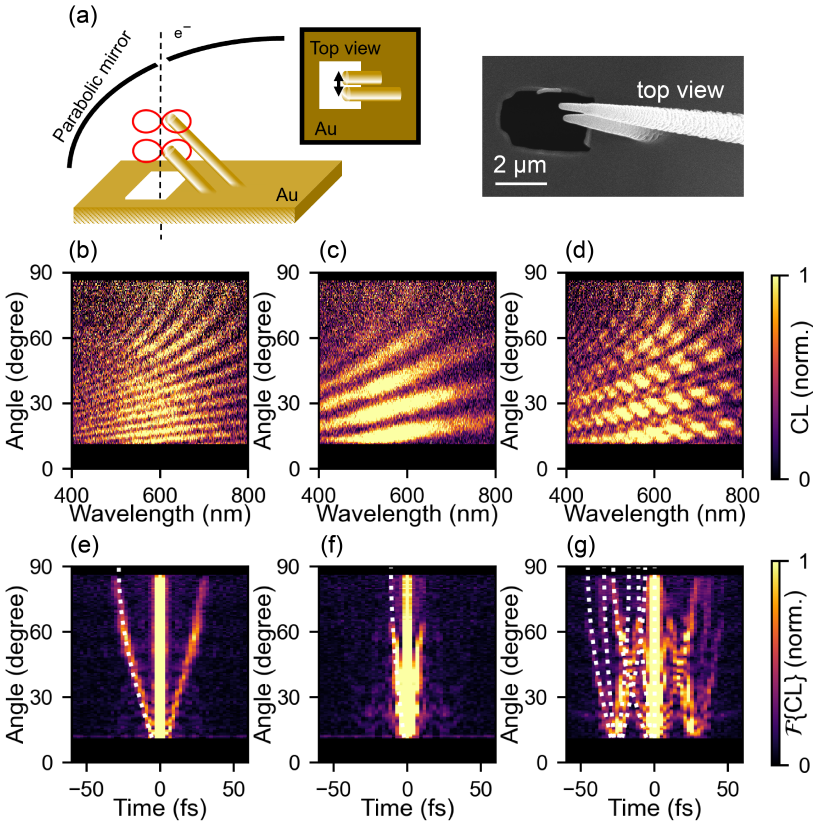

Figure 5.3: Coherent excitation of two Au pillars with different lengths that are displaced on the substrate by 200 nm in the horizontal plane. (a) Schematic representation of the measurement and the top-view SEM of the fabricated sample. (b-d) AR spectral CL data from the double pillars and (e-g) Fourier transformed data in the time domain for three configurations: (b,e) the e-beam grazes the tall pillar, (c,f) the electron grazes the small pillar, and (d,g) the e-beam passes in between the two pillars. The white dashed lines in (e-g) indicate the expected time delay components corresponding to a pillar height of 4.2 µm and 1.7 µm for the large and small pillar, respectively.

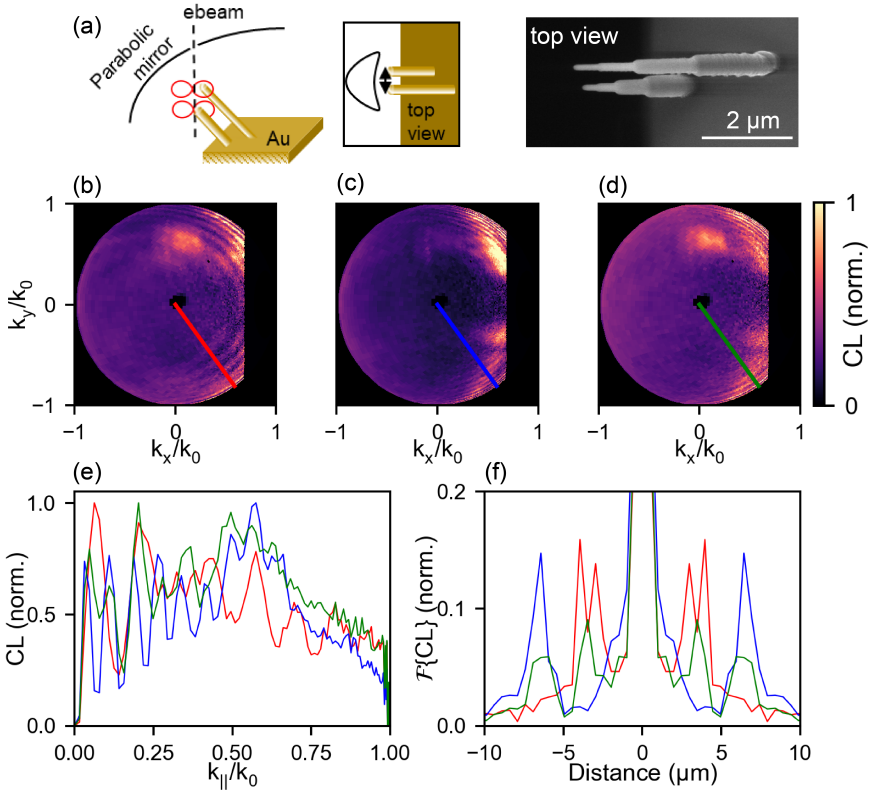

Figure 5.4: Excitation of a double pillar geometry with a laterally spread e-beam. (a) Schematic representation of the measurement and the top-view SEM image of the fabricated sample. (b-d) AR CL data from the double pillar geometry using a 50-nm bandwidth filter centered around a wavelength of 500 nm. (e) Line scans along the k-space images and (f) their Fourier transform, taken from the solid lines in (b-d) for excitation of the small pillar (red), tall pillar (blue), and placed in the middle with a e-beam of 500 nm diameter (green).

rection, as indicated by the top view. The SEM image shows the fabricated sample, where on the left side the substrate is removed using FIB milling. To study the coherent or incoherent nature of the excitation, we perform AR CL measurements using a 50-nm bandwidth filter centered at 500 nm. Figure 5.4b shows the AR CL data for an electron grazing the small pillar. In the AR data we observe interference fringes for positive k_x values, corresponding to the right side of the SEM image in Figure 5.4a. The interferences are again the interference of the direct tip radiation and the reflected signal and therefore are only visible on the right side where the substrate is not removed. To determine the height of the pillar, we take a line scan of the k-space image indicated by the red line. The result is shown in Figure 5.4e (red), where we clearly see the interferences at low emission angles. We take the Fourier transform to translate this spectrum from the reciprocal to the real domain and find that this pillar is 1.7 µm high. Next, we do the same experiment for an electron grazing the tall pillar. The resulting k-space image is shown in Figure 5.4c, and the corresponding line scan and Fourier transform in Figure 5.4e,f, respectively (blue). We identify the height of this pillar as 3.3 µm, resulting in the higher-frequency fringes observed in the AR CL data.

Finally, in order to investigate the possibility to coherently excite both pillars, the electron passes in the middle of the two tips, and we defocus the beam to a spot size of approximately 500 nm, covering both tips simultaneously. The AR CL data is shown in Figure 5.4d, where we clearly see the fringes in the angular range where they were observed in Figures 5.4b,c, indicating that we excite the individual pillars. When we take the Fourier transform of a line scan of this data, shown in Figure 5.4e,f, respectively (green), we clearly see peaks associated to both the tall and the small pillar, indicating that the e-beam excites radiation in both pillars. However, the absence of interference at the negative k_x values, where the substrate is removed, indicates that we measure an incoherent sum of the radiation from both pillars. Hence, we do not coherently excite two horizontally spaced scatterers with a widened e-beam in this configuration.

These results show that, in this configuration and the used e-beam parameters, we do not observe interference associated with the coherent excitation of two laterally separated CL emitters. We can give several considerations. First of all, we have to consider the lateral coherence length of the electrons in the SEM. Coherent excitation of multiple scatterers by different regions of the e-beam requires phase preservation across the illuminated area, i.e., a transverse coherence length comparable to the emitter separation. In transmission electron microscopes (TEMs), Schottky electron sources exhibit a finite degree of spatial coherence (on the order of ≈10 %)[152], and our Schottky emitter in the SEM is of a similar type. In complementary electron diffraction experiments (data not shown), we do observe clear diffraction peaks, indicating a high degree of transverse coherence over a length scale of multiple crystal lattice spacings. However, this is at much smaller length scales than the spacing between pillars studied here. A quantitative study of the lateral coherence length in our SEM remains to be carried out and is a key requirement for observing lateral interference in CL (see Chapter 6).

Secondly, we have to consider the which-path information related to the quantum nature of excitations by coherent electron wave packets; in the present geometry, the electron effectively 'knows' which tip it passed. This information could, in principle, be measured by measuring the position of the electron within the e-beam. Observing interference between spatially separated emitters requires erasing this information. This has been shown in the TEM by Henke *et al.*[71], where the information contained within the photons was erased by mixing polarized signals in order to retrieve the interference on the electron detection plane. In our case, the situation is inverted; we must erase the information carried by the electrons in order to retrieve the interference of the photons. A practical way to achieve this would be to place a structure underneath the double pillar that diffracts the electrons, such as a twisted bilayer of graphene. The diffraction pattern from this structure would consist of partially overlapping diffraction disks. In those overlapping regions, the electron could originate from multiple places within the e-beam. By performing electron-photon correlation measurements and post-selecting photons that are coincident with electrons within one overlapping region, we expect to retrieve the interference pattern, provided the lateral coherence of the e-beam is sufficient. Implementing this scheme requires dedicated sample fabrication and electron–photon correlation capability, both of which are experimentally challenging, but feasible.

5.3. Conclusion

In conclusion, we observe the absence of interference in the CL signal arising from different plasmonic scattering sources within a laterally extended e-beam. For transition radiation (TR) emitted from a thin Si_3N_4 film, the angular emission pattern remains identical whether the film is irradiated with a tightly focused e-beam or with a defocused beam of 6 µm diameter. This demonstrates that, in this configuration, the emitted radiation represents an incoherent sum of TR contributions within the e-beam.

To further probe the spatial coherence of the excitation, we investigated the CL emission from a specially arranged 3D geometry composed of pairs of Au pillars. When the e-beam was positioned between two pillars of different heights separated by 200 nm, we observed clear interference in the CL signal. Analysis of the phase delay between the two emitters reveals a time delay consistent with the electron's time-of-flight between the two pillars, indicating that the electron coherently couples to the electric near fields of both pillars.

In contrast, when the pillar separation was increased to 400 nm and the e-beam was transversely spread to 500 nm, no interference was observed, despite the observation of clear CL emission from each pillar individually. This loss of interference indicates that the laterally extended e-beam does not coherently excite multiple spatially separated scatterers under these conditions. Further experiments will be necessary to determine whether this behavior arises from the limited lateral coherence of the e-beam, or related to fundamental quantum aspects of coherent free-

electron excitation of multiple emitters.

5.4. Appendix

5.4.1. Theoretical description of coherent electron excitation of laterally spaced scatterers

We study the interaction between an electron and a structure that supports an optical excitation of low energy (in the visible regime) compared to the electron energy. Therefore, we can assume that the electron does not change its velocity along the e-beam trajectory (non-recoil approximation). Under these conditions, the effective interaction Hamiltonian $\hat{H}(\mathbf{R})$ only depends on the transverse coordinate $\mathbf{R}$. Since the transverse electron energy transfer is negligible under the non-recoil approximation, the total excitation probability (P) is the incoherent sum over all final states with wave vectors $\mathbf{Q}$ (note that the longitudinal wave vector is determined by energy conservation[85]), given by

$$P \propto \int d^2\mathbf{Q} \left| \int d^2\mathbf{R} e^{-i\mathbf{Q}\cdot\mathbf{R}} \langle n|\hat{H}(\mathbf{R})|0\rangle \psi_{\perp}^{i}(\mathbf{R}) \right|^2. \tag{5.6}$$

Here, $\mathbf{Q}$ is the 2D wave vector of the electron after interaction, and $\psi_{\perp}^{i}$ is the incident transverse wave function of the electron. Since the squared matrix element is the Fourier transform (from $\mathbf{R}$ to $\mathbf{Q}$), integrating over $\mathbf{Q}$ yields

$$P \propto \int d^2\mathbf{R} \left| \langle n|\hat{H}(\mathbf{R})|0\rangle \right|^2 \left| \psi_{\perp}^{i}(\mathbf{R}) \right|^2, \tag{5.7}$$

according to the Plancherel theorem. This demonstrates that the probability does not contain any interference between different lateral positions of the electron (i.e., it is the incoherent superposition of different lateral positions, weighted by the transverse electron density profile). This conclusion would change if we were to collect the transitions associated with a single final state (i.e., a fixed $\mathbf{Q}$, or equivalently, an outgoing electron scattering direction) or a small range of wave vectors $\mathbf{Q}$. In that case, Eq. 5.7 no longer applies, and interference terms can appear.

5.4.2. Analytical solution for TR emission

TR is a coherent form of CL emission, with a characteristic angular emission distribution. The electric far field of TR can be calculated as a function of position in the far field ($\mathbf{r} = (\theta, \phi, r)$) as

$$\mathbf{E}_{\mathrm{TR}}(\mathbf{r}, \omega) = i k_0 \cos(\theta) D \mu_1 \frac{e^{i k_0 r}}{r} \hat{\theta}, \tag{5.8}$$

where k_0 is the vacuum light wavenumber ($k_0 = 2\pi/\lambda$) and D is given by Eq. 5.2. The resulting CL emission probability is then given by

$$\Gamma_{\mathrm{CL}}(\theta) = \frac{c}{8\pi^2 \hbar \omega} |\mathbf{E}_{\mathrm{tot}}|^2 r^2 \sin(\theta). \tag{5.9}$$

When the e-beam is transversely broadened, CL is emitted from the entire interaction disk of the e-beam and the Si_3N_4 substrate, given by

$$\Gamma_{\mathrm{CL}}(\theta) \propto \sin(\theta) \left| \sum_{\mathbf{r'}} A_{r'} \mathbf{E}_{\mathrm{tot}}(\mathbf{r}-\mathbf{r'})(r-r') \right|^2 \tag{5.10}$$

with $A_{r'}$ the weight of the contribution of the electrons at a distance r', effectively the electron density within the e-beam. To take into account the 50-nm bandwidth of the filter that we use in experiments, we integrate Eq. 5.10 from 475 nm to 525 nm with steps of 1 nm.

5.4.3. Spatial resolution analysis

To characterize the spatial resolution of the SEM we used an analytical method based on the power spectrum (2D Fourier transform analysis)[153, 154]. We acquired a high-resolution SEM image of a sample with Au particles in the range of 2-30 nm diameter on carbon (Agar Scientific). We extracted a square image of 1000x1000 pixels. To prevent artifacts due to sharp edges in the image, we applied a radial Hann filter, given by

$$I(r) = \frac{1+\cos(\frac{2\pi r}{N-1})}{2}, \tag{5.11}$$

where r is the distance to the center of the image, and N is the size of the image. The resulting SEM image with the applied Hann filter is shown in Figure 5.5a. Next, we took the 2D Fourier transform shown in Figure 5.5b and determined the highest frequency present in this image, which corresponds to the inverse of the smallest distance that can be resolved in the SEM. Figure 5.5c shows the radial average of the Fourier transform, with the orange line indicating where the gradient of the power spectrum becomes flat. The threshold was found at $0.22\,\mathrm{nm}^{-1}$, corresponding to the smallest distance that can be resolved of 4.4 nm. Although this method provides a way to determine the spatial resolution, and thus the e-beam spot size, in the SEM, vibrations in the microscope can lead to artifacts in the power spectrum. Such artifacts can be seen in Figure 5.5b as a dark vertical line.

5.4.4. Experimental setup and methods

Angle-resolved CL measurements

The AR CL measurements are performed in a Helios5UX scanning electron microscope (SEM; Thermo Fisher Scientific Inc., MA, USA), equipped with a Schottky FEG source. The electron energy used was 30 keV, with a beam current of 1.6 nA. For the AR CL measurements, a half-parabolic mirror was placed in between the sample and the pole piece, that collected the emitted light and directed it onto a camera (SPARC Spectral, DELMIC BV, The Netherlands). From the known parabolic geometry of the mirror, the image on the camera can be converted to the angular emission pattern. For the AR CL measurements a 50-nm bandwidth filter was used centered around 500 nm wavelength, and an exposure time of 300 s per pixel was

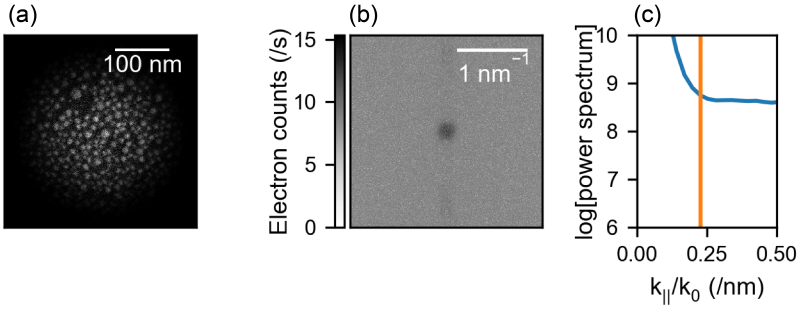

Figure 5.5: Characterization of spatial resolution through the power spectrum analysis. (a) High resolution SE image of a calibration sample consisting of 2-30 nm sized Au particles on carbon with an applied Hann filter. (b) 2D Fourier transform of (a) and (c) the radial average of (b). The orange line indicates the threshold to determine the offset of spatial frequencies included in the SE image, corresponding to a spatial resolution of 4.4 nm.

used. For the TR from a thin film of Si_3N_4 film, the e-beam was first focused on the surface, and for the defocused measurement, the sample was placed 2 mm above the focal point. We used SEM images of the sharp edge of the Si_3N_4 to estimate that the e-beam spot diameter was 6 µm.
For the double pillar configuration shown in Figure 5.4, an e-beam current was used of 0.8 nA, an electron energy of 30 keV, and an exposure time of 300 s. The out-of-focus measurement was done with the sample 84 µm above the focal point, corresponding to an estimated e-beam spot diameter of 500 nm.

Angle- and spectrally resolved CL measurements

The AR spectral CL measurements were performed in an FEI Quanta FEG 650 scanning electron microscope (SEM; Thermo Fisher Scientific Inc., MA, USA) equipped with a Schottky electron source using electrons with an energy of 30 keV and a current of 1.5 nA. In order to measure the AR spectral CL measurements, the same collection system was used as for the AR CL measurements using a vertical slit to select only a narrow radial angle. Next, this was projected onto a spectrometer to acquire the CL data depending on wavelength and azimuthal angle simultaneously. For the double pillars on top of each other (Figure 5.2), an exposure time of 360 s was used and for the slightly displaced pillars (Figure 5.3), 300 s was used. In all cases the substrate was in the focal point of the parabolic mirror.

Sample fabrication

The samples were fabricated using electron beam induced deposition (EBID) in a Helios5UX scanning electron microscope (SEM; Thermo Fisher Scientific Inc., MA, USA). The used substrate was a piece of single crystalline Si for the double pillars on top of each other and a 15-nm thin Si_3N_4 TEM grid (Ted Pella), both covered with 50 nm of Au using a 2-nm thin adhesion layer of Cr (EM ACE600, Leica, Inc.).

A Pt or W wire was grown under a 45° tilt angle, using a 2 keV e-beam. Placing the pillars next to each other and increasing the dwell time for one pillar resulted in displaced pillars in the horizontal direction, with different heights. Next, in case we wanted to eliminate the contribution from TR (Figure 5.3 and 5.4), focused ion beam milling (FIB) was used to remove the Si_3N_4 window underneath, after which the entire sample was coated with 50 nm of Au.

6

Low-energy scanning transmission electron microscopy

In this chapter, we develop and characterize scanning transmission electron microscopy (STEM) capabilities within a low-energy scanning electron microscope (SEM) to investigate the lateral coherence properties of free electrons. We first quantify the performance of the system, demonstrating a spatial resolution of 4.4 nm and a tunable semi-convergence angle ranging from 1 to 8 mrad, depending on the working distance and aperture configuration. Using single-crystalline Au flakes and a monolayer of graphene, we obtain high-quality selected-area electron diffraction (SAED) maps and convergent-beam electron diffraction (CBED) patterns, respectively, validating the system's ability to probe crystallographic information at an accelerating voltage of 30 keV.

Building on these capabilities, we implement a method, that is adapted from techniques traditionally used in transmission electron microscopy, to measure the degree of lateral coherence of the SEM electron beam. By analyzing interference between two electron wave vectors separated by 0.031 $Å^{-1}$, we extract a degree of lateral coherence of approximately 60%.

Together, these results establish STEM in the SEM as a powerful and accessible platform for measuring electron diffraction at low voltages. This capability paves the way towards measuring the full spatial coherence function of the electron, which is necessary for future coherence-sensitive electron–light-matter interaction experiments.

6.1. Introduction

Scanning transmission electron microscopy (STEM) is a powerful technique for studying the structural properties of materials at the nanoscale. Traditionally, these experiments are performed in a transmission electron microscope (TEM), where samples can be imaged with atomic resolution and electron diffraction patterns recorded for phase, orientation, or strain mapping[155]. With advances in detector speed and computational power, four-dimensional (4D) STEM has become available: the electron beam (e-beam) is scanned over the specimen, and for every pixel a two-dimensional (2D) diffraction pattern is collected, resulting in a rich 4D dataset that captures both spatial and reciprocal-space information. Because lower-energy electrons undergo stronger inelastic scattering, 4D-STEM measurements are typically carried out in a TEM operating at 80–200 keV. However, performing similar measurements in a scanning electron microscope (SEM), which operates at much lower electron energies (1–30 keV), can offer unique advantages.

In the SEM, diffraction studies are most commonly performed using electron backscatter diffraction (EBSD)[156]. Conventional EBSD is conducted with a sample tilt of 70°, and the resulting Kikuchi patterns are used to determine the crystallographic orientation and morphology of grains. These Kikuchi patterns arise from incoherent scattering events that create local sources of backscattered electrons; these electrons then diffract from the crystal lattice, producing characteristic line patterns rather than the spot or ring patterns seen in conventional TEM-based electron diffraction. One major advantage of EBSD is that, because it measures backscattered electrons, it does not require electron-transparent samples and it can probe the near-surface region of the specimen, with the sampling depth depending on the beam energy. However, EBSD signals often suffer from a low signal-to-noise ratio, since only a small fraction of the incident electrons are backscattered. Performing STEM in the SEM, could significantly improve the signal quality, offering a complementary and in some cases more sensitive approach to structural characterization in the SEM[74, 157].

For example, due to the lower energy in the SEM, STEM has a higher sensitivity to strain, tilt or defects[158]. Next, the electron scattering interaction probability is higher, especially for intrinsically thin samples, like van der Waals materials. For example, the ratio between Moiré peaks over first-order diffraction peaks is approximately linear with the interaction parameter of the material. The interaction parameter for elastic scattering in graphene increases from 0.81 $\mathrm{keV}^{-1}\,\mathrm{Å}^{-1}$ for an e-beam energy of 100 to 25.61 $\mathrm{keV}^{-1}\,\mathrm{Å}^{-1}$ for 0.1 keV, respectively[159]. Caplins *et al.*. have implemented diffraction measurements in the SEM, and used it for orientation mapping of graphene[160]. Furthermore, Schweizer *et al.*. compared tilted diffraction patterns of crystalline Si and observed higher-order Laue-zone rings appearing for 30 keV[161].

In this work, we develop 4D-STEM in the SEM to measure diffraction patterns of transmitted electrons. We demonstrate 4D-STEM data of thin Au flakes, where we map the surface tilt. By reducing the working distance (WD) between the sam-

ple and electron column, we obtain convergent beam electron diffraction (CBED) measurements of van der Waals materials. We use a monolayer of graphene to characterize the SEMs semi-convergent angle and then we adapt a technique used in TEMs to measure the degree of lateral coherence. We begin our analysis with an overview of key parameters in electron microscopy.

6.2. Electron microscopy

Electron microscopes use two main kinds of electron sources. Thermionic sources use heat to overcome the tunneling barrier to emit electrons from a cathode material. Field emission guns (FEG), in contrast, rely on a strong electric field applied to a sharp metallic tip to extract electrons. The Schottky source in our SEM is a thermally assisted FEG; a tungsten tip is heated by a filament current while a strong extractor voltage pulls electrons from its apex. Each source type differs in key parameters, like brightness, temporal spread, and lateral coherence. The brightness of a source is defined as the number of electron current (dI) per unit area (dA) per unit solid angle ($d\Omega$). The brightness is conserved within the e-beam at constant operating conditions: when the cross sectional area of the beam is modified, the current scales proportionally. Beam brightness depends on the acceleration voltage: electron acceleration generally reduces brightness, while deceleration increases it. Since the dependence of brightness (B) on acceleration voltage (V) is inversely linear, we can define the reduced brightness (B_r) as

$$B_r = \frac{dI}{dA d\Omega V}. \tag{6.1}$$

For a Schottky FEG, the approximate reduced brightness is $5\times10^8\,\mathrm{A\,m^{-2}\,sr^{-1}\,V^{-1}}$ [24]. Only a few physical processes, such as Coulomb interactions between electrons or energy filtering, can significantly alter the brightness. Although this definition of the reduced brightness assumes a constant current density across the e-beam, in practice, the beam profile has a current density distribution that peaks at the center of the e-beam.

To achieve high-resolution imaging, lateral coherence is essential. Coherence between two points within the e-beam is defined by the fact that there is a constant phase relation between them. This then can result in interference, which is the basis of electron diffraction. Electrons, unlike photons, are fermions and therefore, two electrons are never mutually coherent and interference occurs within a single electron. A perfectly coherent e-beam is generated when electrons originate from the same point within the source, and would create an electron wave packet that is spread laterally over the full beam width. Typically, in electron microscopes, the lateral coherence function is spatially limited, given by the Fourier transform of the real-space intensity distribution at the source[162]. The current within a coherent area (I_{coh}) can be related to the reduced brightness as[162]

$$I_{\mathrm{coh}} = B_r V \frac{\pi^2}{4}\left(\frac{\lambda}{2}\right)^2 = 0.9\times10^{-18} B_r, \tag{6.2}$$

where λ is the de Broglie wavelength of the electron[162]. This relationship shows that the degree of lateral coherence of the e-beam is not so much a result of the setting of the source but rather defined by the final aperture. For a Schottky FEG (B_r =5 × 10^8 A m^{-2} sr^{-1} V^{-1}), the current has to be reduced to the order of 100 pA to achieve a fully coherent beam.

Similar to the lateral coherence given by the Fourier transform of the intensity distribution at the source, the temporal coherence is given by the Fourier transform of the energy spectrum of the e-beam, essentially the energy spread (ΔE) of the e-beam. For a Schottky FEG, the energy spread is approximately 0.3-0.8 eV, corresponding to a temporal coherence length of 1000-500 nm, given by[152]

$$l_c^{\text{temporal}} = \frac{v_e h}{\Delta E}, \tag{6.3}$$

where v_e is the relativistic electron velocity and h is the Planck's constant. This energy spread is the main contributor to chromatic aberration in SEM and TEM, since electrons with different energies have slightly different beam paths and hence focal points[152].

Experimental methods to measure the lateral and temporal coherence in the SEM are not well established. Typically, in the SEM, the e-beam current is high, and the resolution is more limited by aberrations in the electron column than by the degree of coherence. Methods are reported to measure the point spread function of the e-beam in SEM. Zotta *et al.* compared measured secondary-electron of small particles with distributions calculated with Monte Carlo simulations to derive the point spread function[163]. Furthermore, Kamal *et al.* derived the electron profile in the SEM by incorporating the effect of lateral coherence in analysis of the spatial resolution[152]. Directly measuring lateral coherence, however, is more challenging and has not been achieved in the SEM. The temporal coherence in the SEM can be estimated by measuring the energy spread of the e-beam. This has been measured in the SEM that we use, with a retarding field analyzer, yielding an energy spread of approximately 0.7 eV at an accelerating voltage of 4 keV[164]. Lower values, down to 0.3 eV, are found for specific beam settings[165].

In TEMs, several established methods exist to assess the lateral coherence or effective source size of the electron probe[166]. One common approach involves analyzing a coherent convergent beam electron diffraction (CBED) pattern, named a ronchigram, from an amorphous sample to identify the onset of spherical aberrations[167] and choose a small aperture to eliminate these contributions. To reach the necessary spatial resolution for such measurements, an effective camera length of several meters is typically required. Similar long camera lengths are also needed for direct measurements of Airy diffraction from a selective aperture[168, 169]. For example, Hatanaka *et al.* measured the lateral coherence length in the TEM for a parallel e-beam for various electron sources[170]. They found a maximum spatial coherence length of 1.2 µm at the specimen plane using a Schottky FEG with a e-beam diameter of approximately 120 nm. To fit the Airy diffraction patterns, they used an effective camera length of 200 cm with an additional mag-

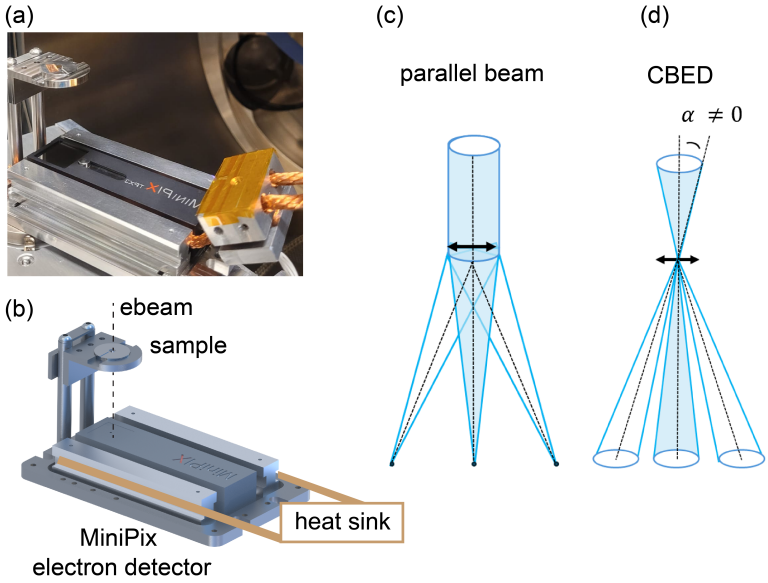

Figure 6.1: Experimental setup for STEM in the SEM. (a) Photograph and (b) schematic representation of the STEM holder with the single electron detector underneath and schematic representation of two measurement geometries: (c) diffraction of a parallel e-beam, and (d) convergent beam electron diffraction (CBED).

nification of 8x. Such requirements make this technique impossible to use in the SEM, where the geometry and lens configuration do not allow for these large effective camera lengths.

An alternative method for assessing lateral coherence involves recording a ronchigram where the diffraction disks partially overlap[171, 172]. In the overlapping regions, electrons originating from different virtual sources interfere, producing interference patterns. The visibility of the interference pattern in the overlapping disk is related to the degree of coherence at a specific spatial frequency determined by the crystal structure. Using two different orientations of diamond, Dwyer *et al.*[171, 172] extracted the degree of coherence at four spatial frequencies, reconstructing the lateral coherence function over the e-beam. Alternatively, Herring *et al.* demonstrated diffractive beam holography, using 300 keV electrons diffracting from a Ge sample[173]. After the interaction with the crystalline specimen, the e-beam was recombined using an electron biprism. Such experiments are more complex to perform in the SEM, where the use of a biprism is not common, the electron optics is less advanced and the angular range limited. Furthermore, these types of measurements yield the degree of coherence between electrons diffracted at specific spatial frequencies defined by the specimen. To obtain a fully comprehensive picture of the lateral coherence function over the e-beam, a range of measurements must be

performed using materials with a range of lattice spacings from which the coherence distribution can then be reconstructed.

6.3. STEM in the SEM

To perform 4D-STEM in the SEM, we use a single-electron counting detector (Minipix, Advacam). The sample is loaded above the detector at a camera length between 1 and 7 cm. To keep the detector at a constant temperature, the holder is connected to a heat sink cooled with liquid nitrogen. Figure 6.1a,b shows a photograph of the experimental setup in the SEM, together with a schematic representation, respectively.
We scan the e-beam over the sample and measure a 2D diffraction image for each pixel at the sample. When we use a small convergent angle beam, the diffraction pattern on the camera consists of spots, while using a higher semi-convergent angle they become disks, where the diameter directly represents the semi-convergent angle of the beam. Depending on the WD and aperture settings we are either in the regime where we use a parallel beam with a semi-convergent angle of around 1 mrad, or where we measure CBED, with a semi-convergent angle of approximately 8 mrad. See Figures 6.1c,d for a schematic of both configurations.

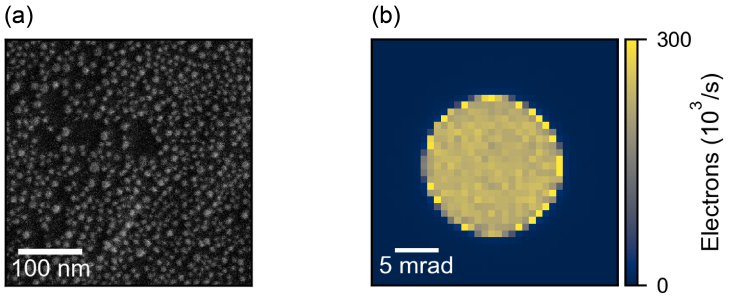

Figure 6.2: SEM characterization. (a) High-resolution SE image of a calibration sample with Au particles with diameters between 2-30 nm diameter, and (b) the angular spread of the e-beam, directly imaged on the single-electron detector at a cameral length of 6.65 cm.

6.4. Results

6.4.1. SEM characterization

First, we characterize the SEM using an acceleration voltage of 30 keV and image a calibration sample that consists of semi-spherical Au particles with diameters between 2-30 nm, see Figure 6.2a. Using the power spectrum analysis described in section 5.4.3, we find a spatial resolution of 4.4 nm at a WD of 4 mm. Furthermore, we determine the semi-convergent angle of the e-beam by imaging a direct beam that is focused on the sample plane using a camera length of 6.65 cm, by remov-

ing the sample, as shown in Figure 6.2b. The corresponding semi-convergent angle is 8.4 mrad. The corresponding Abbe limit related to the electron wavelength (λ_e =6.9 pm for 30 keV electron energy) is 0.4 nm, indicating that the SEM is not operating under diffraction-limited conditions, which is due to inelastic scattering in the larger interaction volume, the spherical aberrations in the SEM, and the limited temporal and lateral coherence.

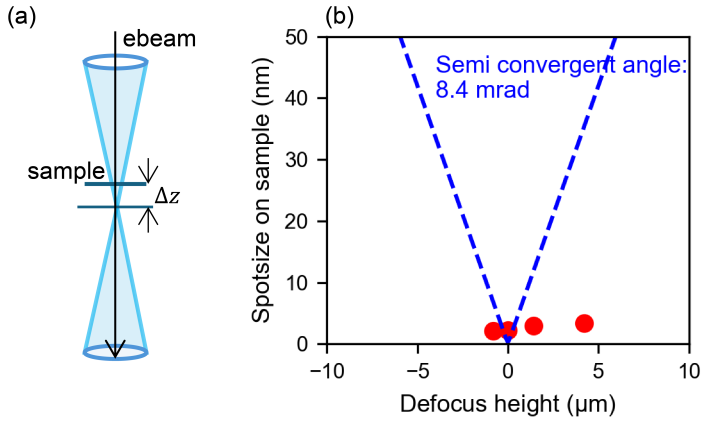

Figure 6.3: Measurement of e-beam waist. (a) Schematic representation of a measurement where the sample is vertically displaced with respect to the beam focus, and (b) the corresponding resolution measurements at different heights (red dots), compared to the solution for a perfect Gaussian beam (blue dashed)

Next, we further study the shape of the e-beam along its trajectory. If the e-beam has a perfect Gaussian lateral distribution with diffraction-limited resolution, the waist of the beam (w) along its trajectory (z) is given by[174]

$$w(z) = w_0\sqrt{1+\left(\frac{z}{z_R}\right)^2}, \tag{6.4}$$

where w_0 is the radius of the e-beam waist and z_R is the Rayleigh length ($z_R = \pi w_0^2/\lambda$). Changing the WD while keeping the sample at the same height, we can determine the height-dependent waist. Figure 6.3a shows a schematic of this measurement, where the focus of the e-beam is moved a distance Δz below and above the sample. The corresponding resolution is measured using a power spectrum analysis[153, 154]. The measured data is shown is red dots in Figure 6.3b: the smallest beam waist (half the resolution) is found to be 2.1 nm; it increases when the sample is out of focus. However, comparing the experimental results to the expected waist of an e-beam with a semi-convergent angle of 8.4 mrad (blue dashed line), we find a significant difference. Surprisingly, the experimental data indicate that the achieved resolution is below the calculated waist.

First of all, there is a uncertainty on the height of the sample above the focus. The mechanical stage in the SEM has a step resolution of around 1 µm and at the same time the SEM uses a model to calculate the WD, which might nog be correctly calibrated at these small distances. Furthermore, there is an additional discrepancy due to the complex spatial structure of the electron probe at the sample plane, which depends on the height relative to the focal point. Within the semi-convergence angle, the e-beam exhibits a uniform angular amplitude rather than the Gaussian lateral profile assumed in our analysis above. Consequently, the beam intensity at the sample can adopt nontrivial shapes that vary with radial distance from the beam center. In section 6.6.1, we calculate the expected probe profiles for different defocus values and find that the effective probe size can be smaller than predicted by the Gaussian model. This effect could explain the discrepancy between experiment and calculation observed in Figure 6.3. To fully match this to the measured resolution, a proper analysis of the convolution of the probe at the sample plane and the sample should be taken into account.

6.4.2. Selected-area electron diffraction

Next, we perform 4D-STEM measurements on a single-crystalline Au flake fabricated using gap-assisted chemical synthesis[175], by Kiani *et al.*. The Au flakes are deposited on a 15 nm thin Si_3N_4 membrane, which is sufficiently thin to be transparent to the e-beam. Measurements are conducted at an electron energy of 30 keV, a WD of 20 mm, and a camera length of 4.7 cm. Figure 6.4a shows the SE image of the Au flake above the window. The corresponding diffraction pattern recorded by averaging over the scan area is shown in Figure 6.4b. The hexagonal symmetry of the pattern confirms diffraction from the face-centered cubic (fcc) lattice of Au along the [111] zone axis. By averaging, local structural information such as strain and sample curvature, are averaged out over the measured area.

To analyze the observed pattern, we calculate the expected diffraction pattern from the Bragg condition for Au at normal incident angle, shown in Figure 6.4c (see section 6.6.2 for the calculation). Diffraction occurs when the Ewald sphere intersects a reciprocal lattice point, resulting in a strong diffracted intensity. The intensity variation between diffraction spots depends on the sample tilt. Such a variation is visible in Figure 6.4b, as two brighter diffraction spots are observed on both sides of the center beam (indicated by the red cross). To investigate this further, we select one diffraction spot (marked by the red dashed circle) and form a transmitted electron image using only electrons from this this diffraction order, shown in Figure 6.4d. This image reveals spatial regions within the flake where the selected diffraction spot has high intensity. The corresponding diffraction pattern is shown in Figure 6.4e, displaying only those diffraction spots that satisfy the Bragg diffraction condition. We can reconstruct this diffraction pattern in calculations if we assume a tilt angle of 6.5° (see Figure 6.4f), such a tilt is not unexpected for such thin Au flakes. In both experiment and calculation, we see the typical circle where the Ewald sphere intersects the reciprocal lattice points with its center on the top left of the image. We note that due to the lower electron energy compared to regular TEM, the Ewald

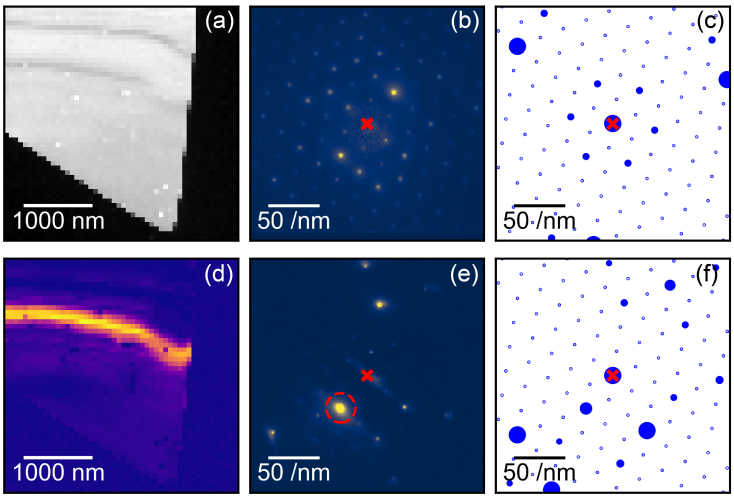

Figure 6.4: Selected-area electron diffraction of a thin Au flake. (a) SE image of the thin Au flake. (b) Average diffraction pattern collected over the entire flake, and (c) calculated diffraction pattern for normal-incident electron, where the size of the spot represents the intensity in the diffraction spot. (d-f) Analysis of the sample surface tilt with respect to the e-beam. (d) Transmitted electron image for electron in one spot indicated by the red dashed circle in (e). (e) Diffraction pattern for the location where this spot has the maximum intensity, and (f) calculated diffraction pattern for a tilt angle of 6.5°.

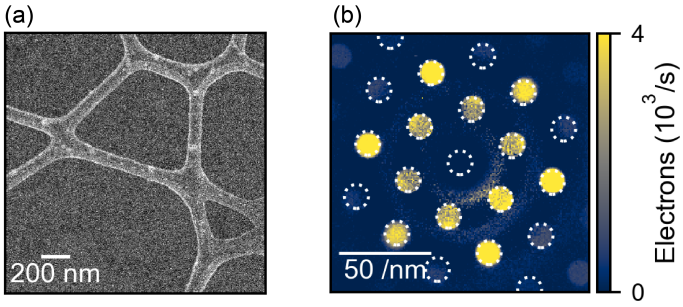

Figure 6.5: CBED of monolayer graphene. (a) SE image of the monolayer of graphene supported by lacey carbon and (b) the CBED pattern from this monolayer using an electron energy of 30 keV, a working distance of 4 mm, a camera length of 6.7 cm, and a semi-convergent angle of 8 mrad.

sphere has a smaller curvature.

6.4.3. Convergent-beam electron diffraction

Next, we decrease the WD to enter a regime where we have a large semi-convergent angle, approximately 8 mrad, depending on the aperture settings. This allows us to study CBED. As a model system, we first study a monolayer of graphene (Ted Pella) supported by a lacey carbon grid. Figure 6.5a shows the SE image of the sample, where the area in between the wires is composed of a monolayer of graphene. Using an electron energy of 30 keV, a WD of 4 mm and a camera length of 6.7 cm, we record the CBED pattern shown in Figure 6.5b. We clearly see the diffraction pattern associated with the hexagonal crystal lattice of graphene, however, instead of measuring discrete spots as before, we measure diffraction disks due to the range of incident angles within the semi-convergent angle. When we calculate the expected CBED pattern from the known cameral length and semi-convergent angle and overlay the disks with the data (white dashed contours), we find excellent agreement. Small deviations in the disk positions may arise from local strain within the graphene layer. However, with our current angular resolution of ~1 mrad, such fine variations cannot be resolved.

Next, we investigate how the size of the electron probe affects the size of the diffraction disks. We hypothesize that an increasing probe size causes a larger portion of the lattice to contribute coherently to the diffraction pattern, resulting in sharper diffraction disks. This effect should reflect the lateral coherence of the e-beam, as a more incoherent e-beam would lead to blurred diffraction features. To test this hypothesis, we first acquire a CBED pattern in focus (probe diameter of 4.4 nm) and take the average intensity calculated by summing all second-order diffraction spots, each centered around their center of mass, as shown in Figure 6.6a.

For comparison, Figure 6.6b presents a cross-section through the center of the

summed diffraction spots, together with the direct beam profile measured under identical conditions (data from Figure 6.2b). We fit the diffraction spot intensity to a convolution of a Gaussian distribution that accounts for the lateral coherence, and a block function describing the angular range of the incident e-beam (see section 6.6.3 for details). The resulting fit (blue dashed line) yields a semi-convergent angle of 7.2 mrad and a coherent diameter of 3.8 nm. The found semi-convergent angle is slightly smaller than that of the direct beam (8.4 mrad), and the derived coherent diameter corresponds to a coherence fraction of the total beam area of approximately 75 %.

To further evaluate this model, we repeat the experiment where we intentionally move the focal point to 20 µm below the sample, thereby increasing the probe size to a diameter of 300 nm. The corresponding summed diffraction spot and crosscut are shown in Figure 6.6c,d, respectively. Surprisingly, the fitted parameters, a semi-convergent angle of 7.2 mrad and coherent diameter of 3.6 nm, are nearly identical to the in-focus case. In principle, if the degree of coherence is conserved along the e-beam trajectory, a larger probe size should correspond to a proportionally larger coherent diameter. The absence of this trend in our measurements suggests that the observed diffraction behavior is dominated by other factors such as the temporal coherence and aberrations. Therefore this approach cannot be used to reliably determine the lateral coherence of the e-beam with a large semi-convergent angle.

6.4.4. Ronchigrams

Next, we apply a technique to measure the lateral coherence that is adapted from a method previously demonstrated in the TEM, using CBED[171]. To determine the lateral coherence, we measure CBED patterns on a bilayer of graphene under conditions where the diffraction disks overlap. Figure 6.7a shows the schematic representation of the experiment. The detector is placed at a distance (Z) below the focal point of the e-beam, while the sample is placed above the focal point by a distance Δf. The bilayer sample consists of two graphene layers spaced by a vertical distance d, each acting as a diffracting plane for the e-beam. As the vertical distance d, combined with de Broglie wavelength of the electron (λ =6.98 pm), results in a slight difference in diffraction k-vector for each layer, which in turn results in two partially overlapping disks. In the area where they overlap, the detected intensity reflects the sum of diffracted electrons contributions that originate from two virtual point sources, S^1 and S^2. The phase difference between these contributions results in an interference pattern in the overlap region of each set of disks. The period of the interference pattern depends on the spacing between the layers (d) and the distance from the sample to the focal point (Δf).

In the bilayer of graphene, the interlayer spacing equals the out-of-plane lattice constant of 3.35 Å[176]. Because this separation is small, the resulting interference fringes are expected to be widely spaced, making them unresolvable within a single diffraction disk. To overcome this limitation, we employ a twisted bilayer

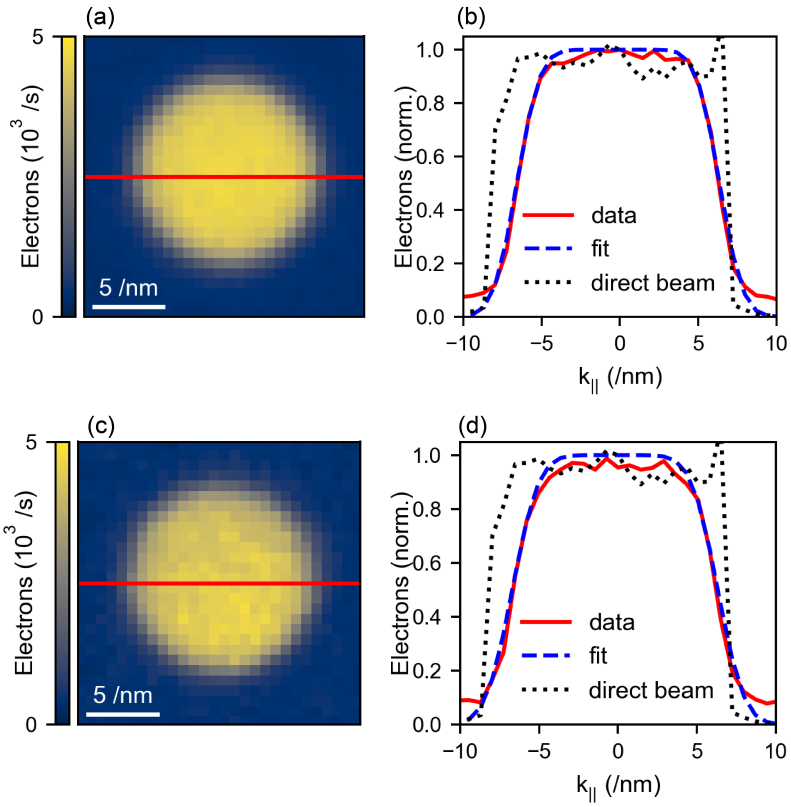

Figure 6.6: Size of CBED disks. (a) Average intensity of all second-order diffraction spots and (b) the profile along the center (red) and fit to a convolution of a Gaussian and a block function, compared to the measured profile of the direct beam (black dashed) from Figure 6.2. (c,d) show the same analysis when the monolayer of graphene is 20 µm above the focal point, resulting in an e-beam spot diameter of 300 nm.

of graphene with a small twist angle (β). The relative rotation between the two layers introduces a lateral displacement of their reciprocal lattice points, which implies that the corresponding virtual sources are also separated in the horizontal plane. This additional separation produces a sufficient phase difference between the diffracted beams to generate a visible interference pattern, as illustrated schematically in Figure 6.7b. CBED interference patterns have been used in the TEM to study van der Waals materials in the TEM[176–181]. Kazmierczak *et al.* showed to maps of strain fields in twisted bilayer graphene[182], and Latychevskaia *et al.* showed how to use a twisted bilayer of graphene and hBN to determine out-of-plane atomic displacements[176]. In this chapter, we investigate its use to determine the lateral coherence.

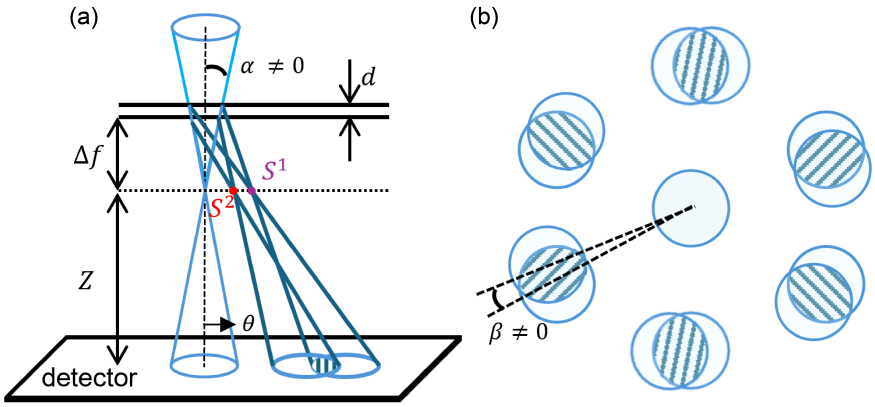

Figure 6.7: Schematic representation of CBED. (a) CBED for a bilayer of material with an interlayer distance d resulting in radially displaced diffraction disks and (b) the overlapping diffraction disks for a twisted bilayer of material.

Calculation

First, we calculate the expected interference pattern for a perfectly spatially coherent beam. We start with determining the positions of the two virtual point sources, which depend on the twist angle, interlayer distance, and defocus height. Next, we propagate the corresponding electron wavefront from these virtual sources to the detector plane. The resulting interference intensity distribution is obtained from the coherent superposition of the two waves (see section 6.6.4 for a detailed description). For the calculation, we use a twist angle of 0.6°, an electron energy of 30 keV, and a semi-convergent angle of 7 mrad. The sample is placed 6 µm above the focal plane and the camera length is 6.65 cm.

Figure 6.8a shows the corresponding calculated CBED pattern for a perfectly coherent beam. The overall diffraction geometry closely resembles that observed experimentally for a monolayer of graphene; however, within each diffraction disk, we now observe a distinct interference pattern. The period of the interference decreases for the higher-order diffraction disks, and their orientation rotates according to the position of the disk with respect to the direct beam: the fringes are always perpendicular to the vector connecting the two disks. Because the twist angle is small, the two disks are nearly coincident and cannot be easily distinguished.

To analyze the fringe structure in more detail, we select two disks, indicated by the blue and purple squares in Figure 6.8a; enlarged images are shown in Figure 6.8b,c, respectively (scale bar 5 nm^{-1}). Around the outer region of each disk, we see an area where there is no overlap in which no interference fringes are observed. Taking the Fourier transform of the enlarged images allows us to study the distance between the virtual sources contributing to the interference pattern, shown in Figure 6.8d,e

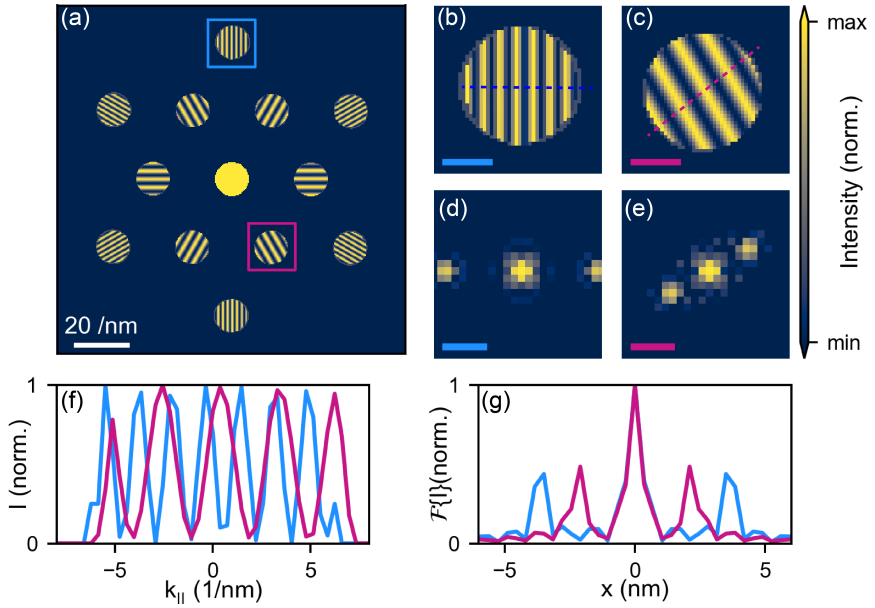

Figure 6.8: Calculated CBED pattern for a twisted bilayer of graphene. (a) The full CBED pattern until the second order, calculated for a twist angle of 0.6° and a defocus of 6 µm (according to section 6.6.4). (b,c) Enlarged images from (a) for two diffraction disks indicated by the blue and purple square (scale bar 5 nm^{-1}) and (d,e) their 2D Fourier transform (scale bar 2 nm), respectively. (f) Line scans perpendicular to the interference patterns in (b,c) in blue and purple, respectively, and (g) their Fourier transform.

with the scale bar indicating 2 nm. We can take a line scan perpendicular to the interference fringes in Figure 6.8b,c, and take the Fourier transform to study the visibility and spacing of the fringes, see Figure 6.8f,g. The distance related to this interference is 2.2 nm and 3.5 nm for the first and second order diffraction spot, respectively. This distance is associated with the real-space distance between the virtual sources S^1 and S^2. Furthermore, since in the calculation we assume a perfectly coherent e-beam and an equal scattering intensity from each layer, the fringe visibility reaches 100 %.

Experiments

To experimentally measure the lateral coherence in the SEM, we measure CBED patterns from a commercial bilayer of graphene (Ted Pella). The sample contains many small graphene flakes with varying twist angles and numbers of layers. We place the sample 6 µm above the focal plane and probe multiple regions to identify an area with a suitable twist angle for producing visible interference fringes. Figure 6.9 shows the CBED results of an area exhibiting clear interferences fringes. Figure 6.9a shows the full CBED pattern recorded on the single-electron detector

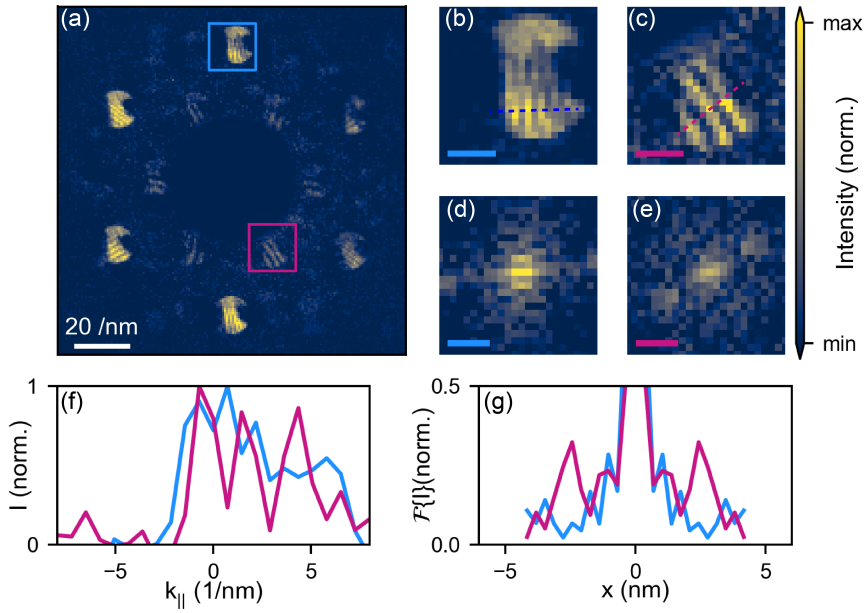

Figure 6.9: Measured CBED pattern for a twisted bilayer of graphene. (a) The full CBED pattern with the background subtracted, resulting in the dark disk in the center. (b,c) Enlarged images from (a) for two diffraction disks indicated by the blue and purple square (scale bar 5 nm^{-1}) and (d,e) their 2D Fourier transforms (scale bar 2 nm), respectively. (f) Line scans perpendicular to the interference fringes in (b,c) in blue and purple, respectively, and (g) their Fourier transform.

after background subtraction to remove contributions from inelastically scattered electrons. The dark central disk in the image is an artifact of the background subtraction related to oversaturation of the detector in this area. Within each disk, a dark spot appears at the same position in each disk. We assign this to a shading effect due to a small contamination that blocks part of the transmitted electrons; in this measurement the e-beam diameter is approximately 80 nm.

Around the shaded region, a distinct interference pattern is visible. The fringes rotate according to the orientation of the diffraction spot with respect to the center beam as expected. This behavior is more clearly seen in the enlarged images of two specific spots indicated by the blue and purple square, shown in Figure 6.9b,c, respectively. The Fourier transforms of the interference patterns (Figures 6.9d,e) reveal components corresponding to the fringe spacing, although the image quality is affected by the shaded regions in the CBED disks. The fringe orientation and periodicity match the calculated results from Figure 6.8 well, demonstrating good agreement between experiments and calculation for Δf =6 µm and β =0.6°.

To measure the fringe visibility, we take a line scans of Figure 6.9b,c, indicated by

the blue and purple dashed line, and compute the Fourier transforms, shown in Figure 6.9f,g, respectively. Although the visibility is much decreased compared to the calculated case (note the different y-scale in panel (g)), we clearly see a peak in the Fourier transform. For the first diffraction order (purple), we find a peak at 2.4 nm with a visibility of approximately 60 %, while for the second diffraction order (blue), the peak is found at 3.5 nm with a visibility of 20 %. A decreasing trend in visibility for larger wave vectors is expected, given the limited coherence of the e-beam. A precise analysis of these numbers is difficult as the measured visibility of the smallest wave vector is sensitive to the background subtraction of the signal of the direct beam.

Similar to the work done by Dwyer [172], who used two facets of diamond to achieve the e-beam coherence function, we can use this measurement to extract the degree of coherence, related to the visibility. This visibility arises from a combination of the finite lateral coherence of the e-beam and the varying number of atomic layers contributing to each diffraction spot[158]. Because the twist angle is small, the diffraction disks are not separable, and the number of atomic layers in each flake is unknown. The found visibilities are associated with the lower limit of the degree of lateral coherence at the analyzed wave vector. The wave vectors correspond to the Moiré wave vectors depending on the twist angle and the diffraction order. Thus, the measurement provides two data points on the lateral coherence curve of the SEM beam, as summarized in Table 6.1. When compared to the maximum accessible wave vector in the e-beam of $0.63\,\text{Å}^{-1}$, these measurements sample only a fraction of the full range.

A more complete reconstruction of the lateral coherence function and probe shape would require repeating the measurement for other twist angles and additional diffraction orders, thereby covering a broader k-vector separation range. However, the finite pixel size of the detector imposes a lower bound on the fringe period that can be resolved (see section 6.6.4 for details).

Table 6.1: Wave vectors connecting the diffraction points of a twisted bilayer of graphene for the first and second diffraction order and a twist angle of 0.6° and the corresponding visibility of the interference fringes from Figure 6.9.

Diffraction order	k-**vector** (Å^{-1})	**Visibility** (%)
1	0.031	60
2	0.053	20

6.5. Conclusion

In this chapter, we demonstrated the development and application of 4D-STEM within a SEM operating at an electron energy of 30 keV. While 4D-STEM is traditionally performed in TEMs operating at higher energies, our work shows that similar diffraction-based analyses are feasible at the lower electron energies typical for SEMs (1–30 keV), offering complementary advantages such as higher sensitivity to

tilt, strain, or Moiré scattering, and potential future correlative experiments with angle-resolved cathodoluminescence (CL) spectroscopy.

We characterize the electron optics in the SEM and determined the minimal probe size (resolution) of 4.4 nm and a convergent angle of 1-8 mrad, depending on the chosen WD and aperture. Using a Schottky FEG, we describe how brightness and lateral and temporal coherence of the e-beam are key parameters that determine the achievable spatial resolution and diffraction. Subsequently, we applied 4D-STEM to study crystalline Au flakes, identifying their crystal lattices orientation and spacing from the measured diffraction patterns. The experiments revealed that the SEM can resolve reciprocal-space information with high precision.

We then explored CBED in the SEM by operating at larger semi-convergent angles. Using graphene monolayers, we observed the transition from discrete diffraction spots to diffraction disks, verifying the expected geometry through comparison with calculated CBED patterns. To assess the lateral coherence of the SEM beam, we have adopted a method inspired by TEM studies, using overlapping diffraction disks from twisted bilayer graphene. Calculations for a perfectly coherent beam were compared with experimental data, from which we extracted a degree of coherence of approximately 60 % and 20 % for an electron k-vector of 0.031 $Å^{-1}$ and 0.053 $Å^{-1}$, respectively.

Overall, this work establishes a foundation for 4D-STEM in the SEM, expanding the capabilities of conventional low-energy electron microscopy toward quantitative structural characterization at the nanoscale. This geometry takes advantage of the high signal-to-noise ratio for transmitted electrons and the different measurement capabilities enabled by low electron energies. Using 4D-STEM, we characterize key e-beam parameters, semi-convergent angle and degree of lateral coherence. Looking ahead, 4D-STEM can be combined with CL to directly correlate structural and optical properties within a single experiment. Ultimately, we could perform single-electron/single-photon coincidence measurements to obtain further insight into the quantum properties of electron-light-matter interactions.

6.6. Appendix

6.6.1. Spatial profile of the e-beam for a uniform angular amplitude

In section 6.4.1, we measure the probe size of the e-beam at different heights (z) above the focal point. We compare this to a perfect Gaussian beam. However, we know from the direct beam image that the lateral shape of the e-beam does not follow a Gaussian function. Therefore, we have to adjust our description of the height-dependent e-beam profile.

For this analysis, we assume a perfectly coherent e-beam with a uniform angular amplitude within the semi-convergence angle (α =8.4 mrad). Then, the beam can

be described as a function of position $\mathbf{r} = (x, y, z)$ as

$$A_e(\mathbf{r}) = \int_{Q<q_0 \sin(\alpha)} d\mathbf{Q} e^{i(\mathbf{Q}\cdot\mathbf{R}+q_z z)}, \tag{6.5}$$

where $\mathbf{R} = (x, y)$, $\mathbf{Q} = (q_x, q_y)$, $Q = \sqrt{q_x^2 + q_y^2}$ is the in-plane wave vector, and q_0 is the electron wave vector ($q_0 = 2\pi/\lambda_e$). The integral is restricted to $Q < q_0 \sin(\alpha)$ due to the semi-convergent angle of the e-beam. Under the paraxial approximation (i.e., $Q << q_0$), we write

$$q_z \approx q_0 - Q^2/(2q_0), \tag{6.6}$$

and therefore

$$e^{iq_z z} \approx e^{iq_0 z} e^{-iQ^2 z/(2q_0)}. \tag{6.7}$$

As a result, Eq. 6.5 becomes

$$A_e(\mathbf{r}) = e^{iq_0 z} \int_{Q<q_0 \sin(\alpha)} d\mathbf{Q} e^{i(\mathbf{Q}\cdot\mathbf{R})-iQ^2 z/(2q_0)}. \tag{6.8}$$

The R-dependent intensity profile of the e-beam ($I_e(R, z)$) becomes

$$I_e(R, z) = 4\pi^2 \left| \int_0^{q_0 \sin(\alpha)} dQ Q J_0(QR) e^{-iQ^2 z/(2q_0)} \right|^2 \tag{6.9}$$

where J_0 is the zeroth order Bessel function and $R = \sqrt{x^2 + y^2}$ is the transverse radial distance to the e-beam's axis[183].

For comparison, the e-beam lateral intensity associated with a Gaussian beam is given by

$$I_{\text{Gaussian}}(R, z) \propto \left| \int_0^{\infty} dQ Q J_0(QR) e^{-Q^2/\Delta^2 - iQ^2 z/(2q_0)} \right|^2, \tag{6.10}$$

where we insert an extra factor e^{-Q^2/Δ^2} in which Δ depends on the beam's semi-convergent angle, and also, the integral is extended over the entire 2D plane.

Figure 6.10 compares the intensity profile calculated for a Gaussian beam according to Eq. 6.10 (black) with the intensity obtained considering the uniform angular profile of the e-beam according to Eq. 6.9 (red). We use four values for z: (a) z =0 nm, (b) z =100 nm, (c) z =500 nm, and (d) z =10 µm. All graphs are normalized, such that the integral of $RI(R)$ from 0 to ∞ is a constant.

The Gaussian angular profile of the e-beam is clearly smooth and independent of z, apart from a lateral enlargement increasing with z. However, the intensity profile associated with a uniform angular profile shows a complex behavior. First of all, far away from the focal point (z =10 µm), we observe a flat profile, with an increased intensity at the edge of the e-beam. This explains the shape of the profile that we observe when we measure the direct beam in Figure 6.2b, that shows a uniform intensity with enhancement at the edge. Furthermore, at small displacements above the focal point, we observe oscillations in the intensity profile. Comparing

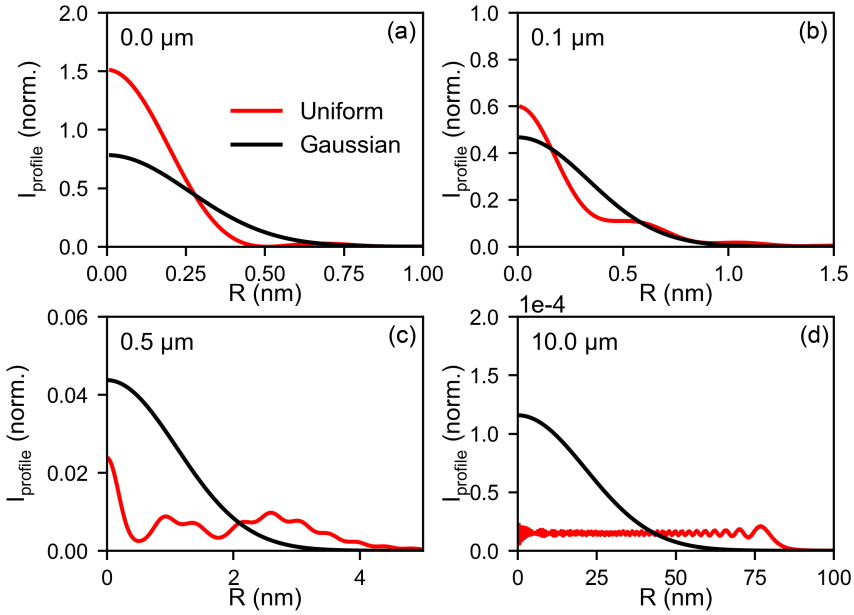

Figure 6.10: Calculated intensity profiles of the e-beam for two assumed amplitude distributions: a uniform profile (red) and a Gaussian profile (black). The beam shape is shown at four axial positions: (a) at the focal plane, and (b) 100 nm, (c) 500 nm, and (d) 10 µm above the focal point, illustrating how the probe shape evolves with increasing defocus.

the Gaussian angular profile with the uniform angular profile for z =500 nm in Figure 6.10, we find a smaller probe size associated with the latter one, which could explain the discrepancy that we observe between experiments and calculations in Figure 6.3. However, to match this to the measured resolution, a proper analysis of the convolution of the probe at the sample plane and the sample should be carried out.

6.6.2. Electron diffraction under a tilt angle

To calculate the electron diffraction pattern from a Au crystal (face-centered cubic lattice), we first computed the real and reciprocal lattices and found the overlap with the Ewald sphere. The real-space lattice of Au is given by

$$\mathbf{r}_{ijk} = a(\mathbf{n}_{ijk} + \mathbf{b}), \tag{6.11}$$

where $\mathbf{n}_{ijk}$ indexes the unit cell position, and $\mathbf{b}$ are the four-unit cell basis vectors (0, 0, 0), (0.5, 0.5, 0), (0.5, 0, 0.5), (0, 0.5, 0.5). The reciprocal lattice of a FCC crystal

is a body-centered cubic (BCC), of which the basis vectors are defined as

$$\begin{aligned}\mathbf{b}_1 &= 2\pi a(-1,1,1)\\ \mathbf{b}_2 &= 2\pi a(1,-1,1)\\ \mathbf{b}_3 &= 2\pi a(1,1,-1).\end{aligned} \tag{6.12}$$

This results in the full set of reciprocal diffraction vectors as

$$\mathbf{G}_{hkl} = h\mathbf{b}_1 + k\mathbf{b}_2 + l\mathbf{b}_3. \tag{6.13}$$

Next, the crystal was rotated so that the (111)-plane is parallel to the z-traveling e-beam. Since electron diffraction is an elastic interaction, the energy of the electron is conserved, and the diffraction spots have to satisfy $|\mathbf{G}_{hkl} - \mathbf{k}_{in}| - k_0 < \epsilon$, where ϵ is a small tolerance. The strength of the diffraction spot (size of the marker in Figure 6.3) scales inversely to the difference in reciprocal space.

6.6.3. Effect of lateral coherence on electron diffraction patterns

To study the effect of increasing probe size on the sample, we used an analytical model for the shape of the diffraction spots. Diffraction of electrons of a crystalline sample is a result of particle-wave duality of electrons. The electron is scattered by the periodic sample as a wave, resulting in an interference pattern of diffraction spots at the detector. Theoretically, for a parallel e-beam with infinite size that scatters from the sample, the diffraction pattern consists of delta functions. However, due to the finite coherence width of the e-beam, only a fraction of the unit cells contribute coherently to the interference pattern, resulting in Gaussian-shaped diffraction spots. Assuming a lateral coherence width (H), the resulting diffraction pattern is given by[184]

$$S \propto \sum_{\mathbf{G}} e^{-|\mathbf{k}_i^{||} - \mathbf{k}_f^{||} - \mathbf{G}|^2 H^2/2}, \tag{6.14}$$

with $\mathbf{G}$ the reciprocal surface lattice vectors, and $\mathbf{k}_i$ and $\mathbf{k}_f$ the incoming and outcoming electron momentum vector, respectively. Since we have a convergent e-beam, we also take into account the distribution of incoming electron momentum vectors. The resulting intensity within a diffraction spot follows

$$I_{\text{diff}}(k_f) = \int_{-k_i}^{k_i} f(k) e^{-(k-k_f)^2 H^2}\, dk, \tag{6.15}$$

with $k_i = k_0 \sin(\alpha)$ and $f(k)$ describing the electron density distribution within the e-beam. Typically, the brightness, the current density per unit solid angle of the source is a conserved value[24], indicating that the electron density within the e-beam is constant

$$f(k_i) = \begin{cases} 1, & |k| < k_i, \\ 0, & \text{elsewhere.} \end{cases} \tag{6.16}$$

Therefore, the diffraction spot intensity function is a convolution of a block function with a width determined by the convergent angle and Gaussian related the coherent width of the e-beam.

6.6.4. Calculation of interference in a ronchigram

In the CBED configuration sketched in Figure 6.7a, the e-beam is interacting with a bilayer with a distance d between the layers and a twist angle β. As a result, we will observe two diffraction disk patterns on the detector, originating from electrons scattered from the first and the second layer. Within the area where the diffraction disks overlap, electrons can come from either one of the layers. Therefore, we observe an interference pattern that resembles the interference from two virtual sources S^1 and S^2. The orientation of the interference fringes is always perpendicular to the vector connecting the center of the two overlapping disks.

To calculate the expected interference period, we calculate the distance between the two sources. In two layers that are stacked on top of each other without translation or rotation, the distance between the two virtual sources is[158, 176]

$$\Delta\rho = d\tan(\theta_i), \tag{6.17}$$

where θ_i is the i$^{\text{th}}$ order Bragg diffraction angle for graphene that is related to the lattice constant (a =2.46 Å) and the distance between the layers (d =3.35 Å). The distance between the virtual sources without twist angle is not large enough to create an interference pattern that is visible with the resolution of our detector[176]. The location of the virtual sources with a twist angle and defocus height (Δf) is given by (see Figure 6.7b for the schematic)

$$\begin{aligned}\rho_1 &= (\Delta f + d)\tan(\theta_i)\hat{x}\\ \rho_2 &= \Delta f \tan(\theta_i)\left(\sin(\beta)\hat{x} + \cos(\beta)\hat{y}\right).\end{aligned} \tag{6.18}$$

The resulting interference pattern at position $\mathbf{R} = (x, y, z)$ at the detector, can be calculated by summing up electron waves originating from S^1 and S^2, given by

$$I(\mathbf{R}) \propto \left| e^{ik_0|\mathbf{R}-\rho_1|} e^{-i\pi\frac{|\rho_1|^2}{\lambda\Delta f}} + e^{ik_0|\mathbf{R}-\rho_2|} e^{-i\pi\frac{|\rho_2|^2}{\lambda(\Delta f+d)}} \right|^2 \tag{6.19}$$

The resulting interference pattern depends on the under- or overfocus, the interlayer distance, and the twist angle. The larger the overfocus, underfocus or the twist angle, the larger the spacing between the virtual sources, hence the smaller the interference period. The visibility of the fringes is a combination of the ratio between the number of atomic layers in each layer within the twisted bilayer, and the lateral coherence of the e-beam. For an equal number of layers, lateral coherence is given by

$$v = \frac{I_{\max} - I_{\min}}{I_{\max}} \tag{6.20}$$

In our experiments, the visibility is approximately 20-60 %. Because any variation in the number of atomic layers contributing to the diffraction spots can only reduce the observed visibility, this value represents a lower bound for the degree of lateral coherence at the spatial frequency set by the specimen. For a bilayer of graphene, the difference between the reciprocal lattice vectors of the two layers is given by[185]

$$q_1(\beta) = 2|\mathbf{b}_i|\sin(0.5\beta), \tag{6.21}$$

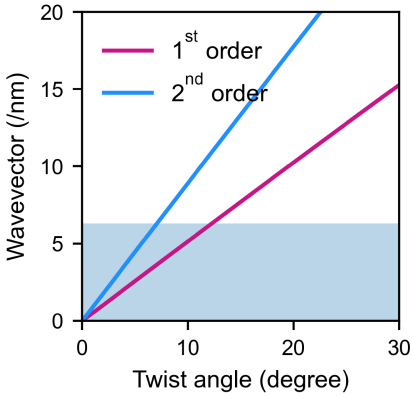

Figure 6.11: Wave vector associated with twisted bilayer of graphene. The solid lines show the relation between the twist angle and the associated wave vector for the first (purple) and second (blue) order diffraction disks of a bilayer of graphene. The accessible k-vector in the e-beam with a semi-convergent angle of 7 mrad is shown for comparison (light blue)

where $\mathbf{b}_i$ is the magnitude of the reciprocal lattice vector corresponding to diffraction order i. The spatial frequencies associated with different twist angles are shown in Figure 6.11 for both the first (purple) and second (blue) diffraction orders. The blue shaded region indicates the accessible k-vectors within the e-beam for a semi-convergence angle of 7 mrad. To probe the coherence function across the entire beam, we would need to measure twisted bilayer graphene with twist angles up to about 7 mrad. However, at such large twist angles, the diffraction disks in our SEM geometry no longer overlap, making the interference measurement impossible with the current beam configuration.

A second limitation of this method for determining the lateral coherence function is the finite resolution of the single-electron detector. Because of the limited pixel size, the smallest interference period we can reliably distinguish corresponds to a virtual-source separation of 4 nm (the accessible domain in Figure 6.9g). Since the interference period depends on both the twist angle and the defocus height above the focal plane, we retain some flexibility in choosing these parameters. Figures 6.12a,b show the calculated virtual-source separations for the first and second diffraction orders, respectively. The dashed line marks the 4 nm resolution limit. Features to the right of this line cannot be resolved with our detector. From these plots, we see that accessing higher spatial frequencies requires using larger twist angles while simultaneously reducing the defocus height, to values on the order of only ~1 µm. Repeating the measurement under these conditions would extend the measurable range of lateral coherence.

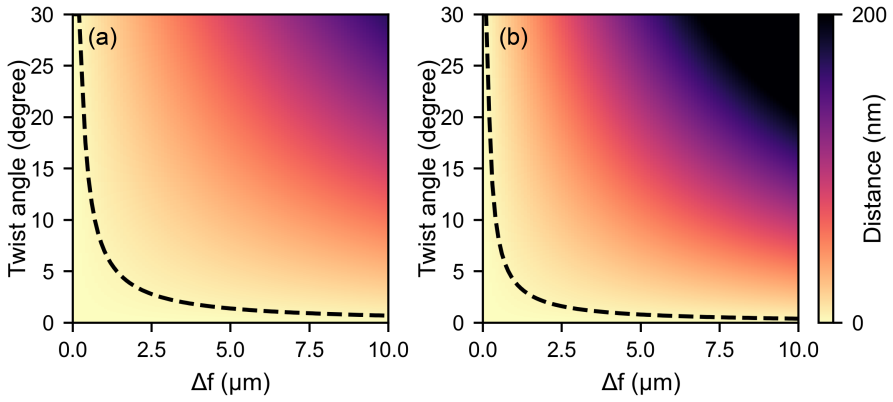

Figure 6.12: Limitation of measurements with a single-electron detector. Calculated distance between the virtual sources S^1 and S^2 for (a) the first and (b) the second order diffraction disks depending on the twist angle and defocus height (Δf). The black dashed line shows the resolution limit of 4 nm. Only features on the left of this line can be resolved by the used detector.

References

[1] L. Novotny and B. Hecht, *Principles of nano-optics* (Cambridge university press, 2012).

[2] S. A. Maier and H. A. Atwater, *Plasmonics: Localization and guiding of electromagnetic energy in metal/dielectric structures,* Journal of Applied Physics **98**, 011101 (2005).

[3] H. A. Atwater and A. Polman, *Plasmonics for improved photovoltaic devices,* Nature Materials **9**, 205 (2010).

[4] M. L. Brongersma, Y. Cui, and S. Fan, *Light management for photovoltaics using high-index nanostructures,* Nature Materials **13**, 451 (2014).

[5] E. C. Garnett, B. Ehrler, A. Polman, and E. Alarcón-Lladó, *Photonics for photovoltaics: Advances and opportunities,* ACS Photonics **8**, 61 (2021).

[6] M. L. Brongersma, N. J. Halas, and P. Nordlander, *Plasmon-induced hot carrier science and technology,* Nature Nanotechnology **10**, 25 (2015).

[7] S. Linic, P. Christopher, H. Xin, and A. Marimuthu, *Catalytic and photocatalytic transformations on metal nanoparticles with targeted geometric and plasmonic properties,* Accounts of Chemical Research **46**, 1890 (2013).

[8] S. Li, P. Miao, Y. Zhang, J. Wu, B. Zhang, Y. Du, X. Han, J. Sun, and P. Xu, *Recent advances in plasmonic nanostructures for enhanced photocatalysis and electrocatalysis,* Advanced Materials **33**, 2000086 (2021).

[9] G. Baffou and R. Quidant, *Nanoplasmonics for chemistry,* Chemical Society Reviews **43**, 3898 (2014).

[10] Y. Zhang, S. He, W. Guo, Y. Hu, J. Huang, J. R. Mulcahy, and W. D. Wei, *Surface-plasmon-driven hot electron photochemistry,* Chemical Reviews **118**, 2927 (2018).

[11] L. Thylén and L. Wosinski, *Integrated photonics in the 21st century,* Photonics Research **2**, 75 (2014).

[12] F. Zangeneh-Nejad, D. L. Sounas, A. Alù, and R. Fleury, *Analogue computing with metamaterials,* Nature Reviews Materials **6**, 207 (2021).

[13] N. Engheta, *Circuits with light at nanoscales: Optical nanocircuits inspired by metamaterials,* Science **317**, 1698 (2007).

[14] J. A. Schuller, E. S. Barnard, W. Cai, Y. C. Jun, J. S. White, and M. L. Brongersma, *Plasmonics for extreme light concentration and manipulation,* Nature Materials **9**, 193 (2010).

[15] H. T. Miyazaki and Y. Kurokawa, *Squeezing visible light waves into a 3-nm-thick and 55-nm-long plasmon cavity,* Physical Review Letters **96**, 097401 (2006).

[16] R. F. Oulton, V. J. Sorger, T. Zentgraf, R.-M. Ma, C. Gladden, L. Dai, G. Bartal, and X. Zhang, *Plasmon lasers at deep subwavelength scale,* Nature **461**, 629 (2009).

[17] S. A. Maier, P. G. Kik, H. A. Atwater, S. Meltzer, E. Harel, B. E. Koel, and A. A. Requicha, *Local detection of electromagnetic energy transport below the diffraction limit in metal nanoparticle plasmon waveguides,* Nature Materials **2**, 229 (2003).

[18] L. Novotny and N. van Hulst, *Antennas for light,* Nature Photonics **5**, 83 (2011).

[19] A. I. Kuznetsov, A. E. Miroshnichenko, M. L. Brongersma, Y. S. Kivshar, and B. Luk'yanchuk, *Optically resonant dielectric nanostructures,* Science **354**, aag2472 (2016).

[20] F. Aieta, M. A. Kats, P. Genevet, and F. Capasso, *Multiwavelength achromatic metasurfaces by dispersive phase compensation,* Science **347**, 1342 (2015).

[21] E. Ruska, *The development of the electron microscope and of electron microscopy,* Reviews of Modern Physics **59**, 627 (1987).

[22] P. E. Batson, N. Dellby, and O. L. Krivanek, *Sub-ångstrom resolution using aberration corrected electron optics,* Nature **418**, 617 (2002).

[23] M. Knoll and E. Ruska, *Das elektronenmikroskop,* Zeitschrift für Physik **78**, 318 (1932).

[24] D. B. Williams and C. B. Carter, *Transmission electron microscopy: A textbook for materials science* (Springer, 1996).

[25] F. Nagler and G. Rake, *The use of the electron microscope in diagnosis of variola, vaccinia, and varicella,* Journal of Bacteriology **55**, 45 (1948).

[26] C. Van Rooyen and G. Scott, *Smallpox diagnosis with special reference to electron microscopy,* Canadian Journal of Public Health/Revue Canadienne de Sante'e Publique **39**, 467 (1948).

[27] A. H. Zewail, *Four-dimensional electron microscopy,* Science **328**, 187 (2010).

[28] D. Cressey and E. Callaway, *Cryo-electron microscopy wins chemistry nobel,* Nature **550** (2017).

[29] C. M. Oikonomou and G. J. Jensen, *The development of cryo-EM and how it has advanced microbiology,* Nature Microbiology **2**, 1577 (2017).

[30] G. P. Thomson, *The diffraction of electrons by single crystals,* Proceedings of the Royal Society of London. Series A, Containing Papers of a Mathematical and Physical Character **133**, 1 (1931).

[31] B. J. Brenny, A. Polman, and F. J. García de Abajo, *Femtosecond plasmon and photon wave packets excited by a high-energy electron on a metal or dielectric surface,* Physical Review B **94**, 155412 (2016).

[32] M. Bosman, V. J. Keast, M. Watanabe, A. I. Maaroof, and M. B. Cortie, *Mapping surface plasmons at the nanometre scale with an electron beam,* Nanotechnology **18**, 165505 (2007).

[33] M. Kociak and O. Stéphan, *Mapping plasmons at the nanometer scale in an electron microscope,* Chemical Society Reviews **43**, 3865 (2014).

[34] J. Nelayah, M. Kociak, O. Stéphan, F. J. García de Abajo, M. Tencé, L. Henrard, D. Taverna, I. Pastoriza-Santos, L. M. Liz-Marzán, and C. Colliex, *Mapping surface plasmons on a single metallic nanoparticle,* Nature Physics **3**, 348 (2007).

[35] F. Hofer, F.-P. Schmidt, W. Grogger, and G. Kothleitner, *Fundamentals of electron energy-loss spectroscopy,* in *IOP Conference Series: Materials Science and Engineering*, Vol. 109 (IOP Publishing, 2016) p. 012007.

[36] V. Flauraud and D. T. Alexander, *STEM-EELS imaging of resonant modes in dielectric silicon nanostructures,* Microscopy and Microanalysis **25**, 634 (2019).

[37] R. Senga, K. Suenaga, P. Barone, S. Morishita, F. Mauri, and T. Pichler, *Position and momentum mapping of vibrations in graphene nanostructures,* Nature **573**, 247 (2019).

[38] F. S. Hage, R. J. Nicholls, J. R. Yates, D. G. McCulloch, T. C. Lovejoy, N. Dellby, O. L. Krivanek, K. Refson, and Q. M. Ramasse, *Nanoscale momentum-resolved vibrational spectroscopy,* Science Advances **4**, eaar7495 (2018).

[39] D. Kepaptsoglou, J. Á. Castellanos-Reyes, A. Kerrigan, J. Alves do Nascimento, P. M. Zeiger, K. El Hajraoui, J. C. Idrobo, B. G. Mendis, A. Bergman, V. Lazarov, J. Rusz, and Q. M. Ramasse, *Magnon spectroscopy in the electron microscope,* Nature **644**, 83 (2025).

[40] T. Coenen and N. M. Haegel, *Cathodoluminescence for the 21st century: Learning more from light,* Applied Physics Reviews **4**, 31103 (2017).

[41] B. Brenny, T. Coenen, and A. Polman, *Quantifying coherent and incoherent cathodoluminescence in semiconductors and metals,* Journal of Applied Physics **115** (2014).

[42] S. J. Smith and E. M. Purcell, *Visible light from localized surface charges moving across a grating,* Physical Review **92**, 1069 (1953).

[43] A. Karnieli, D. Roitman, M. Liebtrau, S. Tsesses, N. van Nielen, I. Kaminer, A. Arie, and A. Polman, *Cylindrical metalens for generation and focusing of free-electron radiation,* Nano Letters **22**, 5641 (2022).

[44] Z. Sun, L. Cao, L. Wang, W. Wu, H. Yang, J. Wang, W. Luo, M. Ren, W. Cai, and J. Xu, *Smith-purcell radiation in two dimensions,* Physical Review Letters **134**, 043802 (2025).

[45] F. J. García de Abajo, A. Polman, C. I. Velasco, M. Kociak, L. H. G. Tizei, O. Stéphan, S. Meuret, T. Sannomiya, K. Akiba, Y. Auad, A. Feist, C. Ropers, P. Baum, J. H. Gaida, M. Sivis, H. Lourenço-Martins, L. Serafini, J. Verbeeck, A. Konečná, N. Talebi, B. M. Ferrari, C. J. R. Duncan, M. G. Bravi, I. Ostroman, G. M. Vanacore, E. Nussinson, R. Ruimy, Y. Adiv, A. Niedermayr, I. Kaminer, V. Di Giulio, O. Kfir, Z. Zhao, R. Shiloh, Y. Morimoto, M. Kozák, P. Hommelhoff, F. Barantani, F. Carbone, F. Chahshouri, W. Albrecht, S. Rey, T. Coenen, E. Kieft, H. L. Lalandec Robert, F. de Jong, and M. Solà-Garcia, *Roadmap for quantum nanophotonics with free electrons,* ACS Photonics **12**, 4760 (2025).

[46] B. Barwick, D. J. Flannigan, and A. H. Zewail, *Photon-induced near-field electron microscopy,* Nature **462**, 902 (2009).

[47] A. Feist, K. E. Echternkamp, J. Schauss, S. V. Yalunin, S. Schäfer, and C. Ropers, *Quantum coherent optical phase modulation in an ultrafast transmission electron microscope,* Nature **521**, 200 (2015).

[48] S. T. Park, M. Lin, and A. H. Zewail, *Photon-induced near-field electron microscopy (PINEM): Theoretical and experimental,* New Journal of Physics **12**, 123028 (2010).

[49] F. J. García de Abajo, A. Asenjo-Garcia, and M. Kociak, *Multiphoton absorption and emission by interaction of swift electrons with evanescent light fields,* Nano Letters **10**, 1859 (2010).

[50] A. Ryabov, J. W. Thurner, D. Nabben, M. V. Tsarev, and P. Baum, *Attosecond metrology in a continuous-beam transmission electron microscope,* Science Advances **6**, eabb1393 (2020).

[51] K. E. Priebe, C. Rathje, S. V. Yalunin, T. Hohage, A. Feist, S. Schäfer, and C. Ropers, *Attosecond electron pulse trains and quantum state reconstruction in ultrafast transmission electron microscopy,* Nature Photonics **11**, 793 (2017).

[52] I. Madan, V. Leccese, A. Mazur, F. Barantani, T. LaGrange, A. Sapozhnik, P. M. Tengdin, S. Gargiulo, E. Rotunno, J.-C. Olaya, I. Kaminer, V. Grillo, F. J. García de Abajo, F. Carbone, and G. M. Vanacore, *Ultrafast transverse modulation of free electrons by interaction with shaped optical fields,* ACS Photonics **9**, 3215 (2022).

[53] R. Shiloh, N. Schönenberger, Y. Adiv, R. Ruimy, A. Karnieli, T. Hughes, R. J. England, K. J. Leedle, D. S. Black, Z. Zhao, P. Musumeci, R. L. Byer, A. Arie, I. Kaminer, and P. Hommelhoff, *Miniature light-driven nanophotonic electron acceleration and control,* Advances in Optics and Photonics **14**, 862 (2022).

[54] J. Breuer and P. Hommelhoff, *Laser-based acceleration of nonrelativistic electrons at a dielectric structure,* Physical Review Letters **111**, 134803 (2013).

[55] M. C. Chirita Mihaila and M. Kozák, *Design for light-based spherical aberration correction of ultrafast electron microscopes,* Optics Express **33**, 758 (2025).

[56] A. Konečná and F. J. García de Abajo, *Electron beam aberration correction using optical near fields,* Physical Review Letters **125**, 030801 (2020).

[57] J. H. Gaida, H. Lourenço-Martins, S. V. Yalunin, A. Feist, M. Sivis, T. Hohage, F. J. García de Abajo, and C. Ropers, *Lorentz microscopy of optical fields,* Nature Communications **14**, 6545 (2023).

[58] D. Nabben, J. Kuttruff, L. Stolz, A. Ryabov, and P. Baum, *Attosecond electron microscopy of sub-cycle optical dynamics,* Nature **619**, 63 (2023).

[59] F. J. García de Abajo and V. Di Giulio, *Optical excitations with electron beams: Challenges and opportunities,* ACS Photonics **8**, 945 (2021).

[60] V. Di Giulio and F. J. García de Abajo, *Free-electron shaping using quantum light,* Optica **7**, 1820 (2020).

[61] A. Konecna, V. Di Giulio, V. Mkhitaryan, C. Ropers, and F. J. García de Abajo, *Nanoscale nonlinear spectroscopy with electron beams,* ACS Photonics **7**, 1290 (2020).

[62] P. Kruit, H. Shuman, and A. Somlyo, *Detection of X-rays and electron energy loss events in time coincidence,* Ultramicroscopy **13**, 205 (1984).

[63] R. Graham, J. Spence, and H. Alexander, *Infrared cathodoluminescence studies from dislocations in silicon in tem, a Fourier transform spectrometer for CL in TEM and ELS/CL coincidence measurements of lifetimes in semiconductors,* MRS Online Proceedings Library **82**, 235 (1986).

[64] D. Jannis, K. Müller-Caspary, A. Béché, A. Oelsner, and J. Verbeeck, *Spectroscopic coincidence experiments in transmission electron microscopy,* Applied Physics Letters **114**, 143101 (2019).

[65] N. Varkentina, Y. Auad, S. Y. Woo, A. Zobelli, L. Bocher, J.-D. Blazit, X. Li, M. Tencé, K. Watanabe, T. Taniguchi, O. Stéphan, M. Kociak, and L. H. G. Tizei, *Cathodoluminescence excitation spectroscopy: Nanoscale imaging of excitation pathways,* Science Advances **8**, eabq4947 (2022).

[66] N. Varkentina, Y. Auad, S. Y. Woo, F. Castioni, J.-D. Blazit, M. Tencé, H.-C. Chang, J. Chen, K. Watanabe, T. Taniguchi, M. Kociak, and L. H. G. Tizei, *Excitation lifetime extracted from electron–photon (EELS-CL) nanosecond-scale temporal coincidences,* Applied Physics Letters **123**, 223502 (2023).

[67] E. Kazakevich, H. Aharon, and O. Kfir, *Spatial electron-photon entanglement,* Physical Review Research **6**, 043033 (2024).

[68] J.-W. Henke, H. Jeng, and C. Ropers, *Probing electron-photon entanglement using a quantum eraser,* Physical Review A **111**, 012610 (2025).

[69] S. Frabboni, G. C. Gazzadi, and G. Pozzi, *Ion and electron beam nanofabrication of the which-way double-slit experiment in a transmission electron microscope,* Applied Physics Letters **97**, 263101 (2010).

[70] R. Ruimy, O. Tziperman, A. Gorlach, K. Mølmer, and I. Kaminer, *Many-body entanglement via 'which-path' information,* npj Quantum Information **10**, 121 (2024).

[71] J.-W. Henke, H. Jeng, M. Sivis, and C. Ropers, *Observation of quantum entanglement between free electrons and photons,* arXiv:2504.13047 (2025).

[72] S. Bogdanov, A. Preimesberger, H. Mishra, D. Hornof, T. Spielauer, F. Thajer, M. Maurer, P. Falb, L. Stöger, T. Schachinger, F. Bleicher, M. S. Seifner, I. C. Bicket, and P. Haslinger, *Ghost imaging with free electron-photon pairs,* arXiv:2509.14950 (2025).

[73] T. Coenen, S. V. den Hoedt, and A. Polman, *A new cathodoluminescence system for nanoscale optics, materials science, and geology,* Microscopy Today **24**, 12 (2016).

[74] U. Bansal, A. Sharma, B. Putz, C. Kirchlechner, and S. Lee, *Data-efficient 4D-STEM in SEM: Beyond 2D materials to metallic materials,* Ultramicroscopy , 114203 (2025).

[75] B. W. Caplins, J. D. Holm, and R. R. Keller, *Developing a programmable STEM detector for the scanning electron microscope,* Microscopy and Microanalysis **24**, 658 (2018).

[76] R. Egerton, P. Li, and M. Malac, *Radiation damage in the TEM and SEM,* Micron **35**, 399 (2004).

[77] J. van de Groep and A. Polman, *Designing dielectric resonators on substrates: Combining magnetic and electric resonances,* Optics Express **21**, 26285 (2013).

[78] N. J. Schilder, H. Agrawal, E. C. Garnett, and A. Polman, *Phase-resolved surface plasmon scattering probed by cathodoluminescence holography,* ACS Photonics **7**, 1476 (2020).

[79] Y. Li and J. Z. Zhang, *Hydrogen generation from photoelectrochemical water splitting based on nanomaterials,* Laser and Photonics Reviews **4**, 517 (2010).

[80] M. A. Butt, B. Janaszek, and R. Piramidowicz, *Lighting the way forward: The bright future of photonic integrated circuits,* Sensors International **6**, 100326 (2025).

[81] A. F. Koenderink, A. Alù, and A. Polman, *Nanophotonics: Shrinking light-based technology,* Science **348**, 516 (2015).

[82] J. Schefold, S. Meuret, N. Schilder, T. Coenen, H. Agrawal, E. C. Garnett, and A. Polman, *Spatial resolution of coherent cathodoluminescence super-resolution microscopy,* ACS Photonics **6**, 1067 (2019).

[83] M. Liebtrau, M. Sivis, A. Feist, H. Lourenço-Martins, N. Pazos-Pérez, R. A. Alvarez-Puebla, F. J. García de Abajo, A. Polman, and C. Ropers, *Spontaneous and stimulated electron–photon interactions in nanoscale plasmonic near fields,* Light: Science & Applications **10**, 82 (2021).

[84] A. Polman, M. Kociak, and F. J. García de Abajo, *Electron-beam spectroscopy for nanophotonics,* Nature Materials **18**, 1158 (2019).

[85] F. J. García de Abajo, *Optical excitations in electron microscopy,* Reviews of Modern Physics **82**, 209 (2010).

[86] M. Kociak and L. F. Zagonel, *Cathodoluminescence in the scanning transmission electron microscope,* Ultramicroscopy **174**, 50 (2017).

[87] M. C. C. Mihaila, P. Weber, M. Schneller, L. Grandits, S. Nimmrichter, and T. Juffmann, *Transverse electron-beam shaping with light,* Physical Review X **12**, 31043 (2022).

[88] E. J. R. Vesseur, R. D. Waele, M. Kuttge, and A. Polman, *Direct observation of plasmonic modes in Au nanowires using high-resolution cathodoluminescence spectroscopy,* Nano Letters **7**, 2843 (2007).

[89] R. Sapienza, T. Coenen, J. Renger, M. Kuttge, N. F. van Hulst, and A. Polman, *Deep-subwavelength imaging of the modal dispersion of light,* Nature Materials **11**, 781 (2012).

[90] K. Wang, R. Dahan, M. Shentcis, Y. Kauffmann, A. B. Hayun, O. Reinhardt, S. Tsesses, and I. Kaminer, *Coherent interaction between free electrons and a photonic cavity,* Nature **582**, 50 (2020).

[91] W. Albrecht and S. Bals, *Fast electron tomography for nanomaterials,* Journal of Physical Chemistry C **124**, 27276 (2020).

[92] O. Nicoletti, F. de La Peña, R. K. Leary, D. J. Holland, C. Ducati, and P. A. Midgley, *Three-dimensional imaging of localized surface plasmon resonances of metal nanoparticles,* Nature **502**, 80 (2013).

[93] A. C. Atre, B. J. M. Brenny, T. Coenen, A. García-Etxarri, A. Polman, and J. A. Dionne, *Nanoscale optical tomography with cathodoluminescence spectroscopy,* Nature Nanotechnology **10**, 429 (2015).

[94] U. Hohenester, *Simulating electron energy loss spectroscopy with the MNPBEM toolbox,* Computer Physics Communications **185**, 1177 (2014).

[95] F. J. García de Abajo and A. Howie, *Retarded field calculation of electron energy loss in inhomogeneous dielectrics,* Physical Review B - Condensed Matter and Materials Physics **65**, 1154181 (2002).

[96] A. Asenjo-Garcia and F. J. García de Abajo, *Plasmon electron energy-gain spectroscopy,* New Journal of Physics **15**, 103021 (2013).

[97] V. Di Giulio, M. Kociak, and F. J. García de Abajo, *Probing quantum optical excitations with fast electrons,* Optica **6**, 1524 (2019).

[98] U. Hohenester and A. Trügler, *MNPBEM - A matlab toolbox for the simulation of plasmonic nanoparticles,* Computer Physics Communications **183**, 370 (2012).

[99] D. Drouin, A. R. Couture, D. Joly, X. Tastet, V. Aimez, and R. Gauvin, *CASINO V2.42 - A fast and easy-to-use modeling tool for scanning electron microscopy and microanalysis users,* Scanning **29**, 92 (2007).

[100] A. Feist, G. Huang, G. Arend, Y. Yang, J.-W. Henke, A. S. Raja, F. J. Kappert, R. N. Wang, H. Lourenço-Martins, Z. Qiu, J. Liu, O. Kfir, T. J. Kippenberg, and C. Ropers, *Cavity-mediated electron-photon pairs,* Science **377**, 777 (2022).

[101] V. Di Giulio, E. Akerboom, A. Polman, and F. J. García de Abajo, *Toward optimum coupling between free electrons and confined optical modes,* ACS Nano **18**, 14255 (2024).

[102] R. L. Olmon, B. Slovick, T. W. Johnson, D. Shelton, S.-H. Oh, G. D. Boreman, and M. B. Raschke, *Optical dielectric function of gold,* Physical Review B **86**, 235147 (2012).

[103] A. Patoux, C. Majorel, P. R. Wiecha, A. Cuche, O. L. Muskens, C. Girard, and A. Arbouet, *Polarizabilities of complex individual dielectric or plasmonic nanostructures,* Physical Review B **101**, 235418 (2020).

[104] G. Lozano, S. R. K. Rodriguez, M. A. Verschuuren, and J. Gómez Rivas, *Metallic nanostructures for efficient LED lighting,* Light: Science and Applications **5**, e16080 (2016).

[105] A. E. Krasnok, A. E. Miroshnichenko, P. A. Belov, and Y. S. Kivshar, *All-dielectric optical nanoantennas,* AIP Conference Proceedings **1475**, 22 (2012).

[106] A. G. Curto, G. Volpe, T. H. Taminiau, M. P. Kreuzer, R. Quidant, and N. F. van Hulst, *Unidirectional emission of a quantum dot coupled to a nanoantenna,* Science **329**, 930 (2010).

[107] T. Coenen, E. J. R. Vesseur, A. Polman, and A. F. Koenderink, *Directional emission from plasmonic Yagi-Uda antennas probed by angle-resolved cathodoluminescence spectroscopy,* Nano Letters **11**, 3779 (2011).

[108] T. Coenen, J. van de Groep, and A. Polman, *Resonant modes of single silicon nanocavities excited by electron irradiation,* ACS nano **7**, 1689 (2013).

[109] J. Xu, Y. Wu, P. Zhang, Y. Wu, R. A. L. Vallée, S. Wu, and X. Liu, *Resonant scattering manipulation of dielectric nanoparticles,* Advanced Optical Materials **9**, 2100112 (2021).

[110] A. B. Evlyukhin, C. Reinhardt, A. Seidel, B. S. Luk'Yanchuk, and B. N. Chichkov, *Optical response features of Si-nanoparticle arrays,* Physical Review B - Condensed Matter and Materials Physics **82**, 1 (2010).

[111] C. Kittel and P. McEuen, *Introduction to solid state physics* (John Wiley & Sons, 2018).

[112] M. Kerker, D. S. Wang, and C. L. Giles, *Electromagnetic scattering by magnetic spheres.* Journal of the Optical Society of America **73**, 765 (1983).

[113] N. Yamamoto, K. Araya, and F. J. García de Abajo, *Photon emission from silver particles induced by a high-energy electron beam,* Physics Review B **64**, 205419 (2001).

[114] T. Matsukata, N. Matthaiakakis, T. A. Yano, M. Hada, T. Tanaka, N. Yamamoto, and T. Sannomiya, *Selection and visualization of degenerate magnetic and electric multipoles up to radial higher orders by cathodoluminescence,* ACS Photonics **6**, 2320 (2019).

[115] S. Fiedler, P. E. Stamatopoulou, A. Assadillayev, C. Wolff, H. Sugimoto, M. Fujii, N. A. Mortensen, S. Raza, and C. Tserkezis, *Disentangling cathodoluminescence spectra in nanophotonics: Particle eigenmodes vs transition radiation,* Nano Letters **22**, 2320 (2022).

[116] E. Akerboom, V. Di Giulio, N. J. Schilder, F. J. García de Abajo, and A. Polman, *Free electron-plasmon coupling strength and near-field retrieval through electron energy-dependent cathodoluminescence spectroscopy,* ACS Nano **18**, 13560 (2024).

[117] C. F. Bohren and D. R. Huffman, *Absorption and scattering of light by small particles* (John Wiley & Sons, 2008).

[118] M. A. Green and M. J. Keevers, *Optical properties of intrinsic silicon at 300 k,* Progress in Photovoltaics: Research and applications **3**, 189 (1995).

[119] P. E. Stamatopoulou, W. Zhao, A. Rodríguez Echarri, N. A. Mortensen, K. Busch, C. Tserkezis, and C. Wolff, *Electron beams traversing spherical nanoparticles: Analytic and numerical treatment,* Physical Review Research **6**, 013239 (2024).

[120] H. Sugimoto, T. Okazaki, and M. Fujii, *Mie resonator color inks of monodispersed and perfectly spherical crystalline silicon nanoparticles,* Advanced Optical Materials **8**, 2000033 (2020).

[121] L. H. G. Tizei, H. Lourenço-Martins, P. Das, S. Y. Woo, L. Scarabelli, C. Hanske, L. M. Liz-Marzán, K. Watanabe, T. Taniguchi, and M. Kociak, *Monolayer and thin h–BN as substrates for electron spectro-microscopy analysis of plasmonic nanoparticles,* Applied Physics Letters **113**, 231108 (2018).

[122] Z. Thollar, C. Wadell, T. Matsukata, N. Yamamoto, and T. Sannomiya, *Three-dimensional multipole rotation in spherical silver nanoparticles observed by cathodoluminescence,* ACS Photonics **5**, 2555 (2018).

[123] F. Qin, Z. Zhang, K. Zheng, Y. Xu, S. Fu, Y. Wang, and Y. Qin, *Transverse Kerker effect for dipole sources,* Physical Review Letters **128**, 38 (2022).

[124] T. Matsukata, C. Wadell, N. Matthaiakakis, N. Yamamoto, and T. Sannomiya, *Selected mode mixing and interference visualized within a single optical nanoantenna,* ACS Photonics **5**, 4986 (2018).

[125] A. J. den Boef, *Optical wafer metrology sensors for process-robust cd and overlay control in semiconductor device manufacturing,* Surface Topography: Metrology and Properties **4**, 023001 (2016).

[126] C. Zuo, J. Qian, S. Feng, W. Yin, Y. Li, P. Fan, J. Han, K. Qian, and Q. Chen, *Deep learning in optical metrology: a review,* Light: Science & Applications **11**, 39 (2022).

[127] A. I. Kuznetsov, M. L. Brongersma, J. Yao, M. K. Chen, U. Levy, D. P. Tsai, N. I. Zheludev, A. Faraon, A. Arbabi, N. Yu, D. Chanda, K. B. Crozier, A. V. Kildishev, H. Wang, J. K. Yang, J. G. Valentine, P. Genevet, J. A. Fan, O. D. Miller, A. Majumdar, J. E. Fröch, D. Brady, F. Heide, A. Veeraraghavan, N. Engheta, A. Alù, A. Polman, H. A. Atwater, P. Thureja, R. Paniagua-Dominguez, S. T. Ha, A. I. Barreda, J. A. Schuller, I. Staude, G. Grinblat, Y. Kivshar, S. Peana, S. F. Yelin, A. Senichev, V. M. Shalaev, S. Saha, A. Boltasseva, J. Rho, D. K. Oh, J. Kim, J. Park, R. Devlin, and R. A. Pala, *Roadmap for optical metasurfaces,* ACS Photonics **11**, 816 (2024).

[128] P. A. Midgley and R. E. Dunin-Borkowski, *Electron tomography and holography in materials science,* Nature Materials **8**, 271 (2009).

[129] A. Borzunov, V. Karaulov, N. Koshev, D. Lukyanenko, E. Rau, A. Yagola, and S. Zaitsev, *3D surface topography imaging in SEM with improved backscattered electron detector: Arrangement and reconstruction algorithm,* Ultramicroscopy **207**, 112830 (2019).

[130] N. Talebi, S. Meuret, S. Guo, M. Hentschel, A. Polman, H. Giessen, and P. A. van Aken, *Merging transformation optics with electron-driven photon sources,* Nature Communications **10**, 599 (2019).

[131] C. I. Osorio, T. Coenen, B. J. Brenny, A. Polman, and A. F. Koenderink, *Angle-resolved cathodoluminescence imaging polarimetry,* ACS Photonics **3**, 147 (2016).

[132] N. van Nielen, M. Hentschel, N. Schilder, H. Giessen, A. Polman, and N. Talebi, *Electrons generate self-complementary broadband vortex light beams using chiral photon sieves,* Nano Letters **20**, 5975 (2020).

[133] S. Tsesses, G. Bartal, and I. Kaminer, *Light generation via quantum interaction of electrons with periodic nanostructures,* Physical Review A **95**, 013832 (2017).

[134] N. Yamamoto, F. J. García de Abajo, and V. Myroshnychenko, *Interference of surface plasmons and Smith-Purcell emission probed by angle-resolved cathodoluminescence spectroscopy,* Physical Review B **91**, 125144 (2015).

[135] M. Taleb, M. Hentschel, K. Rossnagel, H. Giessen, and N. Talebi, *Phase-locked photon–electron interaction without a laser,* Nature Physics **19**, 869 (2023).

[136] M. Taleb, P. Bittorf, M. Black, M. Hentschel, W. Sigle, B. Haas, C. Koch, P. A. van Aken, H. Giessen, and N. Talebi, *Ultrafast phonon-mediated dephasing of color centers in hexagonal boron nitride probed by electron beams,* Nature Communications **16**, 2326 (2025).

[137] T. Soler, E. Akerboom, P. E. Stamatopoulou, H. Sugimoto, M. Fujii, S. Fiedler, and A. Polman, *Electron-energy dependent excitation and directional far-field radiation of resonant Mie modes in single Si nanospheres,* ACS Photonics **12**, 4161 (2025).

[138] T. Coenen and A. Polman, *Polarization-sensitive cathodoluminescence Fourier microscopy,* Optics Express **20**, 18679 (2012).

[139] T. Coenen, E. J. R. Vesseur, and A. Polman, *Angle-resolved cathodoluminescence spectroscopy,* Applied Physics Letters **99** (2011).

[140] N. Pazos-Perez, L. Guerrini, and R. A. Alvarez-Puebla, *Plasmon tunability of gold nanostars at the tip apexes,* ACS Omega **3**, 17173 (2018).

[141] E. Nogales, *The development of cryo-EM into a mainstream structural biology technique,* Nature Methods **13**, 24 (2016).

[142] U. J. Lorenz, *Microsecond time-resolved cryo-electron microscopy,* Current Opinion in Structural Biology **87**, 102840 (2024).

[143] R. Henderson, *Overview and future of single particle electron cryomicroscopy,* Archives of biochemistry and biophysics **581**, 19 (2015).

[144] U. J. Lorenz and A. H. Zewail, *Biomechanics of DNA structures visualized by 4D electron microscopy,* Proceedings of the National Academy of Sciences of the United States of America **110**, 2822 (2013).

[145] M. Adrian, J. Dubochet, J. Lepault, and A. W. McDowall, *Cryo-electron microscopy of viruses,* Nature **308**, 32 (1984).

[146] K. Harvey and G. Edwards, *Using benchtop scanning electron microscopy as a valuable imaging tool in various applications,* Microscopy Today **30**, 32 (2022).

[147] S. Nasrazadani and S. Hassani, *Chapter 2 - modern analytical techniques in failure analysis of aerospace, chemical, and oil and gas industries,* in *Handbook of Materials Failure Analysis with Case Studies from the Oil and Gas Industry*, edited by A. S. H. Makhlouf and M. Aliofkhazraei (Butterworth-Heinemann, 2016) pp. 39–54.

[148] M. Liebtrau and A. Polman, *Angular dispersion of free-electron-light coupling in an optical fiber-integrated metagrating,* ACS Photonics **11**, 1125 (2024).

[149] A. Konečná, F. Iyikanat, and F. J. García de Abajo, *Entangling free electrons and optical excitations,* Science Advances **8**, eabo7853 (2022).

[150] R. Remez, A. Karnieli, S. Trajtenberg-Mills, N. Shapira, I. Kaminer, Y. Lereah, and A. Arie, *Observing the quantum wave nature of free electrons through spontaneous emission,* Physical review letters **123**, 060401 (2019).

[151] E. Akerboom, H. Sugimoto, M. Fujii, F. J. García de Abajo, and A. Polman, *Angle-resolved cathodoluminescence interferometry of plasmonic and dielectric scatterers,* Nano Letters **25**, 14264 (2025).

[152] S. Kamal and R. K. Hailstone, *SEM Nano: An electron wave optical simulation for the scanning electron microscope,* Microscopy and Microanalysis **28**, 441 (2022).

[153] D. C. Joy, Y.-U. Ko, and J. J. Hwu, *Metrics of resolution and performance for CD-SEMs,* in *Metrology, Inspection, and Process Control for Microlithography XIV*, Vol. 3998 (SPIE, 2000) pp. 108–114.

[154] S. Meuret, M. Solà Garcia, T. Coenen, E. Kieft, H. Zeijlemaker, M. Lätzel, S. Christiansen, S. Woo, Y. Ra, Z. Mi, and A. Polman, *Complementary cathodoluminescence lifetime imaging configurations in a scanning electron microscope,* Ultramicroscopy **197**, 28 (2019).

[155] C. Ophus, *Four-dimensional scanning transmission electron microscopy (4D-STEM): From scanning nanodiffraction to ptychography and beyond,* Microscopy and Microanalysis **25**, 563 (2019).

[156] A. J. Wilkinson and T. B. Britton, *Strains, planes, and EBSD in materials science,* Materials Today **15**, 366 (2012).

[157] P. Denninger, P. Schweizer, and E. Spiecker, *Characterization of extended defects in 2D materials using aperture-based dark-field STEM in SEM,* Micron **186**, 103703 (2024).

[158] T. Latychevskaia, C. R. Woods, Y. B. Wang, M. Holwill, E. Prestat, S. J. Haigh, and K. S. Novoselov, *Convergent beam electron diffraction of multilayer van der Waals structures,* Ultramicroscopy **212**, 112976 (2020).

[159] T. Latychevskaia, C. Escher, and H.-W. Fink, *Moiré structures in twisted bilayer graphene studied by transmission electron microscopy,* Ultramicroscopy **197**, 46 (2019).

[160] B. W. Caplins, J. D. Holm, R. M. White, and R. R. Keller, *Orientation mapping of graphene using 4D STEM-in-SEM,* Ultramicroscopy **219**, 113137 (2020).

[161] P. Schweizer, P. Denninger, C. Dolle, and E. Spiecker, *Low energy nano diffraction (LEND)–a versatile diffraction technique in sem,* Ultramicroscopy **213**, 112956 (2020).

[162] C. B. Carter and D. B. Williams, *Transmission electron microscopy: Diffraction, imaging, and spectrometry* (Springer, 2016).

[163] M. D. Zotta, M. C. Nevins, R. K. Hailstone, and E. Lifshin, *The determination and application of the point spread function in the scanning electron microscope,* Microscopy and Microanalysis **24**, 396 (2018).

[164] M. Liebtrau, *Shaping the interplay of free electrons and light with optical metasurfaces*, Ph.D. thesis, University of Amsterdam (2023).

[165] M. Solà Garcia, *Electron-matter interaction probed with time-resolved cathodoluminescence*, Ph.D. thesis, University of Amsterdam (2021).

[166] C. Maunders, C. Dwyer, P. Tiemeijer, and J. Etheridge, *Practical methods for the measurement of spatial coherence—a comparative study,* Ultramicroscopy **111**, 1437 (2011).

[167] H. Sawada, T. Sannomiya, F. Hosokawa, T. Nakamichi, T. Kaneyama, T. Tomita, Y. Kondo, T. Tanaka, Y. Oshima, Y. Tanishiro, and K. Takayanagi, *Measurement method of aberration from ronchigram by autocorrelation function,* Ultramicroscopy **108**, 1467 (2008).

[168] J. Yamasaki, Y. Shimaoka, and H. Sasaki, *Precise method for measuring spatial coherence in TEM beams using Airy diffraction patterns,* Microscopy **67**, 1 (2018).

[169] S. Morishita, J. Yamasaki, and N. Tanaka, *Measurement of spatial coherence of electron beams by using a small selected-area aperture,* Ultramicroscopy **129**, 10 (2013).

[170] S. Hatanaka and J. Yamasaki, *Precise measurement of spatial coherence and axial brightness based on the wigner function reconstruction in transmission electron microscopes with field emission guns and a thermionic emission gun,* Microscopy **74**, 20 (2025).

[171] C. Dwyer, R. Erni, and J. Etheridge, *Method to measure spatial coherence of subangstrom electron beams,* Applied Physics Letters **93** (2008).

[172] C. Dwyer, R. Erni, and J. Etheridge, *Measurement of effective source distribution and its importance for quantitative interpretation of stem images,* Ultramicroscopy **110**, 952 (2010).

[173] R. A. Herring, *Electron beam coherence measurements using diffracted beam interferometry/holography,* Journal of Electron Microscopy **58**, 213 (2009).

[174] O. Svelto, S. Longhi, G. Della Valle, G. Huber, S. Kück, M. Pollnau, H. Hillmer, T. Kusserow, R. Engelbrecht, F. Rohlfing, J. Kaiser, R. Malz, G. Marowsky, K. Mann, P. Simon, C. K. Rhodes, F. J. Duarte, A. Borsutzky, J. A. L'huillier, M. W. Sigrist, H. Wächter, E. Saldin, E. Schneidmiller, M. Yurkov, R. Sauerbrey, J. Hein, M. Gianella, J. Helmcke, K. Midorikawa, F. Riehle, S. Steinberg, and H. Brand, *Springer Handbook of Lasers and Optics*, edited by F. Träger (Springer Berlin Heidelberg, Berlin, Heidelberg, 2012) pp. 641–1046.

[175] F. Kiani and G. Tagliabue, *High aspect ratio Au microflakes via gap-assisted synthesis,* Chemistry of Materials **34**, 1278 (2022).

[176] T. Latychevskaia, C. R. Woods, Y. B. Wang, M. Holwill, E. Prestat, S. J. Haigh, and K. S. Novoselov, *Convergent beam electron holography for analysis of van der Waals heterostructures,* Proceedings of the National Academy of Sciences **115**, 7473 (2018).

[177] M. Van Winkle, I. M. Craig, S. Carr, M. Dandu, K. C. Bustillo, J. Ciston, C. Ophus, T. Taniguchi, K. Watanabe, A. Raja, *et al.*, *Rotational and dilational reconstruction in transition metal dichalcogenide Moiré bilayers,* Nature Communications **14**, 2989 (2023).

[178] I. M. Craig, M. Van Winkle, C. Groschner, K. Zhang, N. Dowlatshahi, Z. Zhu, T. Taniguchi, K. Watanabe, S. M. Griffin, and D. K. Bediako, *Local atomic stacking and symmetry in twisted graphene trilayers,* Nature Materials **23**, 323 (2024).

[179] T. Latychevskaia, Y. Zou, C. R. Woods, Y. B. Wang, M. Holwill, E. Prestat, S. J. Haigh, and K. S. Novoselov, *Holographic reconstruction of the interlayer distance of bilayer two-dimensional crystal samples from their convergent beam electron diffraction patterns,* Ultramicroscopy **219**, 113020 (2020).

[180] K. Zhang and E. B. Tadmor, *Structural and electron diffraction scaling of twisted graphene bilayers,* Journal of the Mechanics and Physics of Solids **112**, 225 (2018).

[181] M. J. Zachman, J. Madsen, X. Zhang, P. M. Ajayan, T. Susi, and M. Chi, *Interferometric 4D-STEM for lattice distortion and interlayer spacing measurements of bilayer and trilayer 2D materials,* Small **17**, 2100388 (2021).

[182] N. P. Kazmierczak, M. Van Winkle, C. Ophus, K. C. Bustillo, S. Carr, H. G. Brown, J. Ciston, T. Taniguchi, K. Watanabe, and D. K. Bediako, *Strain fields in twisted bilayer graphene,* Nature Materials **20**, 956 (2021).

[183] M. Abramowitz and I. A. Stegun, *Handbook of mathematical functions: with formulas, graphs, and mathematical tables*, Vol. 55 (Courier Corporation, 1965).

[184] F. J. García de Abajo, M. Van Hove, and C. Fadley, *Multiple scattering of electrons in solids and molecules: A cluster-model approach,* Physical review B **63**, 075404 (2001).

[185] T. Dierke, S. Wolff, R. Gillen, J. Eisenkolb, T. Nagel, S. Maier, M. Kivala, F. Hauke, A. Hirsch, and J. Maultzsch, *Moiré lattice of twisted bilayer graphene as template for non-covalent functionalization,* Angewandte Chemie **137**, e202414593 (2025).

List of publications

This thesis is based on the following publications.

1. E. Akerboom, V. Di Giulio, N. J. Schilder, F. J. García de Abajo, and A. Polman, *Free electron-plasmon coupling strength and near-field retrieval through electron energy-dependent cathodoluminescence spectroscopy*, ACS Nano **18**, 13560 (2024). **Chapter 2**

2. T. Soler*, E. Akerboom*, P. E. Stamatopoulou, H. Sugimoto, M. Fujii, S. Fiedler, and A. Polman, *Electron-energy dependent excitation and directional far-field radiation of resonant Mie modes in single Si nanospheres*, ACS Photonics **12**, 4161 (2025). **Chapter 3**

3. E. Akerboom, H. Sugimoto, M. Fujii, F. J. García de Abajo, and A. Polman, *Angle-resolved cathodoluminescence interferometry of plasmonic and dielectric scatterers*, Nano Letters **25**, 14264 (2025). **Chapter 4**

4. E. Akerboom, H. Sugimoto, M. Fujii, N. Perez, R. Álvarez Puebla, F. Koenderink, F. J. García de Abajo, and A. Polman, *Revealing time characteristics of dielectric and plasmonic structures through cathodoluminescence interferometry*, **Chapter 4**
in preparation

5. E. Akerboom, N. J. Schilder, F. J. García de Abajo, A. Polman, *Studying electron beam coherence using plasmon interference*, **Chapter 5**
in preparation

6. E. Akerboom, F. Kiani, G. Tagliabue, W. Albrecht, J. Etheridge, F. J. García de Abajo, A. Polman, *Electron lateral coherence length in the scanning electron microscope studied with electron diffraction*, **Chapter 6**
in preparation

Other publications

1. E. Akerboom*, T. Veeken*, C. Hecker, J. van de Groep, and A. Polman, *Passive radiative cooling of silicon solar Modules with photonic silica microcylinders*, ACS Photonics **9**, 3831 (2022).

2. V. Di Giulio, E. Akerboom, A. Polman, and F. J. García de Abajo, *Toward optimum coupling between free electrons and confined optical modes*, ACS Nano **18**, 14255 (2024).

3. D. Dede*, E. Akerboom*, R. Brondolin, T. Veeken, T. Hagger, R. Lamerle, E. Alarcon Llado, V. Piazza, W. C. Carter, A. Polman, and A. Fontcuberta i Morral, *Selective-area deposition of indium and its plasmonic properties*, ACS Applied Optical Materials, DOI: 10.1021/acsaom.5c00373 (2025).

* equal contributions

Author contributions

Chapter 2

Evelijn Akerboom fabricated the samples, performed the CL measurements and the BEM simulations, and did the data analysis. *Evelijn Akerboom, Valerio Di Giulio*, and *Nick Schilder* interpreted the data, and *Valerio Di Giulio* and *F. Javier García de Abajo* developed the theory. *Albert Polman* supervised the project. *Evelijn Akerboom* and *Albert Polman* wrote the original draft and *Valerio Di Giulio, Nick Schilder* and *F. Javier García de Abajo* reviewed and co-edited the chapter.

Chapter 3

Evelijn Akerboom, Saskia Fiedler, and *Albert Polman* conceived the project. *Hiroshi Sugimoto* and *Minoru Fujii* provided the Si particles. *Théo Soler* and *Evelijn Akerboom* fabricated the samples, performed the measurements, and did the analysis. *Théo Soler* and *Evelijn Akerboom* drafted the original draft. *Saskia Fiedler* and *Albert Polman* supervised the project and reviewed and edited the chapter.

Chapter 4

Evelijn Akerboom made the samples, performed the CL measurements, did the analysis, and developed the interference model. *Hiroshi Sugimoto* and *Minoru Fujii* provided the Si particles and *Nicolas Perez* and *Ramón Álvarez Puebla* provided the Au nanostars. *Femius Koenderink* helped on the theory on the time characteristics of the resonances. *F. Javier García de Abajo* and *Albert Polman* supervised the project. *Evelijn Akerboom* and *Albert Polman* wrote the original draft and *F. Javier García de Abajo* provided feedback on the chapter.

Chapter 5

Nick Schilder performed the first measurements of TR from a laterally extended e-beam; further measurements of TR were performed by *Evelijn Akerboom*. *Evelijn Akerboom* designed and fabricated the Au pillars, performed the CL measurements and analysis. *F. Javier García de Abajo* and *Albert Polman* supervised the project. *Evelijn Akerboom* and *Albert Polman* wrote the original draft and *F. Javier García de Abajo* provided feedback on the chapter.

Chapter 6

Evelijn Akerboom and *Max Postma* designed the STEM holder for the SEM and *Ulas Demirtas* wrote the required software for 4D-STEM capabilities. *Fatemeh Kiani* and *Giulia Tagliabue* provided the Au flakes. *Evelijn Akerboom* performed the 4D-STEM

measurements, analysis and performed the analytical calculations for the CBED patterns. *F. Javier García de Abajo, Wiebke Albrecht* and *Albert Polman* supervised the project. *Evelijn Akerboom* and *Albert Polman* wrote the original draft and *F. Javier García de Abajo* and *Joanne Etheridge* provided feedback on the chapter.

The author acknowledges the use of text-based artificial intelligence tools, which were employed to provide sentence-level suggestions related to grammar and vocabulary.

Summary

Since the early days of modern physics, there has been a strong desire to see beyond the limits of human vision. Optical microscopes, invented in the seventeenth century, revolutionized biology and material science, yet their resolving power is fundamentally limited by the wavelength of visible light. This has motivated the development of instruments capable of revealing the structure of matter on smaller scales. The electron microscope provides such a tool; the small de Broglie wavelength of electrons combined with the technological evolution of electron optics has enabled imaging with a spatial resolution more than three orders of magnitude beyond that achievable with visible light.

At the same time, the rapid growth of nanophotonic applications has introduced new opportunities. Manipulating light at the nanoscale enables sensitive sensors, on-chip light sources, enhanced light management for photovoltaics, and much more. In all these cases, it is essentials to understand and control how electromagnetic fields are distributed within nanostructures. Understanding and controlling these electromagnetic fields requires experimental techniques capable of probing light–matter interactions at the nanoscale.

Conventional electron microscopy primarily reveals surface morphology in the scanning electron microscope (SEM), or atomic arrangement in the transmission electron microscope (TEM). Electron tomography extends this capability into three dimensions (3D), enabling atomic-scale reconstruction of nanostructures. The traditional contrast mechanisms in SEM or TEM depend on the scattering or absorption of electrons, which encode morphology rather than the optical response of specimens.

To gain insight in the optical properties of materials at the nanoscale, it is essential to probe how materials interact with light at the nanoscale. In this thesis, we use free electrons as an ultrafast, nanoscale, broadband source of optical excitation, and detect the emitted light, termed cathodoluminescence (CL). CL spectroscopy has proven to be a versatile tool for mapping electric near-field strengths in two dimensions. Here, we extend its application to explore how electron spectroscopy techniques can be used to study electric near fields in 3D.

We begin in Chapter 2 by quantitatively studying the coupling strength between the electron and dipolar modes in plasmonic nanospheres. As the electron traverses the particles, it probes the z-component of the electric near-field along its trajectory. The resulting electron-energy dependent coupling strength corresponds to the Fourier transform of this near field. By performing electron-energy dependent CL measurements on plasmonic nanospheres, we show that the strongest coupling

is achieved when the electron's velocity matches the mode's evolution in time, providing a proof for a phase-matching model of electron-mode coupling.

For aloof trajectories, the data is in excellent agreement with theoretical calculations. For penetrating trajectories, however, inelastic scattering from the heavy Au atoms redirects the electron trajectories, which affects the coupling conditions. We develop a first-order recoil correction model that reconciles theory and measurements. Finally, we theoretically identify the conditions for achieving the strongest coupling between the electron and the plasmonic mode: a coupling efficiency of a few percent can be achieved for Au nanospheres with a diameter of 5 nm, using 1 keV electrons. Higher coupling would be achieved for even more confined electric near fields and slower electrons.

Exploiting the phase-matching condition further, we study the dependence of the CL intensity on electron energy and impact parameter in dielectric Si nanoparticles in Chapter 3. In comparison to Au, the lighter Si atoms produce a lower inelastic scattering probability. Furthermore, dielectric nanospheres support Mie resonances tunable by the varying diameter of the particle.

Using electron-energy-dependent CL measurements, we reconstruct the impact-parameter-dependent electron path length through the particle. We then demonstrate selective mode excitation using the phase-matching condition, achieving tailored angular emission patterns in the far field. We demonstrate how we can use the transverse Kerker condition, when the electric dipole and magnetic dipole resonance spectrally overlap, to optimize the relative coupling strength to selected modes, and thereby the directionality, by controlling the electron velocity.

In Chapter 4, we expand our work towards using CL as a 3D metrology technique. By sequentially exiting multiple scatterers with a single electron, we demonstrate the concept of CL interferometry. We investigate a geometry consisting of a free-standing plasmonic tip above a Au surface. The resulting far-field interference patterns, measured via angle- and wavelength- resolved CL, allow us to extract the dimensions of the measured geometry. Through Fourier analysis, we find the scatterer-surface separation, the electron time-of-flight between scattering events, and the decay time of the resonant modes. Our experiments nicely match an analytical interference model, which we further validate by varying the electron energy and performing polarization-resolved measurements.

Next, we consider the dual particle/wave nature of the electron and how it may affect the generation of CL. Conventional CL models treat the electron as a classical point charge and describe experiments well. At the same time, diffraction experiments exploit the wave nature of the electron, described by a finite lateral and temporal coherence length. In Chapter 5 we demonstrate that, even if we extend the electron beam laterally to interact with multiple scatterers at once, the resulting CL emission is the incoherent sum of individual CL emission events.

First, we study the angular emission distribution of transition radiation emitted from a thin Si_3N_4 membrane. We find identical emission distributions for an elec-

tron beam of 4 nm or 6 µm diameter, showing that the excitation creates an incoherent sum of CL emission events distributed over the transverse beam area. Next, inspired by the geometry studied in Chapter 4, we use a pair of plasmonic nanopillars that are precisely spaced horizontally and vertically to study the angle- and wavelength- resolved CL emission. When the pillars are separated by less than 200 nm, the emission exhibits a coherent behavior, evidenced by the presence of an electron time-of-flight signature. However, if the separation is larger than the extent of the particle's electric near fields, the resulting CL is the incoherent sum of the emission from the pillars. These findings indicate that coherent excitation of transversely spaced emitters by a single electron, according to its wave nature, is not observed under our experimental conditions. Further research is needed to determine whether this arises from the finite lateral coherence of the electron beam or reflects a fundamental aspect of the nature of free-electron excitation.

Finally, we develop scanning transmission electron microscopy (STEM) in the SEM using 30 keV electrons in Chapter 6. First, we quantify key parameters of SEM in our laboratory and find an optimum spatial resolution of 4.4 nm and a semi-convergent angle between 1 and 8 mrad, depending on the chosen aperture and working distance. We use a 2D single-electron detector and measure selected-area electron diffraction patterns from a thin crystalline Au flake and acquire convergent-beam electron diffraction (CBED) patterns of a graphene monolayer. With these measurements, we demonstrate the ability of STEM to probe crystallographic information at a low acceleration voltage.

Next, we perform experiments to reveal the spatial coherence of the electron beam in the SEM, based on a technique used in the TEM by others. We acquire CBED patterns from a twisted bilayer of graphene. Due to the small twist angle, the diffraction disks overlap, and we observe interference from electrons scattering from either layer. For a given diffraction order, the period of the interference is determined by the twist angle as well as the distance between the sample and the focal point. We use a geometric model to analyze interference patterns and find agreement for a twist angle of 0.6° and a defocus height of 6 µm. We extract a degree of spatial coherence at two spatial frequencies: 60 % at 0.031 $Å^{-1}$, and 20 % at 0.053 $Å^{-1}$. The data sample a limited fraction of the electron beam and further expanded measurements at different twist angles are needed to reconstruct the full coherence function of the electron beam.

These studies pave the way towards coherence-dependent electron-light interactions in CL microscopy. Further experiments could also exploit the correlation between electron diffraction and CL. Furthermore, single-electron-single-photon correlation measurements could reveal further details on the quantum aspects of electron-light-matter interactions.

In summary, this thesis advances our understanding on how free electrons couple to resonant optical modes. It demonstrates how CL spectroscopy can be used to recover 3D information in plasmonic and dielectric nanostructures, both for optical near fields in individual structures and for assemblies of spatially separated scatter-

ers. It further studies whether and when the coherence properties of electrons in the SEM impact the CL emission, and provides measurements of the electron spatial coherence in the SEM. Together, these approaches pave the way towards 3D optical metrology, and demonstrate the first explorations towards studying quantum-coherent phenomena using CL in the SEM.

Nederlandse samenvatting

Sinds het ontstaan van de moderne natuurkunde, proberen we kleiner te kijken dan het oog reikt. De uitvinding van de optische microscoop in de zeventiende eeuw heeft hier sterk aan bijgedragen en de biologie en materiaalkunde ingrijpend veranderd. Maar het plaatsoplossend vermogen blijft onlosmakelijk verbonden met de golflengte van zichtbaar licht. Zelfs de meest geavanceerde optische technieken kunnen deze limiet niet doorbreken. Dit heeft geleid tot de ontwikkeling van de elektronenmicroscoop. Dankzij de korte de Broglie-golflengte van elektronen en de snelle vooruitgang in de elektronenoptica is een plaatsresolutie bereikt die vele ordes beter is dan het optisch bereik.

Parallel hieraan is er een snelle ontwikkeling geweest in nanofotonische toepassingen. Het manipuleren van licht op kleine schaal maakt het mogelijk om gevoelige sensoren te ontwikkelen en zonnecellen te verbeteren, om er maar twee te noemen. Voor al deze toepassingen is het controleren en begrijpen hoe elektromagnetische velden zich binnen nanostructuren verdelen essentieel. Dit vereist technieken die in staat zijn om de interactie tussen licht en materiaal rechtstreeks op de nanoschaal te onderzoeken.

De elektronenmicroscoop blinkt uit in het zichtbaar maken van oppervlakte morfologie in de scanning elektron microscoop en van de atomaire ordening in de transmissie elektrom microscoop. Maar de signalen in de elektronenmicroscoop zijn gevoelig voor de verstrooing en absorptie van elektronen, maar geven daarmee alleen informatie over de morfologie van het materiaal, en niet over de optische eigenschappen van de structuur.

Voor een diepgaand begrip van nanofotonische en plasmonische systemen is het essentieel om te onderzoeken hoe materialen op nanoschaal met licht interacteren. In dit proefschrift gebruiken we het elektron niet alleen als beeldvormend deeltje, maar als een snelle, kleine en breedbandige bron van optische excitaties. Het uitgezonden licht, kathodoluminiscentie (CL), bevat informatie over de optische eigenschappen van materialen. Terwijl CL traditioneel vooral wordt ingezet voor tweedimensionale metingen, laten we zien dat CL spectroscopie ons in staat stelt om driedimensionale (3D) informatie terug te winnen over de elektrische velden binnen een structuur en over de afstanden tussen een verzameling van structuren.

In Hoofdstuk 2 bestuderen we kwantitatief de koppeling tussen het elektron en de dipool resonantie in plasmonische nanodeeltjes. Wanneer het elektron door het deeltje beweegt, tast het de z-component van het elektrische veld af langs het traject. De elektronenergie-afhankelijke koppelingssterkte komt overeen met de Fou-

riertransformatie van de elektrische veldverdeling. Door CL-metingen uit te voeren als functie van de elektronenergie tonen we aan dat de sterkste koppeling optreedt wanneer de elektronsnelheid gelijk is aan de effectieve fasesnelheid van het oscillerende dipoolveld.

Voor een passerend elektron, komt de data goed overeen met theoretische simulaties. Maar als het elektron door het materiaal heen beweegt, wordt de non-recoil-benadering geschonden door sterke verstrooing aan de zware goudatomen. Daarom ontwikkelen we een eerste-orde recoil-correctiemodel dat theorie en experiment met elkaar in overeenstemming brengt. Ten slotte identificeren we theoretisch de voorwaarden voor het bereiken van de sterkste koppeling tussen het elektron en de plasmonische resonantie. We stellen vast dat daarvoor een ruimtelijk klein elektrisch veld en langzame elektronen vereist zijn. We vinden een maximale koppeling van een paar procent voor een gouddeeltje met een diameter van 5 nm en een electronenergie van 1 keV. De koppeling kan worden verbeterd door nog kleinere deeltjes en nog langzamere elektronen te gebruiken, maar dit is experimenteel een uitdaging.

Om dieper in te gaan op de koppeling van het elektron aan specifieke resonanties in nanofotonische deeltjes, bestuderen we de afhankelijkheid van CL-emissie van de elektronenergie en de positie van impact. In Hoofdstuk 3 gebruiken we hiervoor Si nanodeeltjes om deze afhankelijkheid te onderzoeken. Si biedt twee belangrijke voordelen: de lichtere atomen verlagen de kans op inelastische verstrooiing en diëlektrische structuren ondersteunen Mie-resonanties die regelbaar zijn via de deeltjesdiameter.

Met energie-afhankelijke CL-metingen reconstrueren we de padlengte van het elektron door het deeltje bij verschillende posities van impact. Vervolgens laten we zien dat selectieve excitatie van resonanties mogelijk is door de snelheid van het elektron te matchen aan de oscillerende spatiële veldverdeling. Dit heeft tot resultaat dat we de hoekverdeling van de CL-emissie kunnen controleren. Wanneer de elektrische en magnetische dipoolresonantie spectraal overlappen, bereiken we de transversale Kerker-conditie, waarbij de emissierichting te controleren is door de elektronsnelheid te variëren.

In Hoofdstuk 4 breiden we ons onderzoek uit naar CL als een 3D-metrologietechniek. Door meerdere verstrooiers opeenvolgend te exciteren met één enkel elektron, voeren we CL-interferometrie uit. We onderzoeken een systeem bestaande uit vrijstaande plasmonische tips boven een goudoppervlak. De resulterende hoek- en spectrumafhankelijke CL-emissie laat een interferentiepatroon zien waarvan de periode te relateren is aan de geometrie. We nemen de Fourier transformatie naar het tijdsdomein, wat ons in staat stelt de afstand tussen de verstrooiers, de reistijd van het elektron van de ene verstrooier naar de volgende, en de levensduur van de resonanties te bepalen. De experimenten komen goed overeen met een analytisch model, dat we verder valideren door de elektronenergie te variëren en polarisatie-afhankelijke metingen uit te voeren.

Vervolgens beschouwen de de golf-deeltje-dualiteit van het elektron en het mogelijke effect op de CL-emissie. Hoewel conventionele CL-modellen het elektron als puntlading behandelen, tonen diffractie-experimenten aan dat het elektron ook een golfkarakter heeft met een eindige laterale en temporele coherentielengte. In Hoofdstuk 5 tonen we aan dat zelfs wanneer de elektronenbundel lateraal wordt verbreed zodat deze meerdere verstrooiers tegelijk aanslaat, de resulterende CL-emissie de incoherente som is van de individuele verstrooiers.

Dit demonstreren we eerst aan de hand van de hoekafhankelijke emissie van transitiestraling uit een dun Si_3N_4-membraan, waarbij dezelfde emissie wordt verkregen voor elektronenbundel met een diameter van 4 nm en 6 µm. Vervolgens bestuderen we, geïnspireerd op Hoofdstuk 4, de CL-emissie van een paar van plasmonische nanopilaren met nauwkeurig gecontroleerde horizontale en verticale afstanden. Wanneer de onderlinge horizontale afstand kleiner is dan 200 nm, vertoont de CL-emissie coherente kenmerken, die blijkt uit de bepaling van een welbepaalde elektron-reistijd. Voor grotere afstanden, buiten het bereik van de elektrische nabijvelden, verdwijnt deze coherentie en wordt de emissie volledig incoherent. Deze resultaten suggereren dat coherente excitatie van transversaal gescheiden emitterende deeltjes niet optreedt onder onze experimentele condities. Verdere studie is nodig om te bepalen of dit veroorzaakt wordt door de eindige laterale coherentie van de elektronenbundel of wijst op een fundamentele beperking in elektron-lichtmateriaal interactie

In Hoofdstuk 6 ontwikkelen we scanning transmissie elektronenmicroscopie (STEM) in de SEM, gebruikmakend van laag-energetische elektronen. Eerst karakteriseren we belangrijke parameters van ons meetsysteem en vinden we een ruimtelijke resolutie van 4.4 nm en een semi-convergentiehoek tussen 1 en 8 mrad, afhankelijk van de gekozen diafragma en werkafstand. We demonstreren elektrondiffractie van een dunne kristallijne goudstructuur en elektrondiffractie van een convergente bundel (convergent-beam electron diffraction, CBED) van een monolaag van grafeen. Hiermee tonen we aan dat we met STEM in de SEM in staat zijn om kristallografische informatie te verkrijgen met lage elektronenergieën.

Vervolgens onderzoeken we of de ruimtelijke coherentie van de elektronenbundel in de SEM bepaald kan worden. We registreren een CBED-patroon van een dubbellaag van grafeen met een kleine onderlinge kristal rotatie. Door deze kleine hoek overlappen de diffractiepatronen. Waar de patronen overlappen verschijnt een interferentiepatroon afkomstig van elektronen die aan beide lagen verstrooien. De periode van deze interferentie wordt bepaald door de onderlinge rotatie, de afstand van het sample naar het focuspunt van de elektronbundel en de diffractie-orde. Met een model vinden we goede overeenstemming voor een onderlinge rotatie van 0.6° en een defocus van 6 µm.

We meten op deze manier twee punten van de ruimtelijke coherentiefunctie: 60 % bij 0.031 $Å^{-1}$ en 20 % bij 0.053 $Å^{-1}$. Dit vormt de eerste experimentele bepaling van de ruimtelijke coherentiefunctie in de SEM, zij het dat slechts dat een klein deel van de elektronenbundelkarakteristiek gemeten wordt. Verdere experimenten met

verschillende onderlinge rotaties zijn nodig om de volledige coherentiefunctie over de bundelbreedte te reconstrueren.

Deze resultaten tonen we aan dat STEM in de SEM kan worden ingezet om elektrondiffractie te meten en coherentie van de elektronenbundel bij lage energieën te onderzoeken. Deze ontwikkelingen vormen de basis voor toekomstige studies naar coherentie-afhankelijke elektron-licht interacties, en kunnen uiteindelijk leiden tot correlatiemetingen tussen diffractie en CL, of tot enkel-elektron-enkel-foton correlatie-experimenten die nieuwe inzichten bieden in de kwantumeigenschappen van elektron-licht-materiaal interacties.

Samenvattend verdiept dit proefschrift ons begrip van hoe vrije elektronen koppelen aan materialen met optische resonanties. Het laat zien hoe CL-spectroscopie kan worden ingezet om 3D informatie te verkrijgen, zowel van optische nabijevelden in individuele structuren als van collecties van ruimtelijk gescheiden verstrooiers. Daarnaast wordt onderzocht onder welke condities de ruimtelijke coherentie van elektronen in de SEM de CL-emissie beïnvloedt en worden in de SEM de eerste metingen van deze ruimtelijke coherentie gepresenteerd. Gezamenlijk wijzen deze benaderingen de weg naar 3D optische metrologie en vormen zij de eerste stappen richting het bestuderen van kwantumcoherentie met behulp van CL in de SEM.

Acknowledgments

Doing a PhD often feels like being on a rollercoaster, with its ups and downs, challenges and triumphs. Alongside the demands of research, you are learning to lead your own projects and to grow into an independent scientist. At the same time, it is a unique opportunity to meet inspiring people, both within your institute and at conferences around the world. Completing a PhD is therefore never a solitary achievement. I am deeply grateful to all those who contributed to this journey and made it such a memorable experience.

First of all, I would like to thank **Albert**. Already when I started as a master's student in the group, you were an amazing supervisor. The time you took to help kickstart projects and to help me find my way around AMOLF was truly inspiring. I am very grateful that I started my PhD in your group on electron microscopy, despite never having worked with electron microscopy before. I would not have dared to take on this challenge without your support and optimism. Over the years, I greatly enjoyed our scientific discussions, always going back to the basics to understand the fundamentals of each project. On a non-scientific level, I also appreciated our conversations about newly discovered concerts and inspiring musicians, which sometimes made our meetings last far longer than strictly necessary.
Next, **Javier**, I would like to thank you for being my co-promoter. From the very beginning, we had many fruitful discussions on how to connect theory and experiment, which ultimately led to our successful joint project with **Valerio**. Over the years, I learned a great deal from you and always enjoyed the challenge of translating theoretical ideas into experimental reality. Especially during our most recent project, where we ventured into unknown territory, I truly cherished the inspiring discussions and thought experiments we had at conferences.
I would also like to thank the members of my committee for taking the time to carefully read my thesis: **Wiebke**, **Esther**, **Jorik**, **Claus**, and **Paul**. In particular, I would like to thank **Wiebke**. I had the opportunity to work with you as my supervisor for a month, during which I learned so much about electron diffraction. This was an incredible opportunity that I greatly value.

Of course, my time at AMOLF would not have been the same without all the amazing colleagues I have had over the past few years. First of all, my paranymphs, **Nika** and **Saskia**. **Nika**, you have been such an example to me. Your positive energy is infectious, and your scientific curiosity is truly inspiring. Over the years, we experienced many different compositions of the photonic materials group, but each time it felt like a family, and you contributed greatly to that sense of cohesion. I am very grateful that we were able to finish this adventure together, and I enor-

mously enjoyed our shared conference trips, frozen margaritas and game nights. **Saskia**, since you joined three years ago, you have been a mentor to me. We started projects together, shared frustrations when experiments did not work, and more recently became gym buddies. I truly enjoyed working with you and had a great time during our extensive game nights, always accompanied by excellent rum.
Hollie, you complete the CL ladies. Working on the same microscope and helping each other in the lab has been a joy. I also really appreciated our non-scientific discussions on how to juggle the many tasks and flexible planning that inevitably come with doing a PhD. Your attention to detail and your commitment to creating an inclusive environment are truly admirable, and I sincerely hope we still get to finish the Lord of the Rings marathon we started a year ago. **Robin**, wat leuk dat je ook een PhD bent gaan doen bij AMOLF. Gelukkig zijn we daarnaast ook gewoon vrienden gebleven en ik koester de leuke dingen die we samen zijn blijven doen. Zeilen bij Terschelling, muziek maken of een potje klaverjassen — het is altijd ontzettend gezellig. **Tom**, ik had me geen betere begeleider kunnen wensen toen ik bij AMOLF begon als masterstudent. Ik voelde me meteen thuis en heb enorm genoten van ons gezamenlijke project, dat we zelfs nog tijdens mijn PhD hebben mogen afronden. Of het nu ging om het plannen van de laatste maanden of het repareren van een telefoon, jij was altijd bereid om te helpen. Daarnaast zijn we de afgelopen jaren goede vrienden geworden door wekelijkse squashen, vaak gevolgd door een borreltje waarbij ik erg heb genoten van onze lange discussies. **Alvaro**, thank you for the nice bike rides and dances we shared. **Tomas**, thank you for your expertise and boldness in changing electron optics. **Magda**, thank you for training me on the CL microscope and for your contagious energy. **Stan**, dankjewel voor onze heerlijk ingewikkelde gesprekken over de betekenis van elektronenlading, en vooral voor je vermogen om écht te luisteren. **Marco**, bedankt dat je je soms laat overtuigen om mee te gaan tijdens de koffiepauzes, ik heb altijd ontzettend genoten van leuke boekentips of muzieknerden. **Larissa,** dankjewel voor de luchtige, fijne gesprekken op kantoor. **Sam**, bedankt voor de avontuurlijke en inspirerende gesprekken tijdens koffie en lunch. **Cathalijne**, het is ontzettend leuk om te zien hoe je de optische setup je eigen maakt. I would also like to thank former group members: **Matthias**, **Theo**, **Nick**, **Max B.**, **Andrea**, **Stefan**, **Ana**, **Daphne D.**, **Hannah**, and **Heleen**.
Aside from my direct colleagues I would like to thank everyone who makes AMOLF such a lovely and supporting environment. **Falco**, het was heerlijk om samen even een rondje te wandelen of te dansen bij de coffee corner om onze gedachten te verzetten. **Igor** en **Imme**, door samen in de PV te werken ontdekten we ook een gezamelijke liefde voor koken uit hetzelfde kookboek. Ik heb altijd enorm genoten van onze sporadische, chaotische kookavonden en lange gesprekken. **Mees**, samen in de PV werken was zowel leerzaam als leuk; samenwerken met jou voelt vanzelfsprekend, en de rust die je uitstraalt is ontzettend fijn. **Max P.**, op borrels heb ik altijd ontzettend met jou en **Bas** gelachen, en ik waardeer het enorm hoe behulpzaam en snel je bent bij het ontwerpen en bouwen van nieuwe labopstellingen — en natuurlijk onze (bijna) wekelijkse squash-uurtjes, waarin je me af en toe zelfs liet winnen. **Ethan** and **Loriane**, thank you for joining the pink office and making it such a fun and pleasant place to work and for the nice conferences that we joi-

ned together, I will never forget dancing next to the pool in Cetraro. I would also like to thank all the other colleagues who brighten the days with scientific and non-scientific discussions, including (but not limited to) **Masha, Linde, Daan, Sarah, Daphne D., Daphne A., Yorick, Fanny, Jerome, Nathan, Francesca, Sergio, Elaina, Oleg, Jerome, Marcel, Susan, Mike, Nelson**, **Govert, Fons, Alex, Nick**, and **Deba**.
Another aspect that makes AMOLF such a wonderful place to work is the extensive support from the technical and support departments. I would especially like to thank **Dion, Max P., Ulas, Igor, Bob, Laura, Angela, Rilda**, and **Isabelle** for their help during my PhD.
While doing science is fun, communicating science is just as important. Therefore, I would like to thank **Petra, Pepijn, Jorijn, Tess, Ulas, Daan, Linde, Mees**, and **Falco** for our trip to Expeditie Next. Explaining optical illusions and holograms to children is always a joy.
Joining the PV during my second year of my PhD was one of the best decisions I made. You created such a supportive and fun group, and organizing events with wonderfully silly themes was a great distraction from the seriousness of PhD life. I would like to thank everyone I worked with in the PV, as well as those who joined later, for all the memorable events: **Jente, Mees, Timo, Yvonne, Moritz, Manuel, Mels, Francesca, Daphne, Imme, Mels, Igor, Sofija, Anne-Sophie, Agustin, Masha, Megan, Daan, Bas, Margo, Elaina, Ulas, Teressa, Bibi, Adrian, Peter, Eric**, and **Shi Wei**. Finally, I had the opportunity to help organize the 75th anniversary of AMOLF. Together with **Daan, Niels**, and **Floortje**, we organized a wonderful party. It was a real pleasure to work with you and to scout locations together and finally, a big thanks for the cantine to always supply the coffee.

Tijdens de vier jaar van mijn PhD had ik ook een geweldig netwerk buiten mijn werk dat mij enorm heeft gesteund. **Lonnie**, **Koekie**, **Plien** en **Lot** — wat ben ik blij dat we zulke goede vrienden zijn gebleven. Ik zou niet weten wat ik zonder jullie zou moeten. Het is zo bijzonder om te zien hoe we samen zijn gegroeid van onwetende studenten tot volwassenen met banen en huizen. Ik haal ontzettend veel energie uit onze gezellige etentjes en koffiemomenten tussendoor. Ik hou zo van jullie.
Ik had het geluk dat ik net voor mijn start bij AMOLF een kamer vond, eerst samen met **Nina** en **Sofie**, en later met **Fanny**. Ik heb enorm genoten van ons huiselijke samenwonen: samen thuiswerken tijdens COVID, elkaar voorzien van koffie en thee en een wandelingetje door het park tijdens de lunch. Later volgde nog een verhuizing, zodat ik samen met **Sofie** en **Tim** eindelijk *The Last of Us* kon kijken — zonder de hele nacht nachtmerries te hebben.

Tijdens mijn PhD heeft muziek altijd een grote rol gespeeld. Het was voor mij de perfecte manier om mijn gedachten te verzetten, en samen muziek maken geeft een ontzettend warm en bijzonder gevoel. **Hidde**, we zijn ongeveer tegelijk aan onze PhD begonnen en mogen die nu ook samen afronden. Jij bent zo'n leuk, warm en energiek persoon, en ik heb enorm genoten van alles wat we samen met jou en

Eline hebben gedaan — zeilen, zingen en dansen. **Emma**, met jou kan ik altijd heerlijk kletsen over van alles en nog wat, en je maakt altijd tijd voor een snel kopje koffie of een biertje tussendoor. **Tonke** en **Wessel**, jullie prachtige fietsverhalen en reistips zijn een grote inspiratie voor mij. Ik ben zo blij dat we nog om de paar maanden samen met **Ivo, Maxim**, en, **Lisa** eten, waar we zelfs een sprookjesmoord oplossen.

Natuurlijk waren de afgelopen jaren niet hetzelfde geweest zonder mijn geweldige familie, **pap**, **mam**, **Bart-Jan** en **Kate**. **Pap** en **mam**, jullie zijn er altijd voor mij en als ik denk dat ik iets niet kan of spannend vind, kan ik altijd bij jullie terecht voor steun en een niet denken maar gaan mentaliteit die soms nodig is om hobbels over te komen. Als ik na een lange werkdag langskom, koken jullie altijd heerlijk voor mij en kan ik me lekker in de watten laten leggen. **Bart-Jan** en **Kate**, thank you for welcoming me many times over the last few years in Vienna, showing me your local favorites and strolling around the Christmas markets together. Our amazing hikes with **Frederieke**, **Victor**, or **Frank**, as well as our skiing trips in the Austrian Alps, have always been a wonderful escape — even despite the inevitable frustrations of international train travel.

About the author

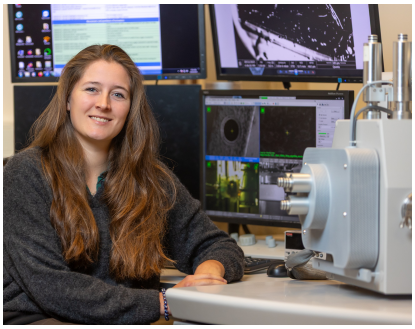

Evelijn Akerboom was born on October 8, 1998 in Amsterdam, the Netherlands. She grew up in Amsterdam and obtained her high-school diploma from Het 4e Gymnasium in 2016. She continued her studies at the University of Amsterdam and Vrije Universiteit Amsterdam, where she graduated with a Bachelor's degree in Physics and Astronomy in 2019.

During her undergraduate studies, she completed an exchange semester in Trondheim, Norway, where she pursued a minor in Biology and Neurology. The courses she attended during this period sparked her interest in biophysics and inspired her to follow the biophysics track of the Physics and Astronomy master's program in Amsterdam. She graduated in 2021, completing a master's thesis on the application of passive radiative cooling for solar panels.

In 2021, Evelijn started her PhD at AMOLF in the group of Prof. dr. A. Polman. Her research focused on the interaction between electrons, light, and matter, with the aim of understanding the underlying fundamental mechanisms. The results of this work are presented in this thesis.

In her free time, Evelijn plays the violin and joined for many years the VU Orchestra in Amsterdam. She also enjoys cycling, cooking, and dancing to jazz music from the 1920s to 1940s.